Lars A. Solli

Development of a lab-on-a-chip platform technology
- experimental and numerical investigations on microfluidic aspects

Thesis for the degree of doktor ingeniør

Trondheim, January 2007

Norwegian University of
Science and Technology
Faculty of Engineering Science and Technology
Department of Energy and Process Engineering

NTNU
Innovation and Creativity

Abstract

The focus on this thesis is the development of a lab-on-a-chip device for real-time detection of enzymatically amplified nucleic acids (using a method called "nucleic acid sequence-based amplification" - NASBA), and the study of microfluidic flows related to this and similar systems. The flows under study are two-phase gas-liquid flow or plug-based flow and hydrodynamically focused flow.

This thesis consists of an introductory part, a theoretical part and five appended papers. In the following, the results from the papers are summed up.

A general multipurpose microchip technology platform for point-of-care diagnostics has been developed. The first prototype studied in this thesis consists of a NASBA chip, manufactured in silicon, along with a custom-made optical detection system. The experimental results proves it is possible to detect real-time NASBA of two different types of artificial single-stranded DNA molecules in chambers with as low volume as 10 nl. This is a reduction of the conventional 20 μl reaction volumes by a factor of 2000.

The second prototype consists of a NASBA chip manufactured in cyclic olefin copolymer and a custom-made instrument. The chip incorporates 12 parallel analysis channels, along with a sample metering system and a non-contact pump mechanism. The chip is able to simultaneously isolate and move twelve sample plugs in steps to four subsequent positions in the parallel channels. The combination of on-chip flexible diaphragms and actuation pins in a surrounding instrument constitute the pumps. The NASBA reaction and the microfluidic system tests were done separately. The results proved it possible to simultaneously detect NASBA in 80 nl parallel detection volumes containing artificial HPV 16 sequences with concentrations as low as 10^{-6} μM, and SiHa cell lines samples of 20 cells per μl. The detection limit is comparable to that of conventional readers, and clinical testing of biological samples in polymer microchips is therefore possible. The microfluidic tests successfully performed metering and controlled movement of nanoliter sized liquid plugs in parallel channels, demonstrating that the pump mechanism has a potential for use in lab-on-a-chip applications. Further, the risk

of cross contamination is drastically reduced between and within subsequently analyzed chips. However, evaporation of liquid reduces the pump quality and the inaccuracy of the positioning indicates the need for improvements of membrane material.

The flowfield inside plugs moving in microchannels are investigated by the means of Micro-Particle Image Velocimetry (micro-PIV) and CFD analysis. The moving plugs exhibit an internal recirculation pattern of liquid flow. The experimental results correspond well with the computational fluid dynamic analysis. The flowfield is characterized inside two different sized plugs moving in a straight microchannel for Reynolds numbers as low as 0.008. Depending on the plug length, different flow profiles predicted by theory are observed. The recirculation flow can be utilized for mixing of reagents within moving plugs. Continuous flow of a liquid through a straight microchannel in the low Reynolds number regime implies parallel streamlines. Thus, in that case, mixing is caused by molecular diffusion. Splitting the liquid into moving plugs with air between, introduces the recirculation streamlines and thus convective mixing. Therefore, a significant reduction of the mixing time can be achieved.

A numerical study of hydrodynamic focusing in microchannels is presented and compared with experimental results. The emphasis is on the characterization of the focused sheet in terms of its shape and position. The sheet defines the measurement plane when using selective seeding, a novel seeding method for micro-PIV. It is found that the sheet is considerably deformed at high flow velocities and large side stream ratios, making the technique applicable to micro-PIV in the velocity ranges below $\sim$10 mm/s. Using lower angles of the side stream inlet channels, the sheet deformation is substantially reduced, extending the velocity range in which selectively seeded micro-PIV is feasible.

The five papers are self-contained publications, listed below.

PAPER I (Chapter 3)

Gulliksen, A., Solli, L. A., Karlsen, F., Rogne, H., Hovig, E., Nordstrøm, T., Sirevåg R., *Real-Time Nucleic Acid Sequence-Based Amplification in Nanoliter Volumes.* Published in: *Analytical Chemistry* **76**(1), pp. 9–14, 2004.

PAPER II (Chapter 4)

Gulliksen A., Solli L. A., Drese K. S., Sörensen O., Karlsen F., Rogne H., Hovig E., and Sirevåg R., *Parallel Nanoliter Detection of Cancer Markers using Polymer*

Microchips. Published in: *Lab Chip*, **5**(4), pp. 416–420, 2005.

PAPER III (Chapter 5)

Solli, L. A., Gulliksen, A., Furuberg, L., Sörensen, O., Karlsen, F., Sætran, L. R., Rogne, H. and Drese, K. S. *A non-contact pump mechanism for parallel movement of nanoliter sized liquid plugs using flexible membranes.* Manuscript for journal publication.

PAPER IV (Chapter 6)

Solli, L. A., Mielnik, M. M., Karlsen F., Sætran, L. R. and Furuberg L., *Flow visualization and simulation of discrete liquid droplets moving in microchannels.* Published in: *Proc. Third National Conference on Computational Mechanics - MekIT'05*, editors: Skallerud, B. and Andersson, H. I., pp. 281–296, Trondheim, Norway, 11-12 May, 2005.

PAPER V (Chapter 7)

Solli, L. A., Sætran, L. R., Mielnik, M. M., *Numerical modelling and experiments on hydrodynamically focused sheets.* Published in: *Proc. Second International Conference on Transport Phenomena in Micro and Nanodevices*, editor: Gad-el-Hak, M., Barga, Italy, 11-15 June, 2006.

Preface

This thesis is submitted in partial fulfillment of requirements for the degree "Doktor Ingeniør" (Doctor of Engineering; Dr.Ing.) at the Norwegian University of Science and Technology (NTNU).

The work was carried out at both the Dept. of Energy and Process Engineering at the Faculty of Engineering Science and Technology, with Professor Lars R. Sætran as supervisor and at the Dept. of Microsystems and Nanotechnology at SINTEF in Oslo, with Dr. Liv Furuberg as my co-supervisor.

NorChip AS is the originator of the lab-on-a-chip project which is the fundament of this work. R&D director Dr. Frank Karlsen has been my co-supervisor in this thesis and superior at my part-time work at NorChip AS.

The research was mainly funded by the Research Council of Norway (NFR), and partially by NorChip AS.

Acknowledgements

First of all, I would like to express my gratitude to my supervisors: Professor Lars R. Sætran, Dr. Liv Furuberg and Dr. Frank Karlsen. All of you have been important contributors to the fulfillment of this project and I am forever grateful for your advice, engagement and support.

I would also like to thank the people at the Department of Energy and Process Engineering and all my fellow students for making my stays in Trondheim enjoyable.

Thanks to NorChip AS for providing research facilities and thanks to everybody at NorChip AS, for their valuable contribution, technical support and good spirits. Not to mention for introducing me to the exciting field of μTAS in the first place.

I would also like to thank SINTEF for providing research facilities and educational collaboration. Particularly all the people at SINTEF MiNaLab, where I have spent most of the time during this project. A special thanks goes to Dr. Henrik Rogne and Dr. Ib-Rune Johansen for their good ideas, professional guidance, positive feedback and comprising and cheerful spirits. Dr. Henrik Rogne has been deeply missed since he lost his struggle against cancer on the 1st of April 2006.

Also, thanks to Associate Professor Ola Sveen at the University of Oslo for help on the biology part of the theory chapter.

I am grateful to all my co-authors for the good collaboration and stimulating discussions, opening my mind to different points of view.

A big thanks goes to my dear friends and colleagues Anja Gulliksen and Dr. Michal Mielnik for fruitful discussions and valuable support during the project.

A special thanks to all the people I have learned to know through conferences and meetings. Your interesting research has inspired and motivated me a whole lot, in addition to making these events memorable social happenings.

Last, but not least, thanks to my nearest friends and family for their patience and support (sometimes by helping me forget it, other times by reminding me of it). This project had its ups and downs, and my spirits followed. I apologize to those who had to bear the brunt of that.

And to Janicke; for putting up with it *all*.

Now, it seems very appropriate to finish off with a quote from the Comic Book Guy of the tv-series "the Simpsons":

"No emoticon can describe how I feel right now."

Oslo, January 2007
Lars A. Solli

Contents

List of Figures

List of Tables

Chapter 1

Introduction

Lars A. Solli

Dept. of Energy and Process Engineering, NTNU.

Lab-on-a-chip (LOC) is a term for devices that integrate one or multiple laboratory functions onto a single chip with outer dimensions of millimeters to a few centimeters. Briefly, the chip is able to manipulate extremely small volumes of sample and provide rapid test results. The chip is controlled by an external instrument. The following sections provide a *vision* on how the concept *may* work.

Current situation:
Anne visits her local doctor. Its time for her cervix cancer check, which she takes every three years. The doctor takes a sample with epithelial cells and tells her that if she does not hear anything within three weeks, it is OK. The doctor sends the Pap-smear to a central laboratory where it is studied manually under a microscope. Some suspicious cell changes are seen. The results are mailed back to the doctor. He calls Anne and tells her that she will need to retest in 6 months[1] to see if there still are any cell changes. Anne spends 6 months anxiously waiting, but the second test shows no cell changes. The first test was probably a false positive result, meaning she had cell changes that were not confirmed by histology[2], regarded as the "gold standard" in the morphological grading of cell abnormalities (Nijhuis *et al.*, 2006).

First LOC systems start to appear:
Anne visits her doctor again. Cervix samples may, if necessary, be analyzed more often than before as costs are now much lower. The doctor mixes Anne's epithelial cells from the swab with a preservation solution and selects a polymer chip for cervix screening from his fridge. A droplet of the solution is applied to the polymer

---

[1]Quality assurance manual, Cervical cancer screening programme in The Cancer Registry of Norway (www.kreftregisteret.no).

[2]Histology is the study of tissue sectioned as a thin slice.

chip and the chip is inserted into the LOC instrument on his desk. The automatic test takes two hours, so Anne goes shopping and visits the doctor's office on her way home. The doctor tells her that her test produced 9 green lights on the LOC panel and tells her that the test is negative; no mRNA activity was found for the 5 markers of high cancer risk human papillomavirus (HPV) types and the 4 human biomarkers of cervical carcinogenesis[3]. If some of the markers had been positive, she would have needed to see a specialist for a thorough follow-up and suitable treatment.

Impact of LOC on a wider scale:
Anne now considers it convenient that tests for common conditions are carried out by her own doctor. A small, hand-held instrument lies at the doctor's desk. With this instrument he is able to test her for a wide range of pathological conditions, such as cancers. Anne even thinks of buying her own hand-held instrument for home checks. At home she can test for less serious diagnoses such as respiratory diseases and check the food in her kitchen for bacteria.

Aim of thesis:

This thesis deals with issues related to the development of an LOC device for real-time detection of enzymatically amplified nucleic acids (using a method called "nucleic acid sequence-based amplification" - NASBA), including experimental and numerical investigations of LOC related flows.

1.1   Background and motivation

Now, what is really a lab-on-a-chip system? Is it related to the MEMS industry? What is mRNA, and what is its connection with a virus? A lot of different questions might rise from the introduction to this thesis. The fist sections will give a brief description of the LOC concept, its history and definitions of terms related to the industry. Secondly, the effects of downscaling a laboratory onto a chip is discussed. Further, advantages and disadvantages of the technology are addressed, along with the presentation of some commercial applications and challenges related to the impact of LOC systems. Finally, the employment of mRNA in LOC is addressed.

This general discussion is largely based on sources such as Ahn *et al.* (2004), van den Berg & Bergvald (2006), Brody *et al.* (1996), Dittrich & Manz

---

[3]This choice of markers is provided as an example. For more information about cancer risk HPV types, see e.g. Jenkins (2001) or Koliopoulos *et al.* (2007).

(2006), Gad-el-Hak (1999), Mielnik (2005), Saliterman (2006), Zhang *et al.* (2006), unless specified elsewhere.

1.1.1 The concept of lab-on-a-chip

Historical background and future perspective

The birth of microtechnology in the late 1950s, realized integrated semiconductor structures for microelectronic chips by the use of lithography. In the 60s, the technology improved with the ability to make micrometer or sub-micrometer sized mechanical structures on silicon wafers. During these early years, development of applications such as pressure and acceleration sensors, and other devices with mechanically moveable parts were the most common in the area. The interest in fluid handling devices started in 1975, when the first microfabricated gas chromatograph was presented (Terry, 1975). However, it was not until the early 1990s before the introduction of miniaturized formats for analytical chemistry and biology began to evolve. Research groups mainly from Europe developed microfluidic components such as micropumps, micromixers, microheaters, microflowsensors, etc., in silicon/glass/polymer substrate materials using microtechnology. The term "miniaturized total analysis system" as a novel concept for chemical sensing (later actually abbreviated to μTAS), saw its light of day in 1990 by Manz *et al.* The work in this period demonstrated that integration of pre-treatment steps, usually done in laboratories, could extend the simple sensor functionality towards a complete laboratory analysis, including e.g. additional cleaning and separation steps.

A milestone in the research and commercial interest emerged in the mid 90s, when the technology proved to be a promising tool for genomics[4], with expression profiling applications such as capillary electrophoresis[5] and DNA microarrays[6]. In addition started an interest for a portable bio/chemical warfare agent detection system from the US military, which started to support US research programs in the field. This period also changed the concept of μTAS - earlier limited to integration of processes for analysis, now broadened to include possibilities for detecting and characterizing different individual components and other non-analysis processes. Hence the term "lab-on-a-chip" was introduced. This multidisciplinary field of research brings the chemist, the physicist, the biologist, the electrical engineer, the mechanical engineer and the medical technologist together to work with *microfluidics*, the essential generic technology that comprises the field.

---

[4]Genomics is the study of the entire genome of an organism.

[5]Capillary electrophoresis is a method to separate ionic species (e.g. DNA) in capillary tubes, based on their size to charge ratio.

[6]DNA microarray is a collection of microscopic DNA spots on a substrate.

The last years have seen a growing interest in companies and applied research groups in many different fields of LOC applications, such as clinical analysis, DNA analysis, proteomics[7] analysis, combinatorial synthesis/analysis, immunoassays[8], toxicity monitoring, and even forensic analysis applications. The global market of microfluidic applications in the life science had a value of €500 million in 2005, and could rise to around €1.4 billion by 2008, particulary if sales of different application area devices live up to their promise (Clayton, 2005).

A significant application area for this technology is clinical diagnostics, which is also the application area of the device in this thesis. Specifically for clinical diagnostics, diseases, can be diagnosed by performing various analyzes on proteins, DNA, RNA, etc. and by observation of symptoms. The early, rapid, and sensitive detection of the disease state is a vital goal for clinical diagnoses. The biochemical changes in the patient's blood, salvia, cervix smear or other bodily fluids can signal organ damage or dysfunction prior to observable microscopic cellular damages (from i.e. Pap smear or biopsy) or other symptoms. So there has been a large demand for the development of an easy-to-handle and inexpensive clinical diagnostic LOC systems, which has the sampling/identifying capability of fast and reliable measurements of metabolic parameters from a human body with minimum invasion (Ahn *et al.*, 2004).

Terminology

The lab-on-a-chip technology in the life science research area is approached by scientists from many different disciplines each having their own "language" and standards. The following provides definitions of the most common words that have emerged over the years. Some of the meanings may overlap.

- *Microfluidic system* signifies chips or systems that comprise any kind of flow and functions in microsized channels. Such as e.g. cellsorter, flow mixing device, PCR chip, etc.

- *MEMS* (Micro Electromechanical Systems). The word MEMS is taken from the semiconductor industry, and refers to the fabrication of electronic or mechanical components on chips. Most typically sensors (e.g. pressure and acceleration) and actuators incorporate MEMS technology.

- *BioMEMS* refers to MEMS for biological applications.

- *MOEMS* (Micro Opto-Electrical-Mechanical Systems) refers to MEMS including optical elements.

---

[7]Proteomics is the next step of genomics, the study of protein expression of organisms.

[8]An immunoassay is a biochemical test that measures the level of a substance in a biological liquid by the use of the specific binding of an antibody to its antigen.

- *MST* (Micro Systems Technology) is an European term synonymous with MEMS.

1.1.2 Size effects

Miniaturization of analytical instruments is not a simple matter of reducing their size. The physical behaviour of a system depends on its size. At small scales different effects come important, rendering some processes inefficient and others useless, but some also more efficient. It may be difficult to replicate smaller versions of some devices because of material or process limitations. For these reasons it might be necessary to develop alternative methods for performing laboratory tasks equivalent to macroscale on microscale.

The same substance can have a whole different physical behaviour when subjected to systems of variable size. An classical example is capillary motion. If a capillary tube is introduced vertically to a pool of water, the water will rise into the capillary due to surface forces. The same phenomenon will not happen in a larger tube as for example a straw or a pipeline.

Maybe the most common characteristic of microscale flow is that the Reynolds number[9] is typically low, which means that the fluid dynamics are dominated by viscous drag rather than inertia. The following example is provided to illustrate this.

- **Example - Low Reynolds number flow**
  Now, what does it really mean that the Reynolds number is small? What is the difference in the experience of a flow dominated by viscous forces rather than inertia? This is demonstrated by an interesting example given by Purcell (1977). Consider a man swimming in water. This gives a Reynolds number of 10^4, if we put in reasonable dimensions. The movement in water by a human being is assumed to be a well–known experience, and the distance one can drift from the power one swimming stroke or kick is common practice. Consider a bacteria (e.g. *E. coli*) with a radius of 1 μm, moving around in the same water with a typical speed of 30 μm/s. The Reynolds number is approximately 10^{-5}. It experiences a viscous drag force $F_D = 6\pi\mu RU$, also known as Stokes' solution for creeping flow past a solid sphere (White, 1991), where R is the radius of the bacteria and μ and U is the viscosity and the velocity of the surrounding fluid, respectively. Using Newton's second law, the motion of the bacteria can be described as follows:

---

[9]The reader that is unfamiliar to the Reynolds number may refer to the definition in Theory chapter, Sec. 2.3.3.

$$m_b\frac{\partial u}{\partial t} = m_b\frac{\partial^2 x}{\partial t^2} = -6\pi\mu R u(t), \tag{1.1}$$

where m_b is the mass of the bacteria, $u(t)$ is its velocity and $x(t)$ is the distance covered. By giving the bacteria an initial velocity u_0 and an initial distance $x_0 = 0$, we can find both the expressions for velocity and distance by integrating Eq. 1.1 once and twice, respectively. They are given by:

$$u(t) = u_0 e^{-\frac{9\mu}{2\rho_b R^2}t} \tag{1.2}$$

and

$$x(t) = -\frac{2u_0\rho_b R^2}{9\mu}\left(e^{-\frac{9\mu}{2\rho_b R^2}t} - 1\right), \tag{1.3}$$

where ρ_b is the density of the bacteria (spherical bacteria: $\rho_b = 3m_b/4\pi R^3$). To get a closer look at the effect of these equations, we insert the values of the example of the moving bacteria into Eq. 1.2 and Eq. 1.3. We assume the bacteria has a density of $\rho_b = 10^3$ kg m^{-3} and a initial velocity of $u_0 = 30~\mu$m s^{-1}, and that the viscosity of water is $\mu = 10^{-3}$ N s m^{-2}. Fig. 1.1a below displays a plot of the velocity of the bacteria, $u(t)$, whilst Fig. 1.1b displays a plot of the covered distance, $x(t)$. In Fig. 1.1a it can be noted that after just approximately 0.6 μs the bacteria has experienced a rapid decrease of its velocity. It has almost stopped completely. Further, it can be seen from Fig. 1.1b that the bacteria will not coast further than about 0.007 nm, which is a distance of order 10^{-6} the size of the bacteria. In fact, the bacteria has a hard time moving anywhere. Given the same conditions, it means that our swimming stroke would bring us below the distance of a single strand of hair. Compared to our perception of moving around in water, this example makes it clear what low Reynolds number means. Inertia plays no role whatsoever; movement is entirely dominated by the forces that are exerted *at that very moment*, and by nothing in the past.

1.1.3   Low Reynolds number

Typically, low Reynolds number flows are thus laminar, meaning that, unlike the mixing, twisting, rotating and unsteady nature of turbulent flows usually encountered in the natural environment and in the familiar macro-scale industrial processes, flow on the microscale is naturally smooth, regular and "streamlined". Processes such as mixing of different fluids, reagents, etc., is an important and
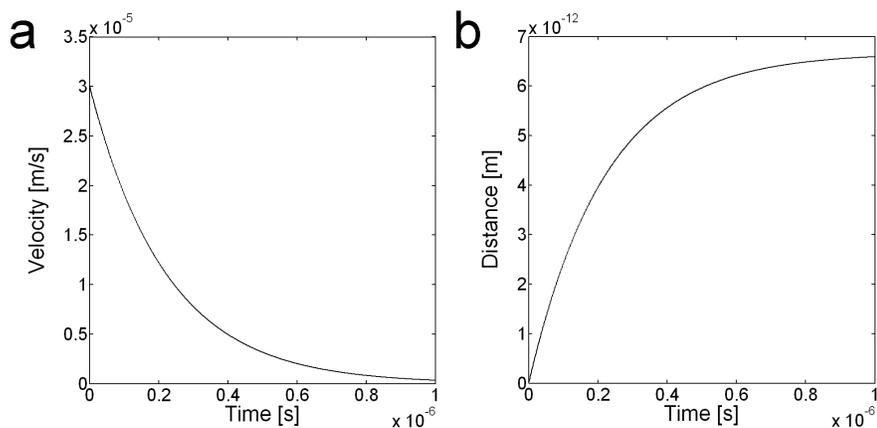
Figure 1.1: a The velocity of a bacteria in water. **b** The distance a bacteria with an initial velocity of 30 μm/s is able to travel in water.

necessary operation in most LOC systems. The dominant mixing mechanism in laminar flows is, however, that of molecular diffusion, which in many cases is too slow and inefficient. Several methods involving mixing of liquid streams has been developed. Many groups have presented mixing techniques either by the use of external fields or by the employment of advanced 3D structures to agitate the flow and create temporary chaotic fluctuations, or by various fluid layering to reduce the diffusion length (see Nguyen & Wu (2005) for a review about micromixers). As a digression, it is interesting to mention that while great efforts are being made to suppress turbulence in certain macro-world applications (e.g. in gas pipe flows to reduce pressure loss and thus cost of gas transport), the opposite is being done in micro-world applications, where lack of turbulence might be a challenge. On the other hand, laminar flow is predictable and may, in principle, be readily determined by means of analytical studies and computational analysis. As will be discussed below, the situation is, however, often not that simple.

There are several instances in which the low Reynolds number in microfluidic devices has been used for novel purposes. Some groups report on the study of chemotaxis[10] by generation of nontrivial chemical gradients (Jeon *et al.*, 2002), the use of ultrafast mixing to study protein folding (Pollack *et al.*, 2001), as well as the study protein growth (Hansen *et al.*, 2002).

---

[10]Chemotaxis is the study of the innate movement of cells, bacteria, etc. directed by certain chemicals in their environment.

Surface-to-volume ratio

The surface-to-volume ratio is the main factor responsible (directly or indirectly) for a majority of the differences in physical behaviour observed between the macro and micro worlds of fluid mechanics. Considering a macro-scale flow, such as the flow in a gas pipe with diameter D of order $\sim$1 m, the surface-to-volume ratio is approximately $D^2/D^3 = 1/D = 1$ m^{-1}. Next, considering a microchannel with diameter of order $\sim 10^{-5}$ m, i.e. 10 μm, the surface-to-volume ratio becomes $\sim 10^5$ m^{-1}. As dimensions shrink, the ratio of surface area to system volume increases, and so does the relative importance of surface forces. This gives rise to various effects characteristic for microscale flows. In addition to the familiar pressure-driven flows and the already mentioned capillary effects, fluid motion can be generated by taking advantages of electrical and magnetic fields. Flow can also be generated more efficiently in microscale by centrifugal force and by acoustic streaming/ultrasonic effects (see Laser & Santiago (2004) for a review about pumping mechanisms in microflows).

When it comes to reaction chambers in LOC, the absorption of reactants on the walls is of relatively higher importance than in corresponding macroscopic test tubes. Thus, surface treatment is of crucial importance of LOC. The numerous physical effects encountered and applied in microfluidics, and their combination, together with the presence of biological species, particle-laden and multiphase flows, chemical reactions, and the use of complex, three dimensional channel geometries, pose a considerable challenge by complicating the theoretical and computational treatment of these flows.

1.1.4 Advantages of LOC

The LOC technology may provide several advantages. The following lists some typical advantages:

- Low fluid volumes consumption, which is beneficial for e.g. lower cost of expensive reagents, environmental pollution (less waste), and less sample fluid is used.

- Faster response time, e.g. heating, mixing.

- Better compactness of the system, due to large integration of functionality and small volumes.

- High-throughput analysis, due to the parallelization ability (see Fig. 1.2).

- Lower fabrication costs of the device, allowing mass production of disposable devices.

- Possibility of full control and monitoring of biological and biochemical processes within the same environment.

- Possibility to simulate and study *in vivo* biological and clinical processes.

- Possibility to perform a complete diagnostics process in real-time without human interference.

- Possibility to completely standardize every step within a diagnostic or a prognostic protocol.
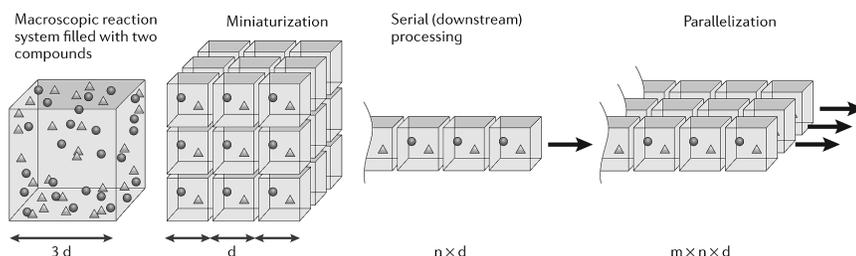
Figure 1.2: Sketch showing the effects of miniaturization and parallelization. *d* is the length of an edge, while *n* and *m* are numbers of reaction systems in serial and parallel, respectively. The image is taken from Dittrich & Manz (2006).

1.1.5   Challenges of LOC

Amongst the challenges of the technology are the following:

- Physical effects such as capillary, evaporation and chemical effects (between chip substrate and sample) become more dominant and make LOC systems behave differently and sometimes more complex than conventional lab equipment.

- Connection between a microchip and its features to a macroscopic system, such as tubing systems and interconnections.

- Reduced sensitivity, due to e.g. few molecules, which leads to low signal to noise ratios.

- Reduced possibility of using large volume of sample.

9

The first two items must be addressed in order to accomplish future LOC systems. The last challenge reflects the reduced possibility of application areas where low concentration of targets are present, such as *E. coli* or salmonella in water (less than 10 copies per gram).

1.1.6 State-of-the-art LOC

There are a vast number of companies worldwide that claim products and technology within the LOC field. Current applications with lab-on-a-chip technology on the market include real-time PCR[11], electrophoresis, microarrays, immunoassys and various devices for biomolecule detection. The applications that are in need of a flow system (i.e. not array-based), usually rely on either electro-osmosis[12], pressure or centrifugal force to drive the the flow.

Nevertheless, there are only a few examples of more or less successful businesses that commercialize LOC systems, as reported in van den Berg & Bergvald (2006). Perhaps the most successful company is Affymetrix with their GeneChip® Arrays for nucleic acid analysis, although one may argue about the microfluidic content of an array product. The I-Stat® analyzer (Abbott) is an example of a product that is doing well in the area of clinical diagnostic applications. This handheld analyzer provides point-of-care testing for monitoring a variety of clinically relevant parameters, as i.e. monitoring or testing of blood gases, electrolytes, coagulation, hematology, glucose, and cardiac markers (www.abbott.com).

Companies with PCR technology include Roche, Caliper Life Science and Cepheid. Fig. 1.3 shows Cepheid's GeneXpert® system, which is a real-time PCR instrument that combines fully integrated sample preparation with the amplification and detection process. It can house four cartridges, where each of them can detect up to four nucleic acids. The system is used at the mail sorting facilities of the United States Postal Service for biothreat protection of agents such as anthrax spores (www.cepheid.com).

Further examples of companies that have a technology platform, but have not yet shown the same level of commercialization as the companies mentioned above, is Swedish Gyros with their CD-systems (based on centrifugal forces) and Fluidigm with their integrated fluidic circuit (IFC) technology. Among the large worldwide companies that try to explore the potential of LOC/microfluidics devices and systems are Motorola, Texas Instruments and Philips. See the report by Clayton

---

[11]PCR (polymerase chain reaction) is a biochemistry technique for enzymatically replicate or amplify DNA for further study.

[12]Electro-osmosis is a method to induce flow in a microchannel by the use of an ionic double layer present at the interface of the immobile, charged surface of the microchannel and the adjacent counter-ions in the fluid. The application of an electric field causes the dissolved ions, together with the bulk fluid, to move to the respective electrode.

Figure 1.3: Images of Cepheid's GeneXpert® technology. The upper images show the instrument package, while the bottom image shows the cartridge. The inset in the middle shows how a cartridge is inserted into the reader. All images are taken from www.cepheid.com.

(2005) for a list of companies and application areas.

1.1.7 Challenges

The actual impact of LOC on the life science and biotechnology so far has been limited (except for microarray technology). Hong & Quake report in 2003 that very few academic biology laboratories use these devices on a routine basis, and when faced with a decision on how to automate, most companies still choose macroscopic robots. The disconnect in this area between technology developers and technology users is particulary dramatic, and has lasted longer than many observers expected. "One reason for this disconnect has been the difficulty of making the transition from simple microfluidic components to highly integrated, functional systems with no operating protocols. Individual microfluidic components such as micropumps, micromixers, microheaters, microvessels, etc., are of little use unless they can be integrated together in a functional system (Hong & Quake, 2003)".

1.1.8   Why detect mRNA?

The system reported in this thesis will be based on sensitive detection of mRNA[13] bio-markers. The method detects genetic activity of bacteria, viruses or irregular cell behaviour that is indicative of disease (Saliterman, 2006).

Current point-of-care diagnostic systems use simplified immunoassay based dot-blots or strip reactions. The immunoassay approach offers high clinical specificity, but generally low sensitivity levels (Saliterman, 2006). It is recommended for only a few clinical applications. Depending on the disease in question, the mRNA approach offers clinical specificity that is at least as good, combined with higher sensitivity due to the possibility of target amplification and sensitive detection (Cook (2003) and Deiman *et al.* (2002)). It is applicable to a wider range of conditions.

An alternative would be to use DNA methods. Like mRNA methods, these are highly analytically selective and sensitive, especially if amplified. Theoretically, only one bio-marker molecule is necessary in the reaction volume to get a positive detection. But DNA tests detect only the presence of bacteria or viruses - they cannot give any information about their activity. False positive results due to dead bacteria and viruses are also likely. In comparison, results based on mRNA methods will provide relevant clinical information about the bacteria or viruses activity which is important for tracking of disease.

mRNA methods are also superior for measuring the effectiveness of therapies. The active markers are measured, not the inactivated ones.

1.2   Objectives

The main objectives of this doctoral project may be summarized as follows:

1. Study and develop microfluidic systems that comprise a lab-on-a-chip technology platform.

2. Design and build micro-structures.

3. Perform experimental and numerical investigations on lab-on-a-chip related flows, such as e.g. plug-based and hydrodynamically focused flow.

The first objective is the main topic of this thesis and its achievements are reported in Chapters 3, 4 and 5. The second and third objective is related to the first, as it turned out to be a spin off task for the ideas that evolved from the work

---

[13]For a more thoroughly explanation of mRNA and other bio molecules, the reader may refer to the biochemistry section of the theory chapter, sec. 2.2.

on the lab-on-a-chip technology. This work is reported in Chapters 6 and 7.

A short summary of the achievements is presented in sec. 1.3 below.

1.3   Summary of thesis

This thesis is composed of six chapters in addition to this introductory chapter. Five of these (chapters 3, 4, 5, 6 and 7) are self-contained articles with introduction, experimental details, results and discussion, and list of references, and may hence be read separately. Chapter 2 presents the relevant theory of the thesis.

The main focus of this work is on the development of the NASBA microchip (chapters 3, 4 and 5), which consists of the amplification and detection part of a lab-on-a-chip system. Chapter 6 presents a numerical and experimental study of liquid plugs moving in microchannels, whilst Chapter 7 involves a numerical study on hydrodynamic focusing. A brief description and summary of the individual chapters is presented below.

Chapter 2 - Theory

This chapter presents the theory relevant to the development of this specific lab-on-a-chip device. The chapter begins with an introduction to microfabrication, where the fabrication methods used in this work and other relevant methods are discussed. Secondly, the biological aspects of this work are addressed. The reader is provided with an explanation of the most common cellular molecules, along with an examination of the NASBA reaction and its detection method. Third, the basic theory of the fluid mechanics relevant to microscale flows are addressed, and attention is also given to aspects such as surface forces, diffusion and evaporation. Finally, a powerful tool when designing and testing microsystem devices is computational simulations. The last section introduces the commercial CFD-software ANSYS-CFX and its specific features used in this work.

Chapter 3 - PAPER I

A. Gulliksen, L. A. Solli, F. Karlsen, H. Rogne, E. Hovig, T. Nordstrøm and R. Sirevåg,
Real-time nucleic acid sequence-based amplification in nanoliter volumes

This paper presents the first prototype of the NASBA chip, which was manufactured in silicon, along with a custom-made optical detection system.

It deals with detection of two different types of artificial single-stranded DNA molecules in several nanoliter sized volumes. The experimental results proves it is possible to detect real-time NASBA in chambers with as low volume as 10 nl. This is a reduction of the conventional 20 μl reaction volumes by a factor of 2000. To the authors knowledge, this is the first time NASBA has been demonstrated in such a microsystem format (Gulliksen *et al.*, 2004).

The second author participated in the experiments and the writing of the paper.

Chapter 4 - PAPER II

A. Gulliksen, L. A. Solli, K. S. Drese, O. Sörensen, F. Karlsen, H. Rogne, E. Hovig and R. Sirevåg,
Parallel nanoliter detection of cancer markers using polymer microchips

This paper presents the first part of the work on the second prototype of the NASBA chip platform. This chip is made of COC polymer and has twelve parallel channels for detection of different cancer markers. It deals with detection limits of artificial HPV 16 sequences and SiHa cell line samples (biological material) using real-time NASBA in 80 nl detection volumes. The results proved it possible to simultaneously detect NASBA in samples containing artificial HPV 16 sequences with concentrations as low as 10^{-6} μM, and SiHa cell lines samples of 20 cells per μl. These results are comparable to the detection limit of conventional readers, thus the work concludes that clinical testing of biological samples in polymer microchips using NASBA is possible (Gulliksen *et al.*, 2005).

The second author participated in the experiments and the writing of the paper. The chip was designed by the third and fourth author, but the second author participated in the design discussions.

Chapter 5 - PAPER III

L. A. Solli, A. Gulliksen, L. Furuberg, O. Sörensen, F. Karlsen, L. R. Sætran, H. Rogne and K. S. Drese
A non-contact pump mechanism for parallel movement of nanoliter sized liquid plugs using flexible diaphragms

This manuscript presents the last part of the work on the second prototype of the NASBA chip. An advantageous option in a LOC system, is the ability to divide the sample into independently controllable discrete nanoliter sized liquid

plugs. For example, a microfluidic operation can be reduced to a set of repeated basic operations, i.e., moving one plug over one unit of action point.

This work presents a novel non-contact pumping mechanism based on on-chip flexible membranes combined with actuation pins in the surrounding instrument. The results proved it possible to simultaneously meter, isolate and transport liquid plugs. However, evaporation of liquid reduces the pump quality and the noise in the results indicates the need for improvements of membrane material. The benefits of this system are the reduction of cross contamination risks between the twelve on-chip analysis channels, and also between the instrument parts and sequentially analysed chips. In addition, the pump mechanism employs low-cost manufacturing, which facilitates disposable chips (Solli *et al.*, 2007).

The first author performed the experiments and wrote the paper.

Chapter 6 - PAPER IV

L. A. Solli, M. M. Mielnik, F. Karlsen, L. R. Sætran and L. Furuberg,
Flow visualization and simulation of discrete liquid droplets moving in microchannels

The work with the NASBA chip in Paper II and III revealed the need of investigations concerning the movement of liquid plugs[14] in microchannels and subsequent mixing with in-channels dried reagents. Mixing in microchannels is dominated by molecular diffusion. This paper reports on the recirculation pattern within moving plugs, and the change of the flow profiles when the height-to-length ratio β of the plugs are decreasing. The work compares experimental results of microscale particle image velocimetry (micro-PIV) with computational fluid dynamic analysis and a theoretical description by Duda & Vrentas (1971). It is concluded that the internal recirculation streamlines generated by the plug movement, molecular diffusion can be combined with convective mixing. This results in a significant decrease of the mixing time for reagents with large molecules (< 100 nm) (Solli *et al.*, 2005).

The first author performed all experiments, simulations and analytical calculations, and wrote the paper.

Chapter 7 - PAPER V

L. A. Solli, L. R. Sætran and M. M. Mielnik,
Numerical and experimental investigation of hydrodynamically fo-

---

[14]although they are in this title called droplets. The literature is not consistent with the terms, and at this stage in this project, droplets was the preferred nomenclature.

cused sheets

A novel seeding method for micro-PIV was developed at NTNU (Mielnik & Sætran, 2006). The method relies on selective seeding of a hydrodynamically focused fluid layer within an otherwise particle-free flow. Obtaining good measurement data greatly relies on the characteristics of the focused layer, as it defines the measurement plane of the system. This paper presents a numerical study of hydrodynamic focusing in microchannels, compared with experimental results. The device is a four-channel intersection, where the sheet position can be controlled by altering the ratio of the side flow streams. The characteristics of the focused sheet, in terms of its shape and position, were investigated with emphasis on the selective seeding technique. It is concluded that hydrodynamic focusing may successfully be applied in micro-PIV for velocities below ∼10 mm/s, along with that lowering of the angle of the buffer stream inlets substantially improves this velocity range (Solli *et al.*, 2006).

The first author did the numerical work and wrote the paper.

1.4 Other minor publications during Dr.Ing. studies

Peer reviewed conference proceedings

1. *A micro fabricated system for real-time amplification and detection of up to 50 different cancer markers in 1.5 microliter of purified RNA,*
   Gulliksen, A., Solli, L. A., Morland, E., Skomedal, H., Morland, G., Hagen, M., Rogne, H., Fismen, B. G., Drese, K. S., Sörensen, O. and Karlsen, F., Int. J. Cancer, 2002, suppl.13, 205 - 205.

2. *Detection of real-time NASBA in a 10 nl silicon-glass microchip,*
   Solli, L. A., Gulliksen, A., Nordstrøm, T., Sirevåg R. and Rogne, H., Eurosensors XVI, The 16th European Conference on Solid-State Transducers, September 15-18, 2002, Prague, Czech Republic. [**oral presentation**]

3. *Detection of multiple real-time NASBA in nanoliter volume,*
   Gulliksen, A., Solli, L. A., Karlsen, F., Sirevåg, R. and Rogne, H., Proc. of the μTAS Symposium (μTAS 2002), Nara, Japan, Nov 2002, 184-186.

4. *Design and realization of a Lab-on-a-Chip system for multiple real-time detection of Nucleic Acid Sequence-Based Amplification (NASBA),*
   Drese, K. S., Solli, L. A., Sörensen, O. and Gulliksen, A.,

smallTalk2003, The Microfluidics, Microarrays and BioMEMS conference, July 13-16, 2003, San Jose, CA, USA.

5. *Flowsensor for dosing applications and microfluidics at SINTEF,*
   Furuberg, L., Wang, D., Vogl, A. and Solli, L. A.,
   Micro Structure Workshop 2004 (MSW 2004), Ystad, Sweden, March 2004.

Invited presentations

1. *"Detection of Parallel Real-Time NASBA Reactions on a Microchip",*
   Solli, L. A.,
   MEMS seminar, NTNU, Trondheim, Dec. 4, 2002.

Patents

1. *"A Device for Carrying out a Biological Assay",*
   Frank Karlsen, Anja Gulliksen and Lars Anders Solli,
   PCT patent application PCT/GB2005/004524 (2004)

References

AHN, C., CHOI, J.-W., BEAUCAGE, G., NEVIN, J. H., LEE, J.-B., PUNTAMBEKAR, A. & LEE, J. Y. 2004 Disposable smart lab on a chip for point-of-care clinical diagnostics. *Proceedings of the IEEE* **92** (1), 154–173.

VAN DEN BERG, A. & BERGVALD, P. 2006 Labs-on-a-chip: origin, highlights and future perspectives. On the occation of the 10th μTAS conference. *Lab on a Chip* **6** (10), 1266–1273.

BRODY, J. P., YAGER, P., GOLDSTEIN, R. E. & AUSTIN, R. H. 1996 Biotechnology at low Reynolds numbers. *Biophysical Journal* **71** (6), 3430–3441.

CLAYTON, J. 2005 Go with the microflow. *Nature Methods* **2** (8), 621–627.

COOK, N. 2003 The use of nasba for the detection of microbial pathogens in food and environmental samples. *Journal of Microbiological Methods* **53** (2), 165–174.

DEIMAN, B., VAN AARLE, P. & SILLEKENS, P. 2002 Characteristics and applications of nucleic acid sequence-based amplification (NASBA). *Molecular Biotechnology* **20** (2), 163–179.

DITTRICH, P. & MANZ, A. 2006 Lab-on-a-chip: microfluidics in drug discovery. *Nature Reviews Drug Discovery* **5** (3), 210–218.

DUDA, J. L. & VRENTAS, J. S. 1971 Steady flow in the region of closed streamlines in a cylindrical cavity. *Journal of Fluid Mechanics* **45**, 247–260.

GAD-EL-HAK, M. 1999 The fluid mechanics of microdevices - the freeman scholar lecture. *J. Fluids Eng.* **121**, 5–33.

GULLIKSEN, A., SOLLI, L., KARLSEN, F., ROGNE, H., HOVIG, E., NORDSTROM, T. & SIREVAG, R. 2004 Real-time nucleic acid sequence-based amplification in nanoliter volumes. *Analytical Chemistry* **76** (1), 9–14.

GULLIKSEN, A., SOLLI, L. A., DRESE, K. S., SÖRENSEN, O., KARLSEN, F., ROGNE, H., HOVIG, E. & SIREVÅG, R. 2005 Parallel nanoliter detection of cancer markers using polymer microchips. *Lab on a Chip* **5** (4), 416–420.

HANSEN, C., SKORDALAKES, E., BERGER, J. & QUAKE, S. 2002 A robust and scalable microfluidic metering method that allows protein crystal growth by free interface diffusion. *Proceedings of the National Academy of Sciences of the United States of America* **99** (26), 16531–16536.

HONG, J. & QUAKE, S. 2003 Integrated nanoliter systems. *Nature Biotechnology* **21** (10), 1179–1183.

JENKINS, D. 2001 Diagnosing human papillomaviruses: recent advances. *Current Opinion in Infectious Diseases* **14** (1), 53–62.

JEON, N. L., BASKARAN, H., DERTINGER, S. K. W., WHITESIDES, G. M., VAN DE WATER, L. & TONER, M. 2002 Neutrophil chemotaxis in linear and complex gradients of interleukin-8 formed in a microfabricated device. *Nature Biotechnology* **20** (8), 826–830.

KOLIOPOULOS, G., ARBYN, M., MARTIN-HIRSCH, P., KYRGIOU, M., PRENDIVILLE, W. & PARASKEVAIDIS, E. 2007 Diagnostic accuracy of human papillomavirus testing in primary cervical screening: A systematic review and meta-analysis of non-randomized studies. *Gynecologic Oncology* **104** (1), 232–246.

LASER, D. J. & SANTIAGO, J. G. 2004 A review of micropumps. *Journal of Micromechanics and Microengineering* **14** (6), R35–R64.

MANZ, A., GRABER, N. & WIDMER, H. 1990 Miniaturized total chemical-analysis systems - a novel concept for chemical sensing. *Sensors and Actuators B-Chemical* **1** (1-6), 244–248.

MIELNIK, M. M. 2005 Micro-PIV and its application to some BioMEMS related microfluidic flows. PhD thesis, Norwegian University of Science and Technology (NTNU), Trondheim, Norway.

MIELNIK, M. M. & SÆTRAN, L. R. 2006 Selective seeding for micro-PIV. *Experiments in Fluids* **41** (2), 155–159.

NGUYEN, N. & WU, Z. 2005 Micromixers - a review. *JOURNAL OF MICROMECHANICS AND MICROENGINEERING* **15** (2), R1–R16.

NIJHUIS, E. R., REESINK-PETERS, N., WISMAN, G. B., NIJMAN, H. W., VAN ZANDEN, J., VOLDERS, H., HOLLEMA, H., SUURMEIJER, A. J., SCHUURING, E. & VAN DER ZEE, A. G. 2006 An overview of innovative techniques to improve cervical cancer screening. *Cell Oncol.* **28** (5–6), 233–246.

POLLACK, L., TATE, M. W., FINNEFROCK, A. C., KALIDAS, C., TROTTER, S., DARNTON, N. C., LURIO, L., AUSTIN, R. H., BATT, C. A., GRUNER, S. M. & MOCHRIE, S. G. J. 2001 Time resolved collapse of a folding protein observed with small angle x-ray scattering. *Physical Review Letters* **86** (21), 4962–4965.

19

PURCELL, E. M. 1977 Life at low Reynolds number. *American Journal of Physics* **45** (1), 3–11.

SALITERMAN, S. S. 2006 *Fundamentals of BioMEMS and Medical Microdevices*. Bellingham, WA: Wiley - Interscience.

SOLLI, L. A., GULLIKSEN, A., FURUBERG, L., SÖRENSEN, O., KARLSEN, F., SÆTRAN, L. R., ROGNE, H. & DRESE, K. S. 2007 A non-contact pump mechanism for parallel movement of nanoliter sized liquid plugs using flexible diaphragms. Manuscript for submission.

SOLLI, L. A., MIELNIK, M. M., KARLSEN, F., SÆTRAN, L. R. & FURUBERG, L. 2005 Flow visualization and simulation of discrete liquid droplets moving in microchannels. In *MekIT'05 - Thrid National Conference on Computational Mechanics (Trondheim, 11-12 May, 2005)*, pp. 281–296.

SOLLI, L. A., SÆTRAN, L. R. & MIELNIK, M. M. 2006 Numerical and experimental investigation of hydrodynamically focused sheets. In *Second International Conference on Transport Phenomena in Micro and Nanodevices (Barga, Italy, 11-15 June, 2006)*.

TERRY, S. C. 1975 PhD thesis, Stanford University, Stanford, CA.

WHITE, F. M. 1991 *Viscous Fluid Flow*, 2nd edn. McGraw-Hill, Inc.

ZHANG, C. S., XU, J. L., MA, W. L. & ZHENG, W. L. 2006 PCR microfluidic devices for DNA amplification. *Biotechnology Advances* **24** (3), 243–284.

Chapter 2

Theory

Lars A. Solli
Dept. of Energy and Process Engineering, NTNU.

This chapter gives a brief overview of the basic theory relevant to this thesis. Section 2.1 presents the most common fabrication methods of microstructures, from prototyping of test-devices to industrial mass production. The second section, sec. 2.2, presents the basics of cellular biology and the NASBA reaction. The third (sec. 2.3) introduces the fluid mechanics relevant to micro scale flows, whilst the last section (sec. 2.4) presents the mathematics behind the computational fluid dynamics involved.

2.1   Microfabrication

A variety of methods exist for the fabrication of lab-on-a-chip devices, including wet and dry etching (reactive ion etching and plasma etching), conventional machining (e.g. milling or sandblasting), photolithography, soft lithography, hot embossing, injection molding, casting, laser ablation, and *in situ* construction. In the following subsections, the most common methods used for the fabrication of polymer micro-devices are emphasized, together with the fabrication method of silicon-devices used in the work in this thesis. Sec. 2.1.1 to 2.1.2 provides a brief introduction along with advantages and disadvantages of the described method. As an enclosure, sec 2.1.3 presents all methods summarized in a table with typical fabrication capabilities (e.g. feature size and aspect ratio), along with production capabilities (e.g. speed and volume) and whether the methods are suitable for prototyping. Only the polymer, cyclic olefin copolymer (COC), is considered here, as it is the thermoplastic of interest, but the table may also serve as a good template for other thermoplastics. Typical values for the topical micromachining technique of silicon are also included.

Unless specified otherwise, the general information about microfabrication

presented herein may be found in textbooks such as Geschke *et al.* (2004), Li (2006), Minteer (2006), Nguyen & Wereley (2002), Senturia (2001), and reviews by Fiorini & Chiu (2005) and Becker & Locascio (2002).

2.1.1   Micromachining of silicon

The pioneer microfluidic devices consisted of silicon and/or glass. Channels in a silicon wafer with a glass lid on top were most common, but also glass lid on glass. The devices were fabricated using micromachining techniques borrowed from the semiconductor industry. Micromachining of silicon and glass is a generic term for 3D structure forming techniques such as wet and dry etch. These manufacturing processes also involve photolithography and electron beam lithography, among other techniques. The common factor is that they all require the use of clean-room facilities.

Dry etching of channels in silicon

Deep reactive ion etching (DRIE) is a common dry etching technique and a more advanced variant of the basic RIE (reactive ion etching) technique. Briefly, RIE is a technology using plasma to etch materials. The use of low-pressure glow-discharge plasma produces ions and neutral reactants, while an ion flux orthogonal to the wafer surface etches the silicon and anisotropic profiles can be obtained.

A typical process used, the so-called Bosch DRIE takes advantage of a side-effect of a glow-discharge, that is the tendency to create polymeric species by chemical cross-linking. These polymer species deposit on the wafer, covering all of its surface with a passivation layer. Figure 2.1 illustrates the DRIE of silicon with the Bosch process. In the process there are three primary steps. Fig. 2.1a illustrates the etch step, where neutral reactants in SF_6 plasma are used to perform a nearly isotropic etch on all exposed substrate. C_4F_8 source gas is used to deposit a Teflon-like passivation layer on all surfaces. Fig. 2.1b shows the deposition process. This polymer layer protects the substrate from further chemical attack and prevents further etching. In the third step (see Fig. 2.1c), the process returns to etching with SF_6 and combined with ion bombardment, it removes the passivation layer from all horizontal surfaces, but not from the vertical side-walls. By this means etching is preferentially in the vertical direction. The two latter etch/deposit steps are repeated many times, resulting in a large number of very small isotropic etch steps taking place only at the bottom of the etched pits. This process is called multicycling. Fig. 2.2 presents a silicon microchannel etched by the Bosch DRIE process.

The DRIE process described above is a commercially available technology from Bosch. The process produces features that are both optically smooth and have
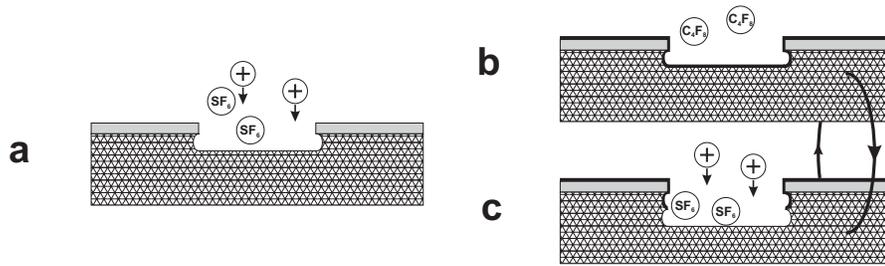
Figure 2.1: Sketch of the DRIE process. **a** Step 1: Etch **b** Step 2: Deposition **c** Step 3: Etch. The figure is most kindly provided by Preben Storås, SINTEF.
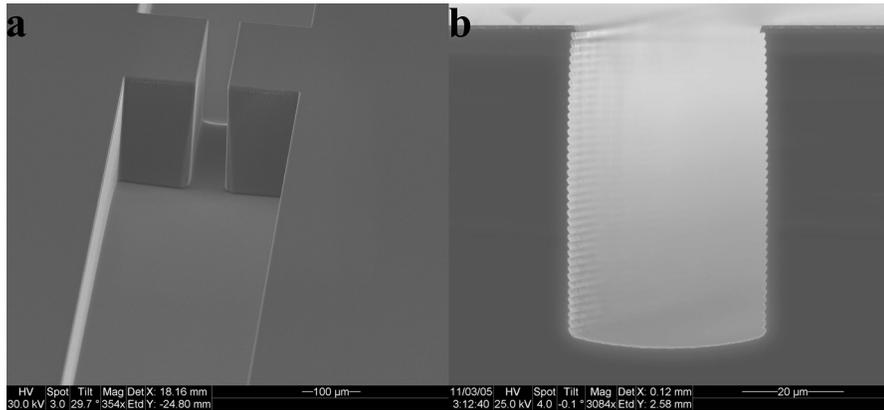
Figure 2.2: SEM (scanning electron microscope) photographs of microchannels in silicon. **a** Microfluidic channel network. **b** Cross section of a channel. A closer look at the sidewalls reveals scallops from the multicycling process. The photographs are most kindly provided by Preben Storås, SINTEF.

near perfectly vertical sidewalls, and is also capable of satisfying high aspect ratio requirements. If such high demands are not required, other and less expensive DRIE processes are also available. These processes employ different source gases and differ slightly from the above description, but the general principle is the same.

The manufacturing of silicon microstructures by any DRIE process is an expensive and not very flexible process, and thus not suited for rapid prototyping of test-devices. The technique is, however, well adapted for large-volume production of commercial products.

Anodic bonding of glass on silicon

Basically, anodic bonding is a method for sealing an alkali-rich glass to virtually any metal. It is the most commonly used method in microfabrication to join sodium borosilicate glasses like Corning #7740 (Pyrex), the glass used in this micro-device, to silicon substrates.

Anodic bonding is based on the movement of mobile alkali ions in the glass at high temperatures, driven by an external applied electrostatic field. A typical set-up is that of the silicon-glass device is fixated between a hotplate and an electrode. The device is heated, so the sodium ions become mobile, while voltage is applied to make the glass negative with respect to the silicon. The positive sodium ions drift towards the negative electrode, leaving a depleted layer in the glass. Most of the applied voltage drops across this layer and the electrostatic forces that develop pull the glass and silicon into close proximity. An electrochemical reaction occurs, resulting in covalent bonds between the surface atoms of the glass and the silicon.

2.1.2   Micromachining of polymer

Hot embossing

The process of hot embossing is presented in Figure 2.3. The technique is limited to thermoplastic materials, because of their ability to be reshaped when heated near the glass transition temperature of the material. The process is initiated by heating both the mould and the polymer to the glass transition temperature of the polymer. The mould is then pressed into the polymer workpiece, which takes on the shape and form of the master mould. Next, the mould and the polymer are cooled below the glass transition temperature to harden the polymer. Finally, the components are demoulded, leaving an inverted replica of the master mould in the polymer.

This heating and cooling of thermoplastics is known as thermocycling. This is a thermodynamic process which is not necessarily reversible. The thermoplastics in the hot embossing process might encounter structural stress formation due to poor alignment to the mould when cooled. Exposing the materials to processes such as mechanical cutting, milling, etc might also result in stressed structures. Thermocycling can then be applied to the polymers to relieve the stress. This process is known in material science as annealing (not to be confused with the biological explanation of the word. See sec. 2.2.4).

The master mould is typically made in either silicon or metal. The only criteria is that the material is able to sustain the temperatures and pressures used in hot embossing. A silicon master may be made using micromachining (see sec. 2.1.1), while a metal master can be fabricated using a variety of techniques, depending
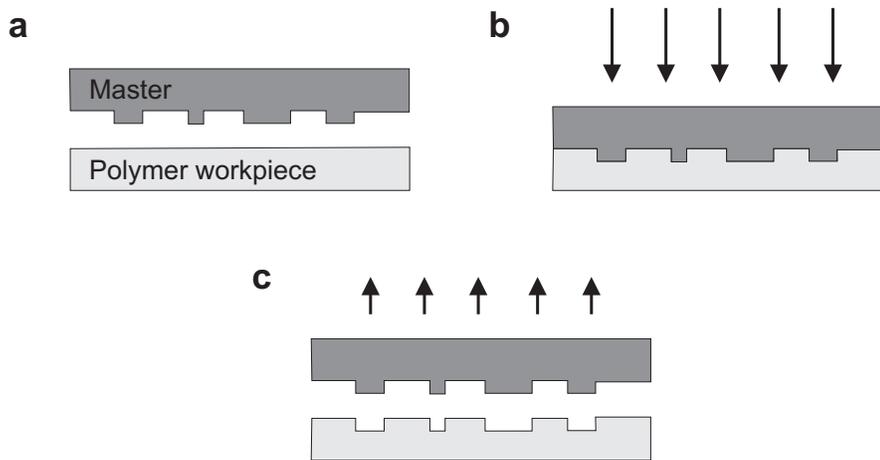
Figure 2.3: Sketch of the hot embossing process. **a** Step 1. The master mould and the polymer workpiece are arranged above each other and heated to the glass transition temperature. **b** Step 2. The master and workpiece are pressed together. **c** Step 3. The components are cooled and separated.

on the size tolerance of the microstructures. The most common ones are milling and electroplating.

Hot embossing is a fairly straightforward technique that does not require expensive equipment and can therefore be considered as a rapid prototype manufacturing technology. The master mould can be used repeatedly and the quality of the microstructure varies with access to hydraulic press equipment and well-defined temperature control. The limiting factor is however the manufacturing of the master mould. Depending on the high level of details on the micro device, making the mould can be a time-consuming process, and in such cases, hot embossing is not ideal for prototyping a few devices.

Injection moulding

Injection moulding is a common process in the existing plastic industry used to form a variety of everyday objects. The process is similar to that of hot embossing (see sec. 2.1.2) by the use of an inverted master mould. Injection moulding requires the use of melted prepolymerized pellets or granules of a thermoplastic, which is injected into the heated mould cavity under high pressure. The die is then cooled below the glass transition temperature of the material, which solidifies the polymer into the shape of the mould creating the part. Finally, the polymer microstructure can be released from the mould. Figure 2.4 displays a device made by injection moulding.
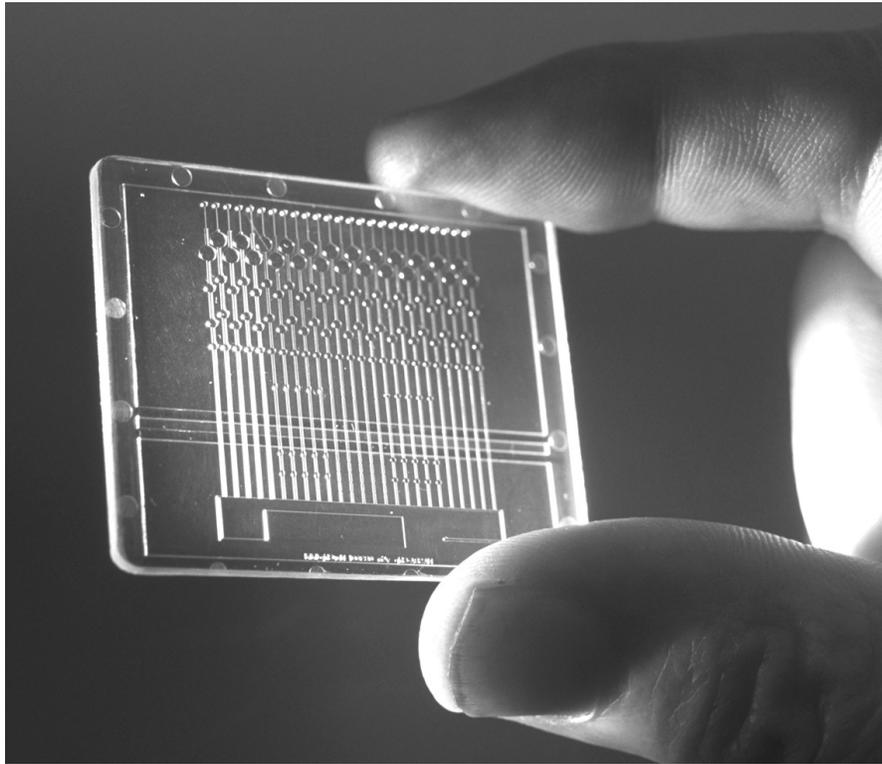
Figure 2.4: Picture of an injection moulded microstructure. The micro-device is the first prototype of the NASBA-chip of NorChip AS. The chip was made by IMM, Germany.

The equipment used for the injection moulding process is industry standard, but highly expensive. The quality of the polymer product is highly dependent on the master mould, which may be processed in the same manners as for hot embossing. However, the mould has to endure the high pressures that are used, which means that by far most moulds are made of metal. In addition, the liquid state of the polymer during injection permits excellent distribution within all features of the die, which may result in precise replication. To achieve this, parameters such as injection pressure and velocity, operating temperature and residence time must be optimized for each run. Once these parameters are optimized, injection moulding offers high-throughput (only seconds per piece) and large-volume production. The expenses involved make injection moulding not particulary ideal to prototyping of a few test devices, but for producing complex microfluidic test structures in numbers of hundreds, injection moulding should be considered due to its great quality of replication. The process is also considerably low-priced for large-volume production.

Milling

Milling or micromilling as it is often referred to, is a mechanical method used for complex shaping of metal and polymers. Its basic form is that of a rotating cutter or endmill which rotates about the spindle axis (similar to a drill), and a movable table to which the workpiece is affixed. This is usually the set-up of a manually operated milling machine. The opposite is present in most computer numerical controlled (CNC) milling machines, where the table is immobile and the spindle axis is computer controllable in three to five degrees of freedom. The CNC commands can easily be translated from computer-aided design (CAD) software, which is indispensable when producing complex microstructures.

The milling process is serial and a considerably slow machining technique, partly because the small endmill tools tend to be fragile and break easily. The production time also depends on the level of details within the microstructure, and should lie anywhere between minutes and few hours, depending on using a manual or CNC milling machine.

When working with polymers, milling can leave structural stress in the material. Like hot embossing, this can be relieved by annealing the structure. Hard polymers like thermoplastics are suitable for milling, whereas soft polymers like elastomers usually cannot be milled.

Milling is a flexible and straightforward micromachining technique. A manually operated milling machine is usually a part of the instrument park in an engineering workshop, and makes prototype manufacturing for plain structures possible, but a rather tedious and time consuming process. Access to a CNC milling machine, on the other hand, decreases the time spent on each piece drastically, but due to its serial nature, most likely not a high-throughput production.

Laser ablation

Laser ablation or laser micromachining is based on removing material from a surface by irradiating it with a laser beam. The set-up used for laser ablation looks very much like the CNC milling set-up (see sec. 2.1.2 Milling), which also enables the advances mentioned in the same section.

The light source in a laser ablation system usually consists of a high-intensity pulsed laser source, capable of pulse rates on the order of 10 - 10^4 Hz. The wavelength of the emitted radiation may range from the deep ultraviolet (UV) ($\sim$150 nm) to the infrared region (IR) ($\sim$10.6 μm) of the spectrum, depending on the material to ablate. For microstructures in polymer, a general rule is that the deep UV lasers are used to ablate transparent, non-doped polymers. Usually, excimer lasers are applied for this purpose. If the polymers are doped with dyes that absorb at particular wavelengths, solid-state lasers (such as Nd:YAG lasers)

or gas lasers (such as CO_2 lasers), that operate in the IR region of the spectrum may be used.

A metal mask can be applied to the workpiece so that designated areas can be protected and others exposed to the laser for ablation. Alternatively, a direct-write process using CNC may be employed.

The quality of the microstructures attainable with laser ablation depends strongly on the optical system, the movement of the stage, and the pulse rate, pulse duration and the wavelength of the laser. For instance, the beam velocity and the pulse rate of the laser requires careful optimization in order to achieve the best results. Otherwise, the ablated channels may easily have a rippled surface. Generally, laser ablated channels have greater surface roughness than hot embossed or injection moulded channels. The irradiated polymers might also change the chemical structure of the surface, thus changing the bio-compatibility of the material. The disadvantage of laser ablation is its intensity nature. The intensity of laser beams have a Gaussian profile, which severely limits the feature size of the channels if nearly vertical sidewalls features are required. Hence, additional optimization (e.g. a more advanced optical system or the employment of a mask) is required in order to avoid V-shaped channels.

Laser ablation for the fabrication of plastic microfluidic devices is advantageous for prototyping applications. However, the disadvantages of the high surface roughness and change of bio-compatibility, severely limits its impact when complicated features and sensitive chemicals are involved.

2.1.3   Characteristic fabrication details

Table 2.1 presents some representative fabrication details for the microfabrication techniques described in this section. All values are for COC polymer, except of the DRIE etch which is presented for silicon. The details are *typical* values, i.e. characteristic sizes that can be expected from a microfabrication workshop. Hence, the table is not describing the state-of-the-art technology or recent research results.

It is important to emphasize that for polymer microfabrication, combination of different techniques (e.g. milling and laser ablation) may be employed in order to achieve satisfying channel details.

2.2   Biochemistry

This section presents an overview of the basic theory of the biochemistry relevant to the NASBA reaction, in addition to explaining the reaction itself. First, the cell and its main components are introduced. Next, the cellular molecules and virus are presented. Finally, the NASBA reaction and a few detection methods for amplified

Table 2.1: Overview of the microfabrication methods presented and some of their characteristics. All values are for fabrication of COC polymer. The values are kindly provided by IMM, Germany, whilst the values for DRIE is kindly provided by SINTEF.

Method	Material	Feature size	Roughness	Aspect ratio	Rapid prototyping	High-throughput	Large-volume
RIE-etch[1]	Silicon, glass	$\sim 5~\mu m$	< 10 nm	20-30	–	+	+
Hot embossing	Thermoplastics, elastomers	$\sim 100~\mu m$	0.3 μm with polished dies	1-2 for 100-200 μm channels[2], 5 and more for bigger channels[2]	+[3]	–	–
Injection moulding	Thermoplastics	$\sim 100~\mu m$	0.3 μm with polished dies	1-2 for 100-200 μm channels[2], 5 and more for bigger channels[2]	–	+[3]	+[3]
Milling	Metal, glass, thermoplastics	$\sim 100~\mu m$	typically 5-10 μm, with liquid cooling: $\sim 2~\mu m$	for 100 μm mills: 1.5; for 200 μm mills: 2, for 300 μm mills and bigger: 5 and more	+	–	–
Laser ablation	All solids and liquids	$10 - 20~\mu m$	0.5-0.8 μm for small channels, $> 5~\mu m$ for bigger channels due to pulse rate	1.5-2 for small channels, more for bigger channels	+	+	+

[1]) Silicon as the material.
[2]) For milled moulds.
[3]) Requires mould made by milling or micromachining.

nucleic acids are addressed. It is important to emphasize that this section is written with the intension of giving people with no background in biology an overview of the NASBA reaction and its applicability in studying biological activities. The text is simplified, and some things are left out due to the scope of this thesis, not to mention that it is written by a non-biologist.

Unless specified otherwise, the general information about cellular biology presented herein may be found in textbooks such as Stryer (1995) and Madigan *et al.* (1997). A good exercise book for a non-biologist in Norwegian is Bjålie *et al.* (2003). The information about the NASBA technique, also unless specified otherwise, can be found in the the original paper by Compton (1991) and in the review by Deiman *et al.* (2002).

2.2.1   Cellular biology

The cell is the structural and functional unit of all living organisms, and is the smallest biological unit to maintain a self-contained metabolism. Some organisms, like a bacteria or an amoeba are single-celled or unicellular organisms. More advanced organisms, like ourselves, are multicellular. Multicellular organisms are composed of several different kinds of cells, which then again are exclusively designed to implement certain tasks. The cells that perform a similar function constitute of the various sorts of biological tissue of the organism, like the *epithelium tissue* (surface tissue), the *muscle tissue* and the *nervous tissue*. A group of tissues that perform a specific function is called an *organ* (e.g. heart, skin, bones). The human body consists of an estimated 10^{14} cells of approximate size 10 - 100 μm each. Despite the numerous functional differences of the tissue and organs of the human body (or the body of all animals, for that matter), the cells still have several common features.

Figure 2.5 illustrates a typical *eukaryote* cell, which makes up all multicellular organisms. Eukaryotic cells, in contrast to *prokaryotic*, are cells with nucleus. The prokaryote cell is nearly always unicellular and are far more primitive than those of eukaryotes. Most prokaryotes are bacteria. All eukaryotic cells have a *cell membrane* that envelops the cell and surrounds its internal fluid, the *cytoplasm*. The cell membrane has a double layer of *lipids* (hydrophobic fat-like molecules), which keeps water-soluble components from diffusing through the membrane while fat-soluble liquids can diffuse through unhindered. The cytoplasm is an aqueous solution, where salts, oxygen and cellular molecules or nutrients are dissolved. The insoluble constituents of the cytoplasm are *organelles* (such as the *mitochondria*, the *chloroplast*, *lysosomes*, *peroxysomes*, *ribosomes*), as well as complex cell membrane structures (e.g. *endoplasmic reticulums* and the *Golgi apparatus*). Similar to the human body the organelles are the organs of the cell, all adapted for performing one or more vital functions. One of the main
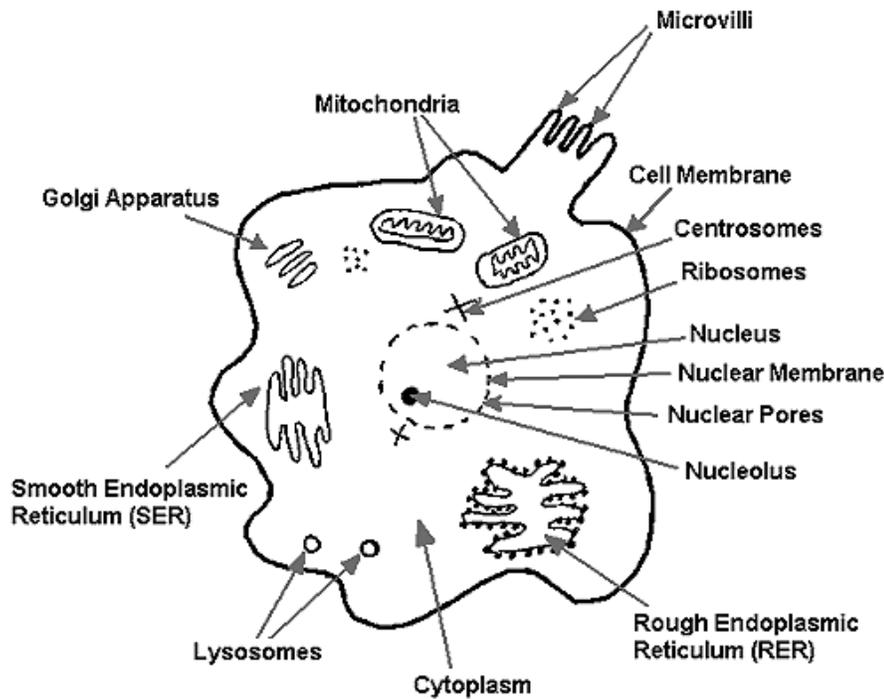
Figure 2.5: Diagram of an eukaryote cell.

characters and perhaps the most conspicuous organelle is the core of the cell, the *nucleus*. The nucleus is spheroid in shape and separated from the cytoplasm by a double membrane called the *nuclear membrane*. The nucleus accommodates all the information needed to repair the cell or make new cells, encoded in strings of DNA. All the actions of the cell are controlled by DNA that controls the synthesis of different proteins. To synthesize a desired protein, the nucleus sends RNA as "blueprints" to the ribosomes, which can be viewed upon as the protein production machines of the cell.

2.2.2 Cellular molecules

The following is a brief description of the most important cellular molecules that are involved in the thesis work. The two types of large molecules or *macromolecules* presented here, are the *protein* and the *nucleic acid*. These molecules are polymers, built by smaller molecules, or *monomers*, called *amino acids* and *nucleotides*, respectively. The *enzyme* is a type of protein and *DNA* and *RNA* are polymers composed of nucleic acids.

Amino acids

The amino acids can be thought of as the nuts and bolts of the structure of the cell. They are very small, around 10 - 30 Å in size (ten to thirty atoms). They all have a very similar end, a carboxyl group, that can easily bind or *polymerise* with others, making them easy to string together to form proteins. There are twenty standard[1] amino acids used by cells in protein biosynthesis that are specified by the general genetic code. Humans cannot synthesize nine of the standard amino acids, and these must be obtained from food. These are called *essential* amino acids, whereas the others are called *nonessential*.

A short chain of amino acids is called a *peptide*, and the chemical covalent bond that joins two amino acids is called a *peptide bond*. A long string of peptides such as a whole protein or large protein fragment is called a *polypeptide*.

Proteins

The proteins can be thought of as the workhorses of the cell. They are essential parts of all living organisms, as they participate in every process of the cell. Proteins are large organic compounds made of amino acids arranged in a linear chain. The amino acids are linked together by peptide bonds, and their sequence is specified by a gene encoded in the genetic code. Most proteins fold into unique three-dimensional structures. The mechanism of folding is complex, and yet not completely understood. The unwrapped state, where the protein is an unstructured strip, is known as the *denatured* form of the protein, which sometimes *renatures* to the active form, or *native state*. However, the folding structure can often be assumed having an approximate spherical shape. Based on this, proteins are in the range of 2–8 nm in radius (Jeon & Andrade, 1991).

Enzymes

Enzymes are proteins that accelerate, or catalyze, chemical reactions. These reactions would occur anyway, although they might take place so slowly that the organisms are in danger of having died first. Almost all processes in the cell need enzymes in order to occur at significant rates.

Enzymes are generally named after the reaction they catalyze. Usually the suffix *-ase* is added to the name of the substrate (e.g. *RNase* is the enzyme that catalyzes the breakdown of RNA into smaller components).

Enzyme activity can be affected by other molecules. Inhibitors are molecules that decrease enzyme activity, and activators are molecules that increase activity.

---

[1]There are a vast number of "nonstandard amino acids" which are not incorporated into proteins, e.g. some neurotransmitters.

Drugs and poisons are often enzyme inhibitors. Commercially, enzymes are used in e.g. household cleaning products (in biological washing powders to dissolve and remove fat stains on clothes).

Nucleotides and Nucleic acids

The nucleic acids can be thought of as the data-banks of the cell. Here is all the information necessary to build proteins, together with the expertise on how to store and when to pass on such information. Nucleic acids are the largest of the cellular molecules.

Nucleic acids are polymers composed of monomers called nucleotides, which consist of a sugar (ribose in RNA and deoxyribose in DNA), a phosphate and one of five kinds of bases. Nucleic acids may be single-stranded or double-stranded and the two most common are deoxyribonucleic acid (DNA) and ribonucleic acid (RNA). Nucleic acids are found in all living cells and viruses.

DNA

Deoxyribonucleic acid (DNA) is a long polymer chain of double-stranded nucleotides mostly stored in the cell nucleus. As Figure 2.6a shows, DNA has the shape of a double helix, and contains the genetic information of all cellular life. Each strand is a chain of chemical "building blocks", the nucleotides, of which there are four types: *adenine* (A), *cytosine* (C), *guanine* (G) and *thymine* (T). Each base forms hydrogen bonds readily to only one other base, A to T forming two hydrogen bonds, and C to G forming three hydrogen bonds. Figure 2.6b displays a sketch of the chemical structure of DNA. The unique combination of these four nucleotides composes genetic information or the "blueprints" of all information of the organism. A strand of DNA contains genes, areas that regulate genes, and areas that either have no function, or a function yet unknown. The total length of all DNA-molecules in a human cell is about 1.5 m, and the total length of all DNA in a human body is about 400 times the distance from the earth to the sun.

RNA

Unlike DNA, ribonucleic acid (RNA) is almost always a single-stranded nucleic acid polymer and has a much shorter chain of nucleotides. Deoxyribose is replaced by ribose, and the first three nucleotides are the same as those found in DNA. But in RNA *uracil* (U) replaces thymine as the base complementary to adenine. As explained before, the DNA stores all information required by the cell to synthesize the desired proteins. However, the DNA does not participate in the synthesis, which occurs at the ribosomes in the cytoplasm (see Fig. 2.5). The RNA serves as

a

1 turn = 10 base pairs = 3.4 nanometers

2 nanometers

major groove   minor groove

b

Adenine
Thymine

Guanine
Cytosine

phosphate
-deoxyribose
backbone

H-bond

3' end

5' end
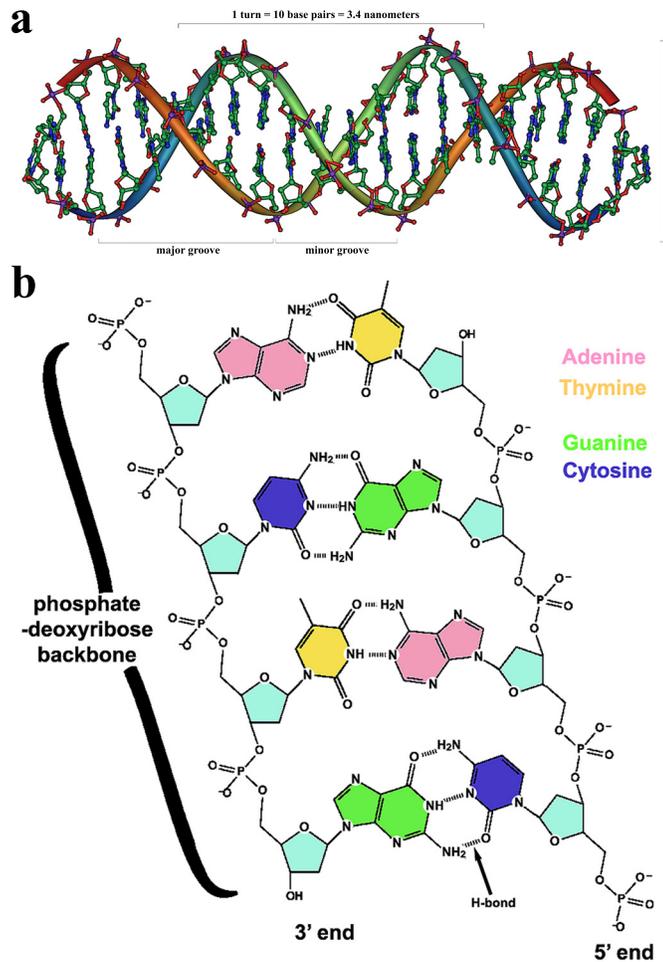
Figure 2.6: a Computer art of the general structure of a section of a DNA strand. Image is created by Michael Ströck. Released under the GFDL (GNU Free Documentation License). **b** Sketch of the chemical structure of DNA. The colour code of the four bases are shown on right hand side of the figure. The turquoise colour represents the sugar. Image is created by Madeleine Price Ball. Released under the GFDL.

a template for translation of genes into proteins, as well as an interpreter of the transcripts. Fig. 2.7 shows a sketch on how this process works.

The *messenger RNA* (mRNA) is a type of RNA molecule which purpose is to undergo the process in Fig. 2.7. Its short life begins with transcription in the nucleus, where it subsequently transports its genetic information from DNA to the cytoplasm and is translated one or more times by the ribosomes. It is inactivated and destroyed in a controlled manner. In addition to mRNA, other shapes of
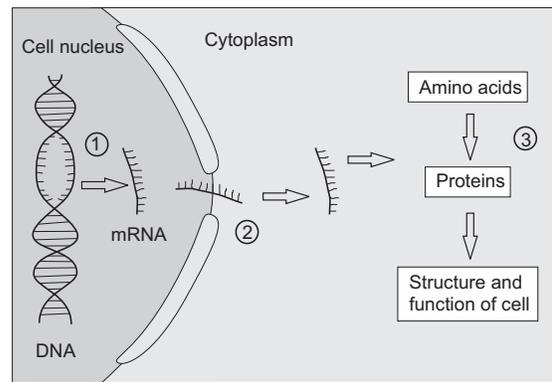
Figure 2.7: Transcription of genetic information. (1) In the core of the cell (cell nucleus) the DNA transfers information to the RNA. (2) RNA carries the information from the nucleus out to the cytoplasma. (3) Inside the cytoplasma, the RNA controls synthesis of proteins which subsequently mediates the biological effect in the cell.

RNA exist and are important to the genetic reconstruction. These are amongst others *transfer RNA* (tRNA), *ribosomal RNA* (rRNA), *catalytic RNA* and *double-stranded RNA* (dsRNA). The first three are involved in the protein synthesis at the ribosomes, while the latter forms the genetic material of many viruses.

2.2.3   Virus

A virus is the simplest type of an organism. It consists of short sequences of genetic material (DNA or RNA), enveloped in a protective protein shell called a *capsid*. The majority of viruses have diameters between 10 and 300 nm. There are arguments whether viruses are at all living organisms, and the answer is a matter of definitions. A virus does not metabolize on their own, and is therefore according to the cell theory not considered a living organism.

A virus can only live by infecting other organisms and reproduce by taking possession of their cells. Figure 2.8 illustrates a viral attack on a cell. On the right hand side of the illustration, the enclosing shell of the virus is broken down, the genetic material is released and forced into the cell nucleus. Inside the nucleus the virus exploits the infected host by controlling the cell's operations to replicate its own capsids and genetic material. This is illustrated in the bottom of the figure. The left hand side of the figure exhibits that the virus self-assembles into more viruses, which then in turn will infect other cells.
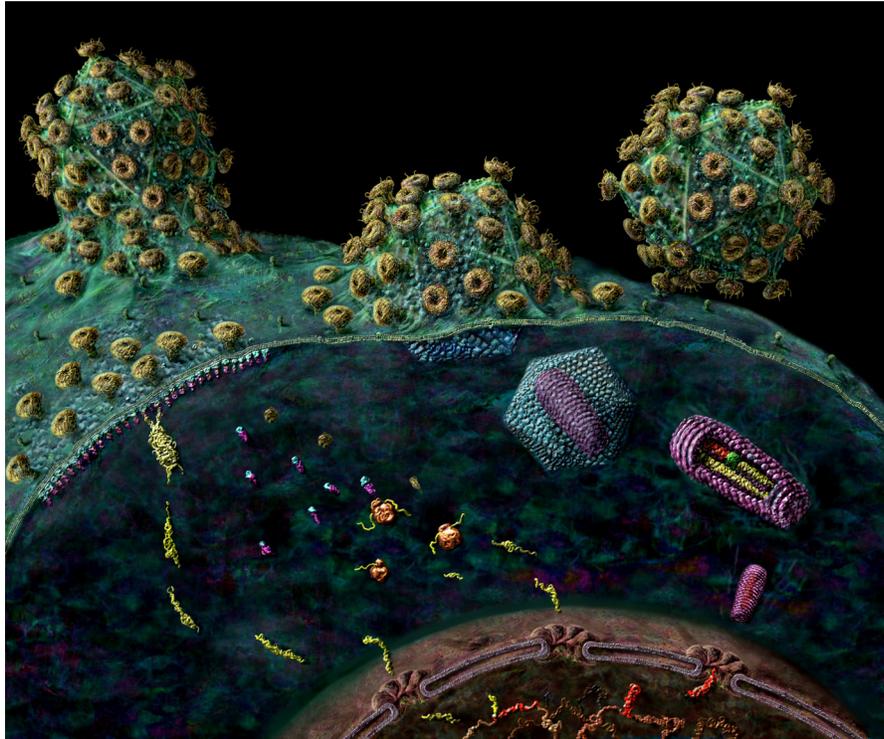
Figure 2.8: Computer art showing viral attack on a cell. Human Immunodeficiency Virus (HIV) particle (upper right) attaches to cell surface. The viral envelope merges with the cell plasma membrane (middle) releasing the matrix shell and core (purple bullet-shaped structure containing the viral genome) into the cell. The viral RNA (yellow string-like structure in core) is converted into viral DNA (red string-like structure in core) by the enzyme reverse transcriptase (green sphere). The viral genome is delivered to the nucleus (brownish sphere at bottom) and enters through a nuclear pore (flower-like opening). Once inside the nucleus, the viral DNA joins (integrates) with the host cell DNA. The viral DNA then directs the production of viral RNA which exits the nucleus through nuclear pores. Some viral RNA goes to form a new viral genome (yellow lump attached to underside of cell membrane at left) while other viral RNA directs the production of new viral proteins via ribosomes (3 brown spherical objects in middle of cell). The new viral components (genome + proteins) assemble at the cell surface (left) and a new virus particle buds from the cell (upper left). Image and text are properties of Russell Kightley Media (rkm.com.au). Used with permission.

2.2.4   NASBA detection of microbial targets

NASBA is an abbreviation of Nucleic Acid Sequence-Based Amplification and is an enzymatic amplification of nucleic acids. It is widely used in both medical research labs and in routine labs for a variety of different tasks, such as the diagnosis of

infectious (viral and bacterial) diseases. In general, detection of different RNA strands is applicable to all particles and cells that are biologically active. Detection of the amplified acids, the amplicons, can be carried out by several means addressed in the subsequent text.

NASBA components

In order to describe the NASBA reaction, the two following components need a general presentation.

Primers

A primer is a nucleic acid strand that serves as a starting point for DNA or RNA replication. The primer is required because the DNA and RNA polymerase (the enzyme that catalyzes the replication of DNA and RNA, respectively), can only start synthesizing a new DNA or RNA strand from an existing strand of nucleotides. The primer is a specific sequence (usually ∼50 bases) that will only hybridize to a corresponding region on a DNA or RNA strand. Primers are mainly made from DNA strands.
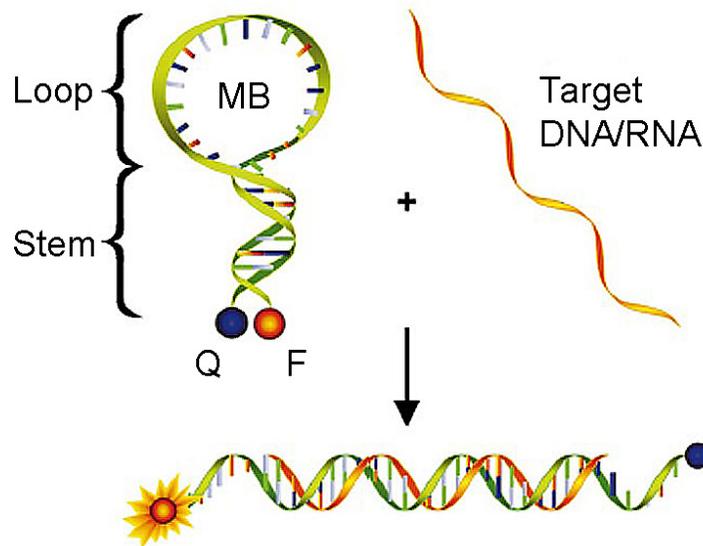
Figure 2.9: Conformational structure of molecular beacon probe. By maintaining the Fluorophore (F) and the Quencher (Q) in close proximity, the fluorescent signal is kept to a minimum. When introducing the target DNA/RNA to the molecular beacon, it undergoes a spontaneous conformational change forcing the stem apart, which consequently results in hybridization to the target and restoration of the fluorescence.

Molecular beacon probes

Molecular beacon probes (Drake & Tan, 2004) are *oligonucleotides* (short sequences of nucleotides (DNA)), typically with twenty or fewer bases. They serve as agents for detecting specific sequences of nucleic acids. A molecular beacon probe consists of a stem-loop structure (upper left in Fig. 2.9). The loop contains a specific sequence that will only hybridize to a corresponding sequence present on a DNA or RNA strand, while the stem contains a *Fluorophore* (F) and a *Quencher* (Q). Prior to hybridization the fluorescence is minimal due to the stem-loop structure of the beacon, maintaining the Fluorophore and the Quencher in close proximity, and static quenching is achieved. When introducing the target nucleic acid sequence to the molecular beacon, it undergoes a spontaneous conformational change forcing the stem apart. Consequently, the two moieties of the stem spatially separate and result in a restoration of the fluorescence. The process is illustrated in Fig. 2.9.

NASBA reaction and detection

NASBA was initially introduced by Compton in 1991 and is a sensitive, isothermal, transcription-based amplification system specifically designed for detecting RNA. The technology relies on the simultaneous activity of three enzymes (*avian myeloblastosis virus reverse transcriptase* (AMV-RT), *RNase H* and *T7 RNA polymerase*) at a fixed temperature of 41°C, to amplify the nucleic acid sequence of interest.

The key attribute in the amplification is the ability to make transcriptionally active double-stranded DNA that serves as "dummy-factories". Together, these DNA strands or "dummy-factories" are able to produce a vast number of amplicons. Figure 2.10 illustrates the principle of creating these DNA strands, which in turn produce amplicons.

1. The process is initiated by the localization of the complementary sequence range on the RNA target by Primer 1 with a T7 promotor attached (represented by the two non-binding bases in the figure). The primer anneals[2] to the target and the AMV-RT-enzyme adds additional complementary nucleotides along the target strand. It produces a *complementary DNA* (cDNA) copy of the RNA target, which together result in a double-stranded hybrid molecule.

2. The enzyme RNase H (recall sec. 2.2.2) recognizes this hybrid molecule and hydrolyzes (splits into two separate strands) the RNA portion of it, leaving a single-stranded DNA. This permits Primer 2, which is complementary to

---

[2]In biology the term annealing is consistent with a single-stranded nucleotide sequence pairing by hydrogen bonds to a complementary sequence, forming a double-stranded nucleotide chain.
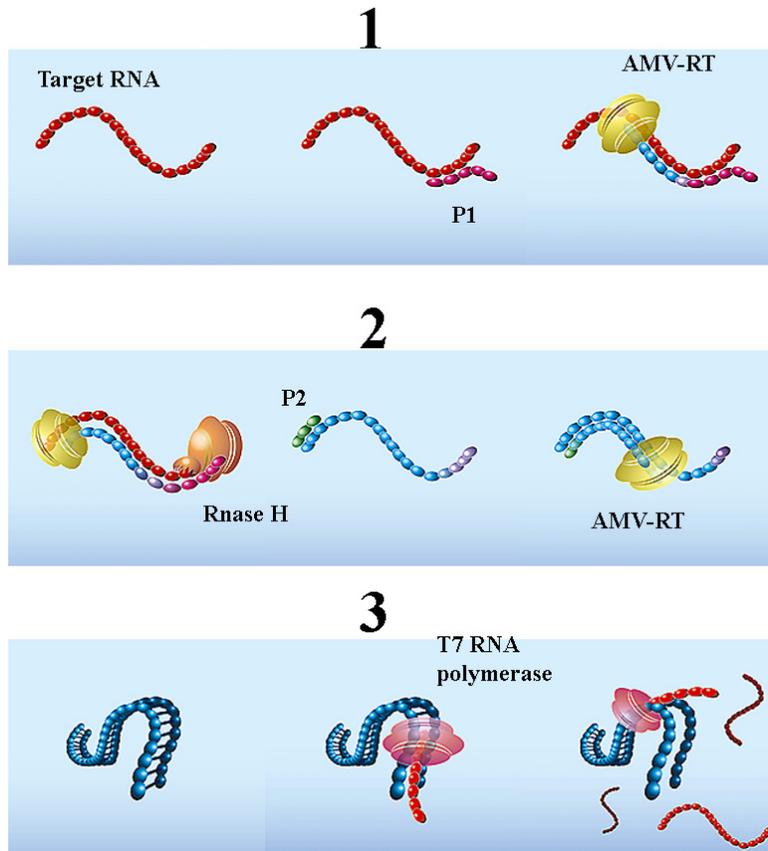
Figure 2.10: Illustration of the NASBA amplification principle. 1. Localization of the target RNA and annealing of Primer 1 results in a double-stranded hybrid molecule. 2. Primer 2 hybridizes and forms a double-stranded DNA copy of the original RNA. 3. RNA polymerase transcripts large amounts of antisense RNA. Image from www.norchip.com, with permission.

the upstream region of the RNA target, to anneal to the cDNA strand. Once again, the DNA-dependent DNA polymerase activity of AMV-RT is engaged, generating a double-stranded DNA copy of the original single-stranded RNA target with a T7 promotor at one end.

3. The reaction has made a double-stranded DNA, where one strand contains the sequence of the mRNA of interest. This strand has the T7 promoter as its first bases. The T7 RNA polymerase recognizes the T7 and transcripts an amplicon - an antisense, single-stranded RNA, which is a complimentary copy of the initial target RNA. The enzyme produces a large amount of the antisense RNA, about 10 to 1000 strands.
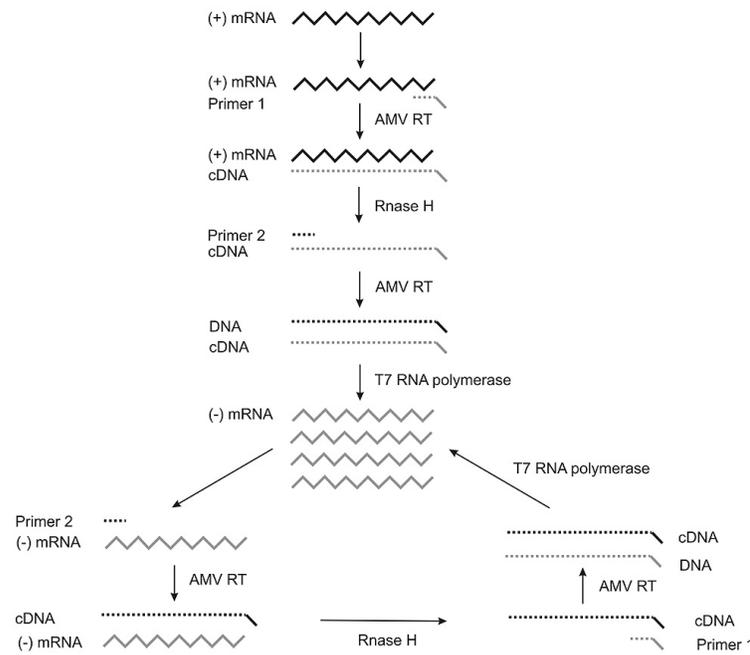
Figure 2.11: Overall description of NASBA amplification. Image from www.norchip.com, with permission.

These transcripts can then serve as templates for the overall amplification process, see Fig. 2.11. The top part of the figure covers the above description. The lower part illustrates how the transcribed mRNA strands in turn serve as templates for even more DNA strands in a similar process, however the primers anneal in reverse order. These new DNA strands will again transcribe even more mRNA. In NASBA, the RNA amplicons have an exponential increase in concentration as long as the primer concentrations are not rate limiting. The increase exhibits a linear growth after the primer pool is depleted. See e.g. Fig. 3.4 to observe the trend of a typical NASBA amplification curve.

The entire NASBA process is performed at 41°C, and the typical number of amplicons generated in 90 minutes is at least in order of 10^9. The amplification method is particularly well suited for analyses of various kinds of RNA: genomic RNA, mRNA, rRNA, viral RNA, and ssDNA. In some NASBA systems, dsDNA may also be amplified, albeit very inefficiently[3], and only in the absence of the corresponding RNA target. Based on this, the NASBA reaction has an application range including viral diagnostics, gene expression, and cell viability.

---

[3]For dsDNA, the process is the same except that an initial heat denaturing step is required before the addition of the enzymes to the reaction mix (100°C, 5 minutes).

The amplicons can be detected by several means. Until the end of the 1990's, *enzymatic chemiluminescence* (ECL), *enzyme-linked gel assay* (ELGA) and fluorescence correlation spectroscopy were the commonly used detection techniques. These methods were however either heterogeneous or they required additional handling of sample, implying that they were not cost-effective and had a low impact for high-throughput applications in routine laboratories (Leone *et al.*, 1998). In addition, due to handling procedures with open sample reservoirs, contamination was also an issue. The introduction of molecular beacon probes in 1998 by the group of Leone *et al.* revolutionized the the post-NASBA detection step (as well as other amplification techniques). The group included the molecular beacons in the reaction mixture prior to the amplification. The molecular beacon probes will consequently hybridize to the anti-sense RNA as these are being transcribed in the amplification process and emit light. Figure 2.12 illustrates the concept. This homogenizes the procedure, enabling a one-tube assay suitable for high-throughput applications for the macro-scale equipment in the routine laboratories, as well as the possibility of real-time monitoring of the reaction. The shift towards simplified operation and fully automated applications has a particularly large impact on the microsystem technology branch of NASBA applicability.
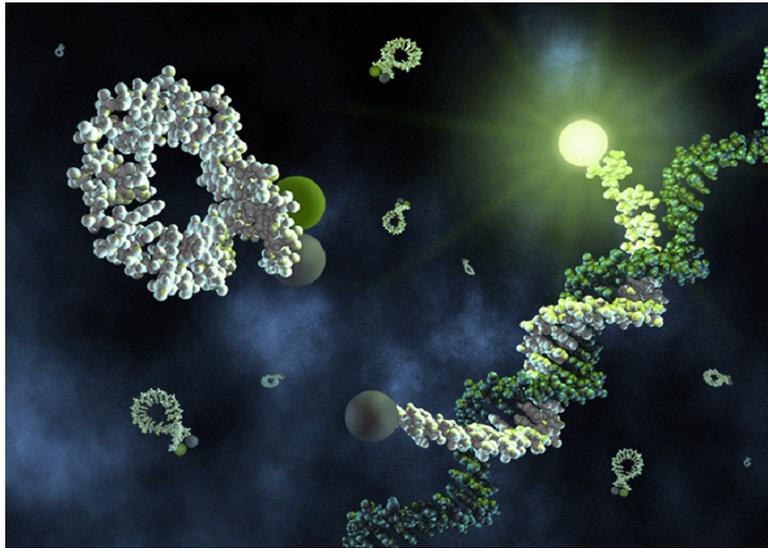
Figure 2.12: Computer art of several molecular beacon probes floating in a sample liquid. One probe has hybridized to a target RNA and its fluorophore emits light. Image from bioMérieux sa, Marcy l'Etoile, France.

To close the section, the most important advantages of NASBA are emphasized:

- NASBA is a completely isothermal reaction (i.e., does not require an expensive thermocycler) and thus facilitates miniaturization.

- The amplicons are single stranded and thus do not require an additional denaturation step prior to detection.

- The ability of NASBA to homogeneously amplify RNA analytes (e.g. tRNA, mRNA or rRNA) extends its application range from viral diagnostics to indication of biological activities such as gene expression and cell viability. This is in strong contrast to DNA amplification, where biological activity is not detected.

2.3   Fluid mechanics

This section presents an overview of the basic theory of the fluid mechanics relevant to microscale flows. First, the validity of the continuum hypothesis when downsizing and approaching microscale flow is discussed. Next, the governing equations of pressure driven channel flow are presented. Third, the diffusion-dominated mixing in microsystems are addressed. Finally, the aspects of two-phase flow where physical properties such as surface tension and contact angle are discussed.

Unless specified otherwise, the general information about presented herein may be found in sources such as Gad-el-Hak (1999), White (1991), and White (1994). While the information about the physics of surfaces may be found in textbooks such as Hiemenz (1986), Israelachvili (1991) and Adamson & Gast (1997).

2.3.1   The continuum hypothesis

In general and more precisely in a macroscopic perspective, fluids can be treated as continuous isotropic matter. The fact that matter is made of atoms and that it commonly has some sort of heterogenous microstructure is ignored in the simplifying approximation that physical quantities, such as density, energy and momentum, can be handled in the infinitesimal limit. Differential equations can thus be employed in solving problems as these quantities are described as averaged values over elements that are large compared to the molecular structure of the fluid. The continuum description could however be questioned because of the small length scales present in microfluidic flows.

For gases, the Knudsen number, a dimensionless number defined as the ratio of the molecular mean free path, λ, to a characteristic physical length, L, is commonly used to distinguish between flow regimes. It is defined as:

$$Kn = \frac{\lambda}{L}. \tag{2.1}$$

The different Knudsen number regimes for gas flow can be summarized as follows (Gad-el-Hak, 1999):

Continuum model with no–slip boundary conditions:	$Kn \leq 10^{-3}$
Continuum model with slip boundary conditions:	$10^{-3} \leq Kn \leq 10^{-1}$
Transition regime:	$10^{-1} \leq Kn \leq 10$
Free molecular flow:	$Kn > 10$

As the above describes, an increase of the Knudsen number will give rise to rarefaction effects in the gas and the continuum approach will eventually break down. The effects of molecular structure are quite different in gases and liquids. Because the density of liquids is about 1000 times the density of gases, the molecules of liquids are close-packed and are thus dominated by large intermolecular forces. Consequently, liquid molecules are more restricted in motion. They can position themselves in respect to each other and prove a tendency to pack into an ordered lattice. Hence, the expression mean free path has no meaning for liquid molecules. The lattice spacing, δ, may be used as a similar measure. It is defined as (Probstein, 1994):

$$\delta \sim \left(\frac{\bar{V}_1}{N_A} \right)^{1/3} \tag{2.2}$$

where $\bar{V}_1$ is the molar volume (i.e. ratio of the volume of the substance to the number of molecules (in moles) contained within that volume) and N_A is Avogadro's number ($N_A = 6.022 \times 10^{23}$ mol^{-1}). For water, with a molecular mass of $M = 18.02 \times 10^{-3}$ kg/mol and a density of approximately $\rho = 10^3$ kg/m^3, the molar volume is $\bar{V} \approx 2 \times 10^{-5}$ m^3/mol, resulting in a lattice spacing of $\delta \approx 0.3$ nm. By substituting this value with the mean free path, λ in Eq. 2.1 and solving for the characteristic physical length L, we have:

$$L = \frac{\delta}{Kn} \tag{2.3}$$

To satisfy the continuum approach with no–slip condition, $Kn \leq 10^{-3}$, the characteristic length of microchannel flow must reach the criteria of $L > 0.3$ μm. However, this assumption also implies that the continuum model with slip conditions ($10^{-3} \leq Kn \leq 10^{-1}$) is valid for description for liquid flow in microchannels as small as $L \sim 3$ nm.

A more intuitive way of validating the impact of the continuum description is through a precision criterion. At sufficiently high precision the fluids are never

continuous. An example could be to determine the mass density to a certain relative precision r. The concept of continuous mass density does only make sense for small changes of mass, i.e. the random fluctuation of molecules in a small characteristic volume V.

- **Example**

  Consider N number of molecules of a mass m in a small volume $V = l^3$. The mass density can be written as $\rho = mN/V$. There are only fluctuations in the relative number of molecules ΔN due to random walk which is typically $\Delta N \approx \sqrt{N}$. For $r = 1\%$ the requirement $\Delta N/N < r$ yields $N > 1/r^2 = 10^4$. The given volume hence needing dimensions $l = 22\delta$. For the case of water, where $\delta \approx 0.3$ nm, yields $l > 7$ nm.

Both the Knudsen number and the precision criterion approach satisfies the continuum description for the geometric channel dimensions used in this thesis, which are a factor of 10^5 larger. The liquid-gas interfaces has, however, a comparable thickness to the molecular scale δ. It is still reasonable to describe the two fluids involved as continuums, as the interface can be characterized as a discontinuous change from one isotropic continuum to another.

2.3.2 Governing equations for a single-phase flow

The general continuum description of the dynamics of an incompressible Newtonian fluid can be modeled by the Navier-Stokes equations. The governing equations of fluid flow are the continuity and momentum equations, which are given respectively, by

$$\nabla \cdot \boldsymbol{V} = 0 \tag{2.4}$$

and

$$\rho \frac{D\boldsymbol{V}}{Dt} = \rho \left(\frac{\partial \boldsymbol{V}}{\partial t} + \left(\boldsymbol{V} \cdot \nabla \right) \boldsymbol{V} \right) = -\nabla p + \mu \nabla^2 \boldsymbol{V} + \rho \boldsymbol{F} \tag{2.5}$$

where $\boldsymbol{V} = (u, v, w)$ is the velocity vector, ρ is the fluid density, μ is the absolute viscosity of the fluid, p is the applied pressure and $\boldsymbol{F}$ is an external force vector (i.e. gravitational, magnetic, etc.). The left hand side of Eq. 2.5 represents the inertial forces, while the right hand side represents the forces due to pressure, viscosity and applied external force. The viscosity is here considered a constant, i.e. Eq. 2.4 and Eq. 2.5 is uncoupled from temperature, and can be solved for $\boldsymbol{V}$ and p independently from the energy equation.

2.3.3 Microscale flow

The most important way of describing the pattern of flow, is by the Reynolds number. Typically it is given as follows:

$$Re = \frac{\rho U x}{\mu} \qquad (2.6)$$

where U is a characteristic flow velocity and L is a characteristic length (typically the smallest dimension of a channel). The Reynolds number is the ratio of inertial forces (ρU) to viscous forces (μ/x) and is also[4] used for determining whether a flow will be laminar or turbulent. Laminar flow occurs at low Reynolds numbers, where viscous forces are dominant, and is characterized by smooth, well-defined streamlines, while turbulent flow[5], on the other hand, occurs at high Reynolds numbers and is dominated by inertial forces, producing random eddies, vortices and other flow fluctuations. Microfabricated fluid systems usually involve small sizes and operate with low velocities, thus these systems are often in the low Reynolds number regime ($Re \ll 1$). Given this assumption, the inertial term of the momentum equation is neglected and Eq. 2.5 is reduced to:

$$\rho \frac{\partial \boldsymbol{V}}{\partial t} = -\nabla p + \mu \nabla^2 \boldsymbol{V} \qquad (2.7)$$

where the body forces have also been neglected. Equation 2.7 is also know as the creeping flow equation.

2.3.4 Diffusion

Due to the absence of inertial effects in microscale flows, mixing of two (or more) liquids is dominated by molecular diffusion. Diffusion is a transport phenomenon being the spontaneous spreading of matter (particles), heat, or momentum. A solution in equilibrium will seek uniform distribution of its molecules, generating concentration gradients throughout the solvent. The movement of molecules along a concentration gradient, i.e. from areas of high concentration to those of low, is called diffusion.

The Stokes-Einstein equation describes the way that diffusion increases in proportion to temperature, and is inversely proportional to the frictional force experienced by a molecule.

$$D = \frac{kT}{f} \qquad (2.8)$$

---

[4]The Reynolds number is a dimensionless number that provides a criterion for determining dynamic similitude.

[5]For pipe channel flow the transition to turbulent flow is approximately at $Re = 2300$.

Table 2.2: Examples of characteristic diffusion coefficients for spherical particles in water at 20°C.

	Potassium ion (0.2 nm)	Spherical protein (6 nm)	HIV virus (100 nm)	Red blood cell (7 μm)
Diffusion coefficient [m²/s]	1.1×10^{-9}	3.6×10^{-11}	2.1×10^{-12}	3.1×10^{-14}

where D is the diffusion coefficient, k is Boltzmann constant ($k = 1.38 \times 10^{-23}$ J/K), T is the temperature and f is a frictional constant. As both the Boltzmann constant and the temperature are known, all that is required to determine the diffusion constant is to find the frictional constant f. Determining this exactly is a matter for experimentation, but it can also be determined reasonably accurately on theoretical grounds for various polymer shapes and weights. Stokes' relation gives us a theoretical value for the frictional constant of a solid spherical particle in a liquid:

$$f = 6\pi\mu R \tag{2.9}$$

where μ is the viscosity of the liquid and R is the radius of the sphere. Substituting Eq. 2.9 into Eq. 2.8 gives

$$D = \frac{kT}{6\pi\mu R}. \tag{2.10}$$

The difficulty here (and where inaccuracy arises) is that the particle radius is not simply the physical radius of the molecule, but is rather the effective radius of the molecule, taking into account the effects of solvation (solvation is the layer of ordered water that the electric field of a protein causes to form around the protein). Also, the formula is strictly only accurate only for a single spherical particle. It can be modified easily to take account of prolate and oblate ellipsoids, but even these, like the sphere, are usually only approximations to the true shape of the particles. Table 2.2 displays examples of diffusion coefficients for some known particles (all assumed spherical). As Eq. 2.10 describes, the diffusion coefficient decreases as the radius of the particle increases.

The characteristic length scale for diffusion of a particle in a fluid in a given time, can be estimated from the Einstein-Smoluchowski diffusion equation. The equation relates the diffusion coefficient with the Brownian motion and is given as

Table 2.3: Examples of characteristic diffusion lengths and times for spherical particles in water at 20°C.

Diffusion length (μm)	Potassium ion (0.2 nm)	Spherical protein (6 nm)	HIV virus (100 nm)	Red blood cell (7 μm)
1	0.5 ms	14 ms	233 ms	16 s
10	47 ms	1.4 s	23 s	27 min
100	4.7 s	140 s	39 min	**45 hours**
1000	7.8 min	233 min	**65 hours**	**189 days**

$$D = \frac{\lambda^2}{2\tau}, \tag{2.11}$$

where λ is the length of the average "jump" between collisions and τ is the average time difference between collisions. The equation is derived for Brownian movement in one dimension only, but it serves as a reasonable estimate for diffusion times. By rearranging Eq. 2.11 and substituting λ with the characteristic length scale, L_d and τ with the characteristic time scale, t_d, the following can be found:

$$t_d = \frac{L_d^2}{2D}. \tag{2.12}$$

Eq. 2.12 describes the way that the characteristic diffusion time increases with proportion to the square of the diffusion length and is inversely proportional to the diffusion coefficient. Table 2.3 displays characteristic time required to diffuse a certain distance for the same spherical particles as in Table 2.2.

As mentioned above, mixing in microsystems may be a challenging task. The problem have received considerable attention over the years, and several methods have been developed and studied (see sec. 6.1 for an introduction).

Furthermore, an important way of describing the mixing is by the Péclet number, *Pe* (see sec. 2.3.7). This is a dimensionless parameter which relates convection with diffusion time.

2.3.5 Two-phase flow

Multiphase flows in microscale is common in many lab-on-a-chip or bioMEMS applications. First of all, many systems contain particles such as cells or viruses embedded in a liquid phase. Secondly, most systems require mixing of a sample liquid with one or more liquid reagents. Third, the forces between a gas and a

liquid interface, i.e. capillary forces, facilitates pumping mechanism, valve control or simply liquid handling. Further, the use of immiscible fluids to i.e. sheath fluid by means of transportation, route in channel network, and encapsulation of substances have shown many promising applications the recent years. The main focus of this discussion is liquid-gas flow, i.e. discrete liquid plugs in microchannels.

Multiphase flow introduces the physical properties surface tension and contact angle. The effects of these can be understood be studying Gibbs free energy G, the energy of systems where the thermodynamic control parameters are pressure p, temperature T, and particle number N. It is defined as $G \equiv G(p, T, N)$. The total Gibbs energy G of a system is given as a sum of several energy contributions G_i. In particular the focus is on equilibrium states, where the Gibbs free energy per definition is at minimum.

The physics and chemistry behind the surface tension and contact angle are not understood completely, however, they are applied in everyday products as e.g. ink-jet printers.
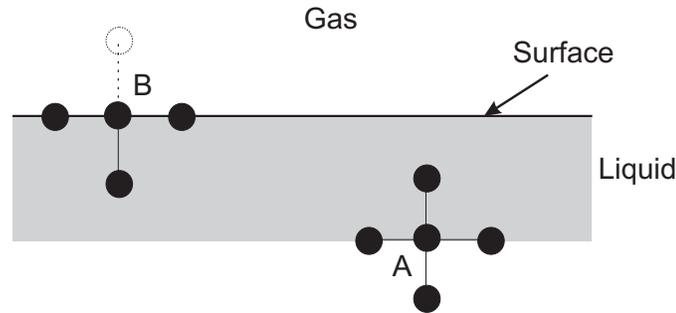
Figure 2.13: Sketch showing the surface tension of a liquid-gas interface. A molecule in the bulk of the liquid (A) forms chemical bonds with the neighbouring molecules, whilst a molecule at the surface (B) misses the chemical bond in the direction of the gas. Consequently, the energy of the surface molecules is higher than that of bulk molecules, and the formation of a surface requires energy.

Surface tension or interfacial energy

Surface tension or interfacial energy is energy per area of an interface between two phases, whether they are solids, fluids, or gases. Consider the situation in Fig. 2.13, where a microscopic model of a liquid and a gas is sketched. The liquid, not being able to expand, will form an interface towards the gas. The molecules in the bulk of the liquid (molecule A) form chemical bonds with the neighbouring, thus gaining a certain amount of binding energy. At the liquid-gas interface the molecules (molecule B) cannot form as many bonds since there are comparatively

few molecules in the gas. This absence of bonds in the direction of the surface results in a higher energy for the surface molecules. Energy or work is required to move molecules from the bulk to the surface, hence the name surface tension. In order to minimize the Gibbs free energy of the system, the liquid surface will tend to contract to minimize its surface area. This tends to create spherical surfaces - energy efficient surfaces. This example is given for a liquid-gas system, but the same applies at the interface of two immiscible liquids. The state of tension at the interface is then termed interfacial tension. The surface tension (and interfacial energy) γ is defined as

$$\gamma \equiv \left(\frac{\partial G}{\partial A}\right)_{p,T}, \tag{2.13}$$

where G is the free energy of the surface, A is the surface area, and p and T are the fixed pressure and temperature, respectively. The measured value for the water-air interface at $20°$ is 72.9 mJ m^{-2}. Table 2.4 presents some typical values for surface tension of given liquids.

Table 2.4: Data for static measured surface tension in air.

Liquid	$\gamma[\text{mJ/m}^2]$	Ref.
Blood (37°C)	58	Hrncir & Rosina (1997)
Glycerin (20°C)	48.09	Adamson & Gast (1997)
Glycerin (24°C)	62.6	Adamson & Gast (1997)
Mercury (20°C)	486.5	Adamson & Gast (1997)
Methanol (20°C)	22.5	Adamson & Gast (1997)
Water (20°C)	72.94	Adamson & Gast (1997)
Water (100°C)	60.58	Hiemenz (1986)

The Young-Laplace equation As described in the previous section, an interface will have a tendency to curve due to existence of surface tension. When the interface rests in thermodynamic equilibrium, the intermolecular forces acting must be balanced by a pressure difference Δp across it (the highest pressure on the concave side). An expression for the pressure difference can be found by considering the energy required to expand a curved surface. Consider the sketch in Fig. 2.14, where a small section of an arbitrary surface is depicted. When displacing the surface outwards by a small distance δr, the resulting change in surface area is:

$$\delta A = \left(\frac{1}{R_1} + \frac{1}{R_2}\right)\delta r A_0, \tag{2.14}$$
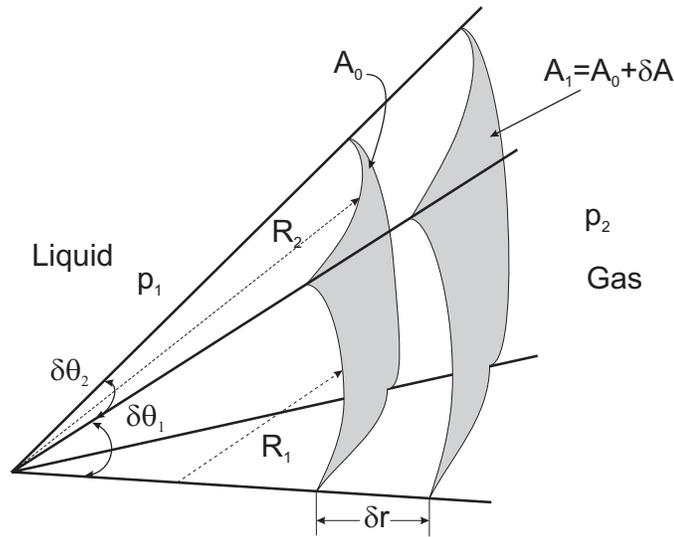
Figure 2.14: Differential expansion of a small section of an interface with locally constant curvatures.

where δr is assumed small ($\delta r^2 \ll 0$).

There will be two contributions to the change δG in the free energy of the system. An increase in free energy of the surface due to enlargement of the surface area,

$$\delta G_{surf} = \gamma \delta A = \gamma \left(\frac{1}{R_1} + \frac{1}{R_2} \right) \delta r A_0, \tag{2.15}$$

and a decrease in pressure energy due to the change in volume,

$$\delta G_{pressure} = -(p_1 - p_2)\delta V = -\Delta p \delta r A_0. \tag{2.16}$$

Where $\delta A \delta r \ll 0$. Thermodynamic equilibrium requires that net change of free energy equals zero, hence:

$$\delta G = \delta G_{surf} + \delta G_{pressure} = 0. \tag{2.17}$$

By inserting the expressions Eq. 2.15 and Eq. 2.16 into Eq. 2.17, results in the Young-Laplace equation

$$\Delta p = \gamma \left(\frac{1}{R_1} + \frac{1}{R_2} \right) = \gamma 2H, \tag{2.18}$$

where H is the mean curvature[6].

---

[6]$H = \frac{1}{2}(\frac{1}{R_1} + \frac{1}{R_2})$

50

Δp is the pressure difference required to sustain the curvature resulting from the surface tension. It is defined positive and is thus the pressure at the concave side minus the pressure at the convex. For a spherical droplet, where $R_1 = R_2 = R$, the pressure difference becomes

$$\Delta p = \frac{2\gamma}{R}. \tag{2.19}$$

Note that the pressure is highest inside the droplet.

Furthermore, for large scale surfaces, e.g. a pond, the pressure difference is negligible as R_1 and R_2 tend to infinity. However, in microscale, Δp becomes extremely important as R_1 and R_2 may tend to zero. Further arrangements of the equation will be discussed in the section involving capillary forces in microsystems, sec. 2.3.5.

Contact angle

The contact angle is defined as the angle θ at which a liquid/gas interface meets a solid surface, as the sketch in Fig. 2.15a shows. The theoretical description of contact arises from the consideration of a thermodynamic equilibrium between the three phases: the liquid phase of the droplet (L), the solid phase of the substrate (S), and the gas phase of the ambient (G). The gas phase might also be another (immiscible) liquid phase. Here, it is more convenient to address the terms as interfacial energies, i.e. the solid-gas interfacial energy as γ_{SG}, the solid-liquid interfacial energy as γ_{SL} and the liquid-gas energy (i.e. the surface tension) as simply γ.
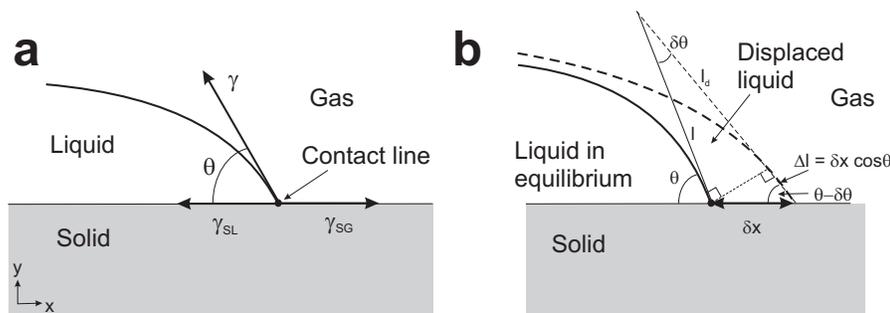
Figure 2.15: a Components of interfacial tension needed to define the contact angle. **b** Sketch of a small displacement δl of the contact line away from the equilibrium position.

The Young equation The contact angle is formed from a minimum configuration of these interfacial energies. The sketch in Fig. 2.15b shows the same situation

as Fig. 2.15a except that the interface is tilted an infinitesimal displacement δx. The change in Gibbs free energy per unit length $\frac{1}{L}\delta G$ along the contact becomes,

$$\frac{1}{L}\delta G = \delta x(\gamma_{SL} + \gamma) - \gamma_{SG}\Delta l = 0, \tag{2.20}$$

where a sine approximation and a rearrangement gives

$$\gamma \cos\theta = \gamma_{SG} - \gamma_{SL}. \tag{2.21}$$

Eq. 2.21 is known as the Young's equation and was first published in 1805. In general, the contact angle plays the role of a boundary condition.

Absorption and adhesion   Adamson & Gast (1997) points out that the phases are mutually in equilibrium and thus the interfacial energy γ_{SG} should in fact be given as

$$\gamma_{SG} = \gamma_{SG}^0 - \pi^0, \tag{2.22}$$

where π^0 is the change in interfacial free energy due to absorption. This is a reminder that the solid surface must be in equilibrium with the saturated vapour pressure p^0 and that there must be an absorbed film of film pressure π^0. The change π^0 can also be found from the Gibbs free energy (recall that G is also a function of the number of particles N). It relates to changes in the solid-gas interfacial free energy with changes of the substances at the solid surface. This interfacial energy changes with the absorption of gas molecules, it is dependent on the relation between the gas pressure p and the saturated vapour pressure p^0. For constant temperature π^0 is given as

$$\pi^0 = \frac{RT}{\Sigma} \int_0^{p^0} nd(\ln p), \tag{2.23}$$

where the surface excess per square centimeter Γ is just $\frac{n}{\Sigma}$, n is moles absorbed per gram and Σ is the specific surface area. The ideal gas law is considered in the above expression.

   Furthermore, Hiemenz (1986) defines the work of adhesion, W_{SL}, as the difference between the final and initial free energies of the solid-liquid contact line. It is given as

$$W_{SL} = \gamma + \gamma_{SG} - \gamma_{SL}. \tag{2.24}$$

The relation is simply work required to separate one unit area solid-liquid into one unit area solid-gas and one liquid-gas. Finally, Young's equation (Eq. 2.21) may be used to simplify the above expression

Table 2.5: Data for static measured contact angle in air at 20–25°C. All data, except where indicated, are from Adamson & Gast (1997).

Liquid	Solid	θ [deg]
Water	Gold	0
Water	Glass	25
Water	PMMA	59.3
Water	Human skin	90, 75[1]
Water	COC	94.9[2]
Mercury	Glass	128–148

[1]) Not cleaned of natural oils.
[2]) Own measurements with deionized water.

$$W_{SL} = \gamma(1 + \cos\theta). \tag{2.25}$$

Wetting and non-wetting Young's equation may be written in yet another form

$$k = \frac{\gamma_{SG} - \gamma_{SL}}{\gamma} = \cos\theta, \tag{2.26}$$

where k is the wetting coefficient. Eq. 2.26 requires that $-1 \leq k \leq 1$ only, i.e. it is not limited by the magnitudes of any of the interfacial energies. Systems with $0 < k < 1$ are called hydrophillic ($\theta < 90°$), while those with $-1 < k < 0$ are called hydrophobic ($\theta > 90°$). The limiting cases of $k = 1$ and $k = -1$, are referred to as total wetting and completely un-wetted, respectively. The latter limit is an un-physical state. Table 2.5 gives an overview of measured static contact angles of various liquids and solids in air at 20–25°C.

Contact angle hysteresis The contact angle has in the previous section been described as a stable and static quantity. This is in general not true as contact angles may be metastable and differ from the Young equation description. This is the phenomenon of contact angle hysteresis. The general observation is that the contact angle on a liquid advancing θ_A on a surface is different from one receding θ_R from a surface. This difference $\theta_A - \theta_R$, is the contact angle hysteresis. Fig. 2.16a shows a schematic diagram of this effect. An everyday example is the "teardrop" shape of a raindrop moving down a windowpane, see Fig. 2.16b. This difference can be as large as 50° for water on mineral surfaces. This makes the surface properties

of microdevices extremely important. The chemistry of the surface can be altered by processes such as coating the surface with a liquid with desired properties.
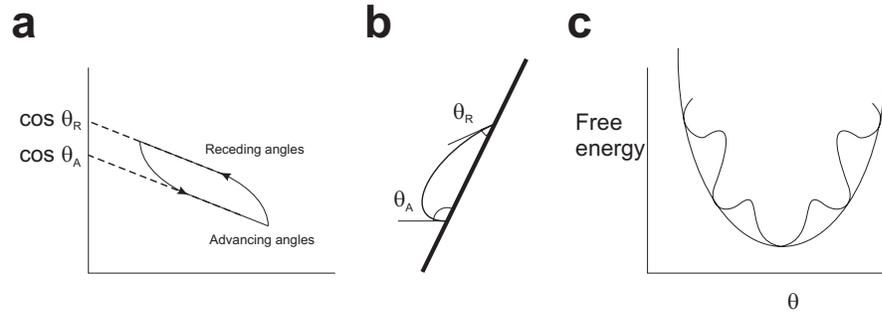
Figure 2.16: a Schematic diagram of advancing and receding contact angles. **b** A drop on a tilted plane, showing advancing and receding contact angles. **c** Schematic energy diagram for metastable states corresponding to different contact angles.

This effect is not yet fully understood, but is generally attributed to surface heterogeneity, surface roughness, solution impurities on the surface, or the contact angle as a dynamic quantity. It is not yet clear whether, like other hysteric phenomena (such as found in magnetism), contact angle hysteresis can be described by irreversible transitions or "jumps" between domains of equilibrium states (Marmur, 1994). The following provides an brief description of the main features of the four attributes.

A. Heterogenous surfaces Surfaces having impurities over distinct separate areas can be modeled with the Cassie equation

$$\cos \theta = f_1 \cos \theta_1 + f_2 \cos \theta_2, \tag{2.27}$$

where f_1 and f_2 are the two fractions ($f_1 + f_2 = 1$) of surface occupied by impurity with contact angles θ_1 and θ_2, respectively. Adamson & Gast (1997) also purpose to weight the two impurity areas by

$$(1 + \cos \theta)^2 = f_1(1 + \cos \theta_1)^2 + f_2(1 + \cos \theta_2)^2. \tag{2.28}$$

The validity of Eq. 2.27 and Eq. 2.28 depends on the given situation.

Heterogeneous surfaces cause metastable equilibrium states of the system, allowing for multiple contact angles. Traversing across such a surface, the contact line has a tendency to pin to the areas of the different material. Thus, the contact line must overcome energy barriers, which in turn shows up as a hysteresis effect. This is illustrated in Fig. 2.16c.

B. Surface roughness The effects of a rough surface can be modeled by the Wenzel equation

$$\cos\theta_{rough} = r\cos\theta_{true}, \qquad (2.29)$$

where r is the ratio between the area and the projected area, and θ_{true} is the ideal angle found in the Young equation (Eq. 2.21). The basic idea is that the projected (or apparent) area $A_{apparent}$ is related to the actual area $A_{true} = rA_{apparent}$, where $r > 1$. Hence, Eq. 2.29 implies that contact angles less than $90°$ are decreased, while angles greater than $90°$ are increased by surface roughness. Furthermore, an interesting situation is when air is trapped by liquid in the roughness grooves or pits. The combination of Eq. 2.27 and Eq. 2.29 yields

$$\cos\theta_{apparent} = rf_1\cos\theta_1 - f_2, \qquad (2.30)$$

where the un-wetted bottoms of the pits or grooves have $\cos\theta_2 = -1$ as $\theta_2 = 180°$.

The surface roughness is not strictly dependent on r but is also a matter of topology: parallel grooves and pits may have the same roughness, but exhibit an entirely different behaviour.

C. Liquid-surface interactions The third set of causes for hysteresis arise when specific interactions between the liquid and the solid appear. A liquid moving on a surface may alter its molecular structure through chemical interactions. Hence, the contact angle may be changed for both the receding as well as the advancing case.

When a surface-active agent is present in the liquid, it can absorb to the surface, lower the interfacial energy of the surface, and cause the contact angle to increase. This phenomenon is called *autophobicity*. In the limiting case this phenomenon can cause a traversing liquid to advance on the surface, then to retract because it no longer wets the surface.

This interaction may play a role in reproducibility of e.g. valves in microdevices. The alteration is usually time dependant.

D. Dynamic contact angle The description of contact angle hysteresis so far has revealed the involvement of liquid in motion across a solid surface, hence the contact angle cannot be viewed as simply a static quantity. The angle becomes dependent on the speed which the three-phase line advances or recedes: the angle is dynamic.

The key element is to model the boundary condition with a singularity moving at the three-phase line. Adamson & Gast (1997) mention two main approaches to treat the case:

- A fluid-solid interface with a slip boundary condition near the contact line.

- A thin immobilized liquid film that precedes the contact line. The contact angle is thus defined between the surface and the thin film.

Here, the theory is not anymore solely based on thermodynamics and energy considerations. These approaches requires among others detailed theory of molecular interactions as they move into the regime of molecular flow (recall sec. 2.3.1), and will not be discussed any further in this work.

However, a method of characterizing the speed of contact line motion is by the dimensionless parameter the capillary number, Ca (see sec. 2.3.7). Ca is the relative ratio of viscous and surface tension forces of the system.
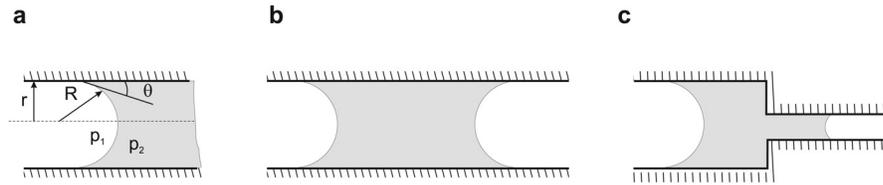
Figure 2.17: Interfaces between liquid and gas in microchannels. The liquid is coloured grey. The channel is either of circular or rectangular cross sections. The circular is shown in a. The rectangular is not shown, but h and w are the height and the width, respectively. The width is perpendicular to the text plane. **a** The driving front of a liquid plug. **b** Liquid plug in equilibrium. **c** Liquid plug in nonequilibrium.

Capillary forces in microsystems

In this section some variations of the Young-Laplace equation (Eq. 2.18) for specific channels are listed. In the microdevices used in this work, the channels are usually of rectangular cross sectional shape, due to the processing techniques (recall sec. 2.1), but circular cross sections might also occur (e.g. in connecting tubings, etc.). Figure 2.17a illustrates an interface between a liquid (grey) and a gas (no colour) in a circular microchannel. The curvature of the interface R can in this case be expressed as $R = r/cos\theta$, where r is the radius of the microchannel. In a similar manner can the curvature for a rectangular shaped cross section be expressed as $R = (1/h + 1/w)/\cos\theta$, where h and w is the height and width of the channel, respectively. Fig. 2.17b presents a liquid plug in a microchannel, where the two menisci of the plug are equal in size and the plug rests in equilibrium. Tab. 2.6 presents the equations for the case of the driving meniscus in Fig. 2.17a and the case with the plug in equilibrium in Fig. 2.17b for both rectangular and

Table 2.6: A list over variations of the Young-Laplace equation (Eq. 2.18) for channels with different cross sectional shapes.

Case	Circular	Rectangular
One meniscus	$\Delta p = \frac{2\gamma \cos \theta}{r}$	$\Delta p = 2\gamma \cos \theta \left(\frac{1}{w} + \frac{1}{h} \right)$
Two menisci	$\Delta p = 2\gamma \cos \theta \left(\frac{1}{r_1} - \frac{1}{r_2} \right)$	$\Delta p = 2\gamma \cos \theta \left[\left(\frac{1}{w_1} + \frac{1}{h_1} \right) - \left(\frac{1}{w_2} + \frac{1}{h_2} \right) \right]$

circular cross sections. The pressure difference across the two menisci in Fig. 2.17b is zero. For illustrative purposes Fig. 2.17c presents a liquid plug that is not in equilibrium. The pressure difference across the two menisci in this case is non-zero. The pressure is higher on the right side meniscus than the left, resulting in a force that will pull the plug towards the right.

2.3.6 Pressure changes and evaporation in microchannels

In microsystems involving liquid plugs enclosed by gas one has to take into account the effects of pressure changes due to heating of the system and evaporation of the liquid. Consider the case shown in Fig. 2.18a, where a liquid plug (grey) rests in equilibrium in a microchannel at 25°C. The channel is closed at the left side and open to atmospheric pressure at the right side. The liquid plug is able to move freely in the channel. Now, imagine that the surrounding gas is not air, but the vapour form of the liquid (considered an ideal gas). As Fig. 2.18b shows, the enclosed volume to the left of the plug increases by a volume ΔV when the microchip is heated from 25°C to 41°C. The displaced volume ΔV has two contributing effects, one from the thermal expansion of an ideal gas and one from the increase in the vapour pressure of the liquid. The plug moves out of the channels and will again reside in a position where the pressures in the front and back of the plug equals each other.

Now, consider again the situation in Fig. 2.18a, where the plug rests in constant temperature (not confined to this specific temperature). If the gaseous phase is not in equilibrium with the liquid phase, the liquid will evaporate until the gaseous phase is saturated with molecules from the liquid. In this situation, both menisci of the plug will experience evaporation into each respective reservoir, resulting in shrinkage of the plug volume. The gas to left of the plug will expand until saturation is met and cause the plug to move a displaced volume ΔV to the right. This distance is dependent on the size of vapour pressure increase. The right
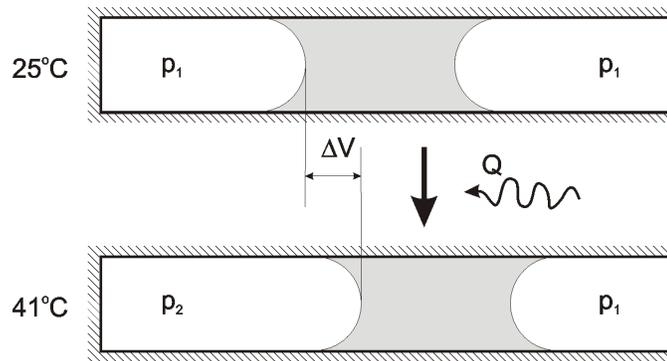
Figure 2.18: A liquid plug (grey) in a microchannel. The left side of the channel is closed, while the right is open to atmospheric pressure. **a** The system is in equilibrium at 25°C. **b** The system is heated to 41°C.

meniscus will experience evaporation until the outside environment is saturated, which in general when involving μl volumes is unlikely to happen before the plug has disappeared completely.

There are, however, three aspects that evolve from this discussion that are important to emphasize. They are described in the following.

- **Saturated vapour**
  In the discussion above, the dissolved amount of molecules in the gas contributes to the total plug movement and plug volume loss. By ensuring that the gas inside the microchannel is saturated before the liquid is applied, evaporation should be avoided at a constant temperature situation. This requires that the liquid, the gas and the microdevice have the same temperature. This also has an effect in the case where the temperature increases. When the pressure of the vapour at 25°C is already at its threshold, the saturated vapour pressure of that temperature, the increase to saturated vapour pressure of 41°C is limited to the difference between these two saturated vapour pressures only. For e.g. water, having a span of saturated vapour pressures of 3.173 kPa at 25°C and 7.957 kPa at 41°C, this becomes particularly important (values from Moran & Sharpiro (1998)).

- **Dead volume**
  The dead volume in Fig. 2.18a is the gas volume to the left of the plug. If this volume is minimal, the amount of molecules that evaporate from the liquid is also minimal, which results in a limited liquid volume loss.

- **Distance to ventilation**
  Some systems are required to have ventilation, which generally means that

58

evaporation from one side of the liquid plug is continuous. The vapour pressure in the gas will not saturate like in a closed system. One way to prolong the evaporation process is by the aid of diffusion (recall sec. 2.3.4). By designing the channel distance from the ventilation outlet to the meniscus of the plug considerably long and the cross section narrow, one is able to keep the liquid volume loss to a minimum.

In an actual microchip the gas may be air and the liquid may be a complex solution consisting of many different chemicals (e.g. water, DMSO, Sorbitol, etc.). This means that the bulk liquid may evaporate molecules from all these chemicals into the air, resulting in a mixture of gases. The situation may be modeled as a multicomponent system with partial pressures from all the contributing solvents, which will not be explained any further in this work. The reader may refer to textbooks such as Moran & Sharpiro (1998).

2.3.7   Dimensionless numbers

Special dimensionless numbers related to the physical behaviour of multiphase flow are introduced in Tab. 2.7. These numbers relate convection, diffusion, gravitation, inertia, surface tension, and viscosity to specific characteristic dimension.

Table 2.7: Dimensionless numbers.

Parameter	Definition	Qualitative ratio of effects	Importance
Reynolds number	$Re = \frac{\rho U L}{\mu}$	$\frac{\text{Inertia}}{\text{Viscosity}}$	Always
Capillary number	$Ca = \frac{\mu U}{\gamma}$	$\frac{\text{Viscosity}}{\text{Surface tension}}$	Capillary flow
Péclet number	$Pe = \frac{U L}{D}$	$\frac{\text{Convection}}{\text{Diffusion}}$	Mixing
Bond number	$Bo = \frac{\rho g L^2}{\gamma}$	$\frac{\text{Gravitation}}{\text{Surface tension}}$	Free-surface flow
Weber number	$We = \frac{\rho U^2 L}{\gamma}$	$\frac{\text{Inertia}}{\text{Surface tension}}$	Free-surface flow

Consider a typical microchannel of $L = 100$ μm, where a stream of water and a stream of aqueous solvent are flowing in parallel at a velocity of $U = 10^{-3}$ m/s.

Additional properties are $\rho = 10^3$ kg m^{-3}, $\mu = 10^{-3}$ kg m^{-1} s^{-1}, $\gamma = 0.073$ J m^{-2}, while the diffusion coefficient of the solvent is $D = 10^{-11}$ m^2 s^{-1} and the characteristic mixing length is 1 cm. The dimensionless parameters become $Re \sim 10^{-1}$, $We \sim 10^{-6}$, $Ca \sim 10^{-5}$, $Bo \sim 10^{-3}$, and $Pe \sim 10^4$. In words this means that the flow is laminar (Re), surface tension is dominating the interface (Ca), and that the liquids have traveled far downstream before completely mixed (Pe). The gravitational and inertial forces are usually negligible in microsystems, hence the low values of Bo and We.

2.4   Commercial software

The fluid dynamical problems and solutions described in chapters 6 and 7 in this thesis were addressed using the commercial simulation software ANSYS CFX (version 5.7 and version 10.0[7], ANSYS, Inc., Canonsburg, PA, USA.) in combination with theoretical[8] and experimental results. It is thus important to have an understanding of CFX, in order to achieve reasonable and reliable results in an investigation of physical phenomena related to micro scale flows. This section presents an overview of the software and models whereas actual simulation results are given in the above mentioned chapters.

CFX is a commercial multi-physics program package providing geometry, grid generation, solver, and visualization facilities all on a graphical user platform. The package includes the following applications:

- ANSYS DesignModeler: Geometry generation.

- CFX-Mesh: Grid generation.

- CFX-Pre: The solver set-up interface.

- CFX-Solver: The solver engine.

- CFX-Post: Results viewer (Post-processor).

The CFX-Solver includes several physical modules for, e.g., multiphase, turbulence, heat transfer, radiation, combustion, etc. In this work, only the flow and the homogenous multiphase (which also includes the VOF (Volume-of-Fluid) module) modules are used.

The two following sections present the flow and homogenous multiphase models, along with the solver settings used in this thesis.

---

[7]version 5.7 is used in the work of chapter 6, whilst chapter 7 includes version 10.0.
[8]Chapter 6 only.

2.4.1 The flow module

The flow module is the core element of the CFX-Solver and is generally used in most applications of the CFX package. It is coupled with all other modules in the solver and is able to simulate almost any kind of fluid within a defined geometry. Basically, it solves the continuity equation and the Navier-Stokes equations within the geometrical restrains with appropriate boundary conditions. CFX uses a unique hybrid finite-element/finite-volume approach to discretizise the equations. In the finite-volume method (FVM), the region of interest is divided into small sub-regions, called control volumes. The equations are integrated, discretized and solved iteratively for each control volume. By enforcing local conservation over each of the control volumes, the FVM satisfies strict global conservation. As a result, the solution fields are stored at the mesh nodes in each control volume throughout the domain. However, various terms in the equations require solutions or solution gradients (i.e. various source terms and surface fluxes) to be evaluated at integration points. CFX uses finite-element methodology (FEM) to describe the solution variation within each control volume, or more specifically, element. In contrast to the FVM where the governing equations are integrated over the control volumes, FEM makes the use of simple piecewise (e.g. linear or quadratic) functions defined on small elements to approximate the exact solution. A residual is defined to measure how far the approximate solution is from fulfilling the governing equations.

The technology of the CFX-Solver includes two key attributes that greatly enhance solution cost (defined as CPU effort, solution time or CPU requirements). One key element is inter-equation coupling. The non-linear equations that arise by applying the finite-volume method to all elements in the domain are linearized by coefficient iteration and assembled into a solution matrix. Segregated (non-coupled) solvers employ a solution strategy where the momentum equations are first solved, using a guessed pressure, and an equation for a pressure correction is obtained. Because of the "guess-and-correct" nature of the linear system, a large number of iterations are typically required in addition to the need for judiciously selecting relaxation parameters for the variables. CFX uses a coupled solver, which solves the hydrodynamic equations (for u, v, w and p) as a single system. This solution approach uses a fully implicit discretisation of the equations at any given time step. For steady state problems, the time-step behaves like an "acceleration parameter", to guide the approximate solutions in a physically based manner to a steady-state solution. This reduces the number of iterations required for convergence to a steady state, or to calculate the solution for each time step in a time dependent analysis.

Another key element in the CFX-Solver is the Algebraic Multigrid (AGM) (Raw, 1996) strategy used to solve the coupled linear set of equations. While the coupled

aspect of the solver deals with local effects, the multigrid strategy handles long distance or "long wavelength" effects. The AMG forms a system of discrete equations for a coarse mesh by summing the fine mesh equations. This results in virtual coarsening of the mesh spacing during the course of the iterations, and then re-refining the mesh to obtain an accurate solution. This technique significantly improves the convergence rates. Algebraic Multigrid is less expensive than other multigrid methods since discretisation of the non-linear equations is only performed once for the finest mesh. CFX uses a particular implementation of (AMG) called Additive Correction (Huchinson & Raithby, 1986) This approach is ideally suited to the CFX-Solver implementation, because it takes advantage of the fact that the discrete equations are representative of the balance of conserved quantities over a finite volume. The coarse mesh equations can be created by merging the original finite volumes to create larger ones as shown below. Fig. 2.19 shows the merged coarse finite volume meshes to be regular, but in general their shape becomes very irregular. The coarse mesh equations thus impose conservation requirements over a larger volume and in so doing reduce the error components at longer wavelengths.

Original mesh   **First coarse mesh**   **Next coarse mesh**
                                  (virtual)   **(virtual)**
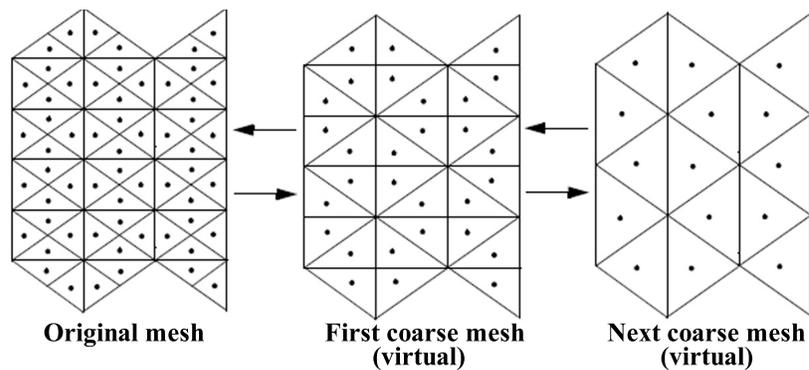
Figure 2.19: Sketch illustrating the principle of multigrid strategy of the CFX-Solver.

The advantages of such a coupled treatment over a non-coupled or segregated approach are several: robustness, efficiency, generality and simplicity. These advantages all combine to make the coupled solver an extremely powerful feature of any CFD code. The principal drawback is the high storage needed for all the coefficients.

Discretization scheme

By default, CFX uses a high resolution scheme to evaluate advection fluxes. This is a bounded, second-order upwind scheme based on that of Barth & Jesperson (1989). It ensures high accuracy (reducing to first order near discontinuities and

in the free stream where the solution has little variation) and good convergence while still producing physical results that are free of spurious spatial overshoots and undershoots in the solution variables. For transient flows, an implicit second-order accurate time differencing scheme is used.

There are possibilities in CFX-Pre to choose a specific numerical spatial difference schemes other than the above mentioned, but the default settings were applied in this work.

Solver settings

In CFX-Pre it is possible to tune on several numerical parameters influencing the solution convergence. Additionally several output options are available. The numerical parameters are:

- Maximum iterations: The number of iterations allowed. For transient flows, the maximum number of each coefficient loop.

- Convergence criterion: The minimum reduction in residual for each variable.

- Minimum residual: A minimum residual at which to stop the iteration procedure (if previous criterion is not applied).

Furthermore, the CFX-Solver allows the control of some advanced options, e.g. equation class settings (set a different timescale or advection scheme for each class of equations), pressure and velocity interpolation schemes, etc.

The convergence of a solution can be assessed by monitoring the residuals during the iteration process. In the present case the relevant parameters are pressure and velocity field. If necessary, parameters such as boundary conditions, time step, advection scheme and convergence criteria can then be adjusted without stopping the solver in order to accelerate convergence.

2.4.2 The homogeneous multiphase model

Multiphase model

Multiphase flow is a flow in which more than one fluid is present. Different phases of fluids are denoted using lowercase Greek letters α, β, γ, etc. The volume V_α occupied by phase α in a small volume V around a point of volume fraction r_α is given by:

$$V_\alpha = r_\alpha V, \tag{2.31}$$

where the total number of phases is N_P. The volume fraction of each phase is denoted r_α, where $\alpha = 1$ to N_P. It is important to distinguish between the

material density and the effective density of a fluid α. The material density, ρ_α, is the density of the fluid if it is the only phase present, i.e., the mass of α per unit volume of α. The effective density is then defined as:

$$\rho_e = r_\alpha \rho_\alpha. \tag{2.32}$$

This is the actual mass per unit volume of phase α, given that phase α only occupies a fraction of the volume, i.e., the mass of α per unit volume of the bulk fluid. The mixture density is given by:

$$\rho_m = \sum_{\alpha=1}^{N_P} r_\alpha \rho_\alpha. \tag{2.33}$$

The homogeneous[9] multiphase flow model is a limiting case of Eulerian-Eulerian multiphase flow where all fluids share the same velocity fields, as well as other relevant fields such as temperature, turbulence, etc. The pressure field is also shared[10] by all fluids. For a given transport process, the homogeneous model assumes that the transported quantities (with the exception of volume fraction) for that process are the same for all phases, i.e. the scalar variable ϕ,

$$\phi_\alpha = \phi \qquad (1 \leq \alpha \leq N_P) \tag{2.34}$$

Since transported quantities are shared in homogeneous multiphase flow, it is sufficient to solve for the shared fields using bulk transport equations rather than solving individual phasic transport equations. The transport equation for the scalar variable ϕ is governed by,

$$\frac{\partial}{\partial t}(\rho\phi) + \nabla \cdot (\rho \boldsymbol{V}\phi - \Gamma\nabla\phi) = S \tag{2.35}$$

where

$$\rho = \rho_m, \qquad \boldsymbol{V} = \frac{1}{\rho}\sum_{\alpha=1}^{N_P} r_\alpha \rho_\alpha \boldsymbol{V}_\alpha, \qquad \Gamma = \sum_{\alpha=1}^{N_P} r_\alpha \Gamma_\alpha. \tag{2.36}$$

The last term in the brackets on the left side of the Eq. 2.35 represents the diffusion contribution. Γ equals a material-specific quantity (e.g. diffusion coefficient), while S is a source term (e.g. momentum, energy).

---

[9]An inhomogeneous model, where separate velocity fields and other relevant fields exist for each fluid is also present in the code. This model is more appropriate if the phases are unstratified and the interface between them are not well defined.

[10]also for the inhomogeneous model.

Homogeneous fluiddynamic equations

The homogenous model for momentum transport assumes:

$$\boldsymbol{V}_\alpha = \boldsymbol{V} \qquad (1 \le \alpha \le N_P), \qquad (2.37)$$

and is given by:

$$\frac{\partial}{\partial t}(\rho \boldsymbol{V}) + (\rho \boldsymbol{V} \cdot \nabla)\boldsymbol{V} - \mu \nabla^2 \boldsymbol{V} = S_M - \nabla p \qquad (2.38)$$

where

$$\rho = \rho_m, \qquad \mu = \sum_{\alpha=1}^{N_P} r_\alpha \mu_\alpha. \qquad (2.39)$$

S_M is a momentum source term.

The continuity equation of the homogenous model is given as

$$\frac{\partial}{\partial t}(r_\alpha \rho_\alpha) + \nabla \cdot (r_\alpha \rho_\alpha \boldsymbol{V}) = S_{MS\alpha} + \sum_{\beta=1}^{N_P} \Gamma_{\alpha\beta}, \qquad (2.40)$$

where $S_{MS\alpha}$ is a user specified mass source and $\Gamma_{\alpha\beta}$ is the mass flow rate per unit volume from phase β to phase α. This term only occurs if interphase mass transfer takes place.

The VOF module

The VOF module is included in the homogenous multiphase model. It allows for the simulation of a mixture of two incompressible and immiscible fluids including surface tension effects. The basis of the VOF interface tracking method was presented in 1981 by Hirt & Nichols, but recently extended in 1997 by Rudman.

Assuming that there are two fluids involved in the model, a liquid and a gas, the essential features of the VOF interface tracking method are as follows: the distribution of the two fluids within the computational grid is accounted for using a single valued scalar variable F. F specifies the volume fraction of liquid in gas in a given computational grid cell. Hence if $F = 1$ a cell is full of liquid, if $F = 0$ a cell is full of gas, and in a cell containing an interface $0 < F < 1$.

The VOF module requires an initial condition describing the interface topology, which is used to compute volume of fluid fractions F in each computational cell in the grid. This requires a calculation of the volumes divided by the interface in each cell. The exact interface information is then neglected in favor of the scalar information lying in F. The advection of F is then governed by a transport equation,

$$\frac{\partial F}{\partial t} + \nabla \cdot (\boldsymbol{V}F) = 0, \tag{2.41}$$

which is solved together with the homogenous momentum and continuity equations (Eq. 2.38 and Eq. 2.40, respectively). Unlike some codes, CFX does not use reconstructing interface tracking (Rudman, 1997). Instead, CFX uses a compressive differencing scheme for the advection of volume fractions and a compressive transient discretisation scheme (if the problem is transient) to sharpen the interface, called "Volume Fraction Smoothing Type". There are three options available - none, Laplacian, and Volume-Weighted. Unfortunately, these algorithms are not publicly available[11]. The user has to try them out to find the most efficient one (This seems to be the case when working with CFD simulations in general; known or unknown algorithms). In Fig. 2.20 approximate F values are given in every cell together with the linear surface approximation.
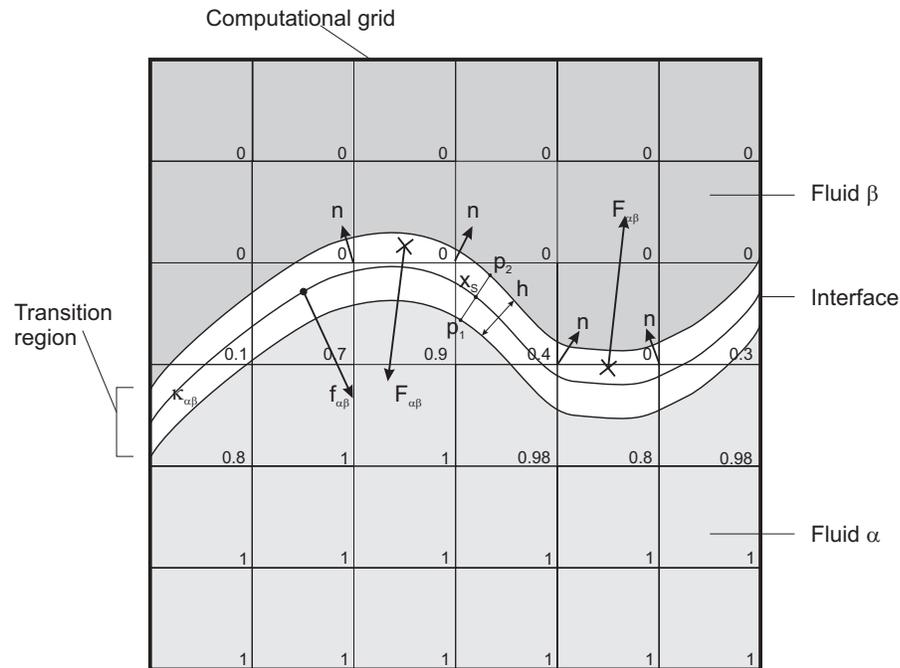
Figure 2.20: An example of a reconstruction of a free surface approximation of linear interfaces in each computational cell. Fluid α and fluid β have values 1 and 0, respectively. The transition region (uncoloured) has width h. This region includes the components of the Continuum Surface Force (CFS) surface physics model: surface force $\mathbf{f}_{\alpha\beta}$, CFS volume force $\mathbf{F}_{\alpha\beta}$, surface normal $\mathbf{n}$, and surface curvature $\kappa_{\alpha\beta}$.

---

[11]from correspondence with ANSYS Inc.

The surface tension model used in CFX is based on the Continuum Surface Force (CSF) model of Brackbill *et al.* (1992). This models the surface tension as a volume force concentrated at the interface, rather than a surface force. Consider the free surface interface shown in Fig. 2.20. The volume force $\boldsymbol{F}_{\alpha\beta}$ must satisfy

$$\lim_{h \to 0} \int_{\Delta V} \boldsymbol{F}_{\alpha\beta}(\boldsymbol{x})dV = \int_{\Delta A} \boldsymbol{f}_{\alpha\beta}(\boldsymbol{x}_S)dA, \tag{2.42}$$

where $\boldsymbol{x}_S$ is a point on the surface, ΔA is the portion of the surface lying within the small volume ΔV, and h is the transition region width (a length comparable to the resolution of the mesh spacing). The surface tension force is given as

$$\boldsymbol{f}_{\alpha\beta} = -\gamma_{\alpha\beta}\kappa_{\alpha\beta}\boldsymbol{n}_{\alpha\beta} + \nabla_S\gamma_{\alpha\beta}, \tag{2.43}$$

where $\gamma_{\alpha\beta}$ is the surface tension coefficient, $\boldsymbol{n}$ is the interface normal vector pointing from the primary fluid to the secondary fluid, ∇_S is the surface gradient, and $\kappa_{\alpha\beta}$ is the surface curvature defined by

$$\kappa_{\alpha\beta} = \nabla \cdot \boldsymbol{n}_{\alpha\beta}. \tag{2.44}$$

The two terms on the right side of Eq. 2.43 reflect the normal and the tangential components of the surface tension force, respectively. The normal component arises from the interface curvature and the tangential component from variations in the surface tension coefficient (i.e. the Marangoni effect).

The above formulation of the surface tension reduces to

$$\boldsymbol{F}_{\alpha\beta} = \boldsymbol{f}_{\alpha\beta}\delta_{\alpha\beta}, \tag{2.45}$$

where $\delta_{\alpha\beta}$ is a delta function called the interface delta function. It is zero away from the interface, therby ensuring that the surface tension force is active only near the interface. As the product $\kappa_{\alpha\beta}\ h \to 0$ the line integral of $\boldsymbol{F}_{\alpha\beta}(\boldsymbol{x}_S)$ should yield the Young-Laplace pressure jump $2H\gamma$.

Solid boundaries

When the interface between the two fluids intersects a wall, it is possible to account for wall adhesion by specifying the contact angle which the interface makes with the wall through the primary fluid. The interface normal vector used for the calculations of both curvature and the surface tension force must satisfy the wall contact angle.

Grid

CFX supports arbitrary mesh topologies, including hexahedral, tetrahedral, wedge, and pyramid elements. Unlike the segregated solvers, the coupled multigrid solver exhibits scalability. This means that solution time per node should be constant, i.e. solution cost on a fine grid having 10 times as many nodes as a coarse grid should be no higher than 10 times the coarse grid solution cost.

Grid generation was accomplished using the CFX-Mesh software. The generation and choice of calculating grid type are generally of crucial importance in CFD. According to the CFX manual grid aspect ratios as high as 100 can be handled, but generally such high values should be avoided.

The CFX-Mesh software generates tetrahedral unstructured meshes. The mesh generation process is fully automatic, however, there are possibilities for considerable control over how the mesh elements are distributed. Briefly, a background length scale dictates how the mesh should be refined. This parameter can be overridden locally on e.g. faces, particular regions, gaps, wherever necessary to appropriate mesh sizes by different mesh controls.

A powerful meshing option is a mechanism called *inflation*. This option allows for generating prism elements (and a small number of pyramids if required) near the walls. Inflation is used for resolving the mesh in the near wall regions to capture flow effects for viscous problems. As Fig. 2.21 shows, the method uses prisms to create a mesh that is finely resolved normal to the wall, but coarse parallel to it.
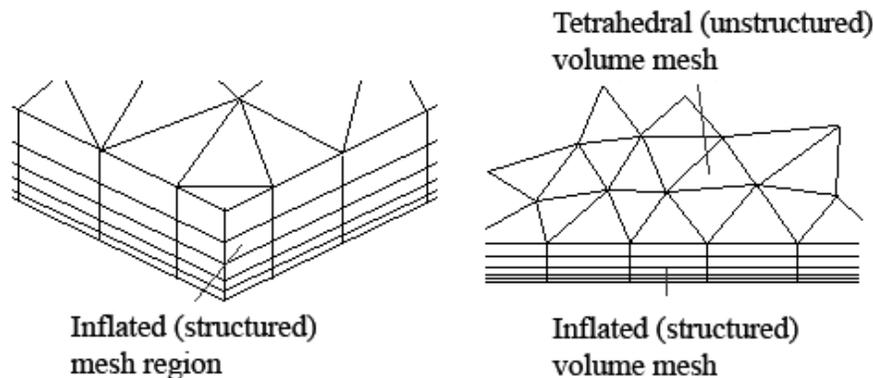
Figure 2.21: Figures showing the inflated mesh region and the transition between the inflation mesh and the tetrahedral mesh.

In general, the following points should be considered and noted as good meshing practice:

- The length scale should reflect the features of the flow to model. Typically

5% of the maximum model dimension. It is important to resolve geometric features that affect the flow with adequate mesh resolution.

- If the size of the geometric features varies significantly, then local control is required over the mesh. It is recommended at least 10 elements resolution across any features of interest.

- For the highest accuracy, one should generally seek a mesh-independent solution, which means that the results of the simulation do not change by reducing the mesh length scale.

- High aspect ratio elements are prone to round-off errors, due to the relative magnitude of the coefficients. Double precision helps high aspect ratio.

Homogeneous multiphase settings

By activating the "Free Surface" model in CFX-Pre, the VOF module is automatically enabled. It is also possible to tune on some numerical parameters influencing the solution convergence of a homogeneous multiphase simulation. The numerical parameters are:

- Interface compression level for interface sharpness, where 0=none, 1=standard compression, 2=enhanced compression. This helps convergence, but increases cost.

- In some cases, using the double precision solver executable can improve convergence. This also increases the cost.

References

ADAMSON, A. W. & GAST, A. P. 1997 *Physical Chemistry of Surfaces*, 6th edn. New York, NY: John Wiley & Sons, Inc.

BARTH, T. J. & JESPERSON, D. C. 1989 The design and application of upwind schemes on unstructured meshes. In *27th Aerospace and Science Meeting & Exhibit (Reno, 9-12 Jan. 1989) AIAA 89-0366*.

BECKER, H. & LOCASCIO, L. E. 2002 Polymer microfluidic devices. *Talanta* **56** (2), 267–287.

BJÅLIE, J. G., HAUG, E., SAND, O., SJAASTAD, Ø. V. & TOVERUD, K. 2003 *Menneskekroppen*, 5th edn. Oslo, Norway: Gyldendal Akademisk.

BRACKBILL, J. U., KOTHE, D. B. & ZEMACH, C. 1992 A continuum method for modeling surface-tension. *Journal of Computational Physics* **100** (2), 335–354.

COMPTON, J. 1991 Nucleic-acid sequence-based amplification. *Nature* **350** (6313), 91–92.

DEIMAN, B., VAN AARLE, P. & SILLEKENS, P. 2002 Characteristics and applications of nucleic acid sequence-based amplification (NASBA). *Molecular Biotechnology* **20** (2), 163–179.

DRAKE, T. & TAN, W. 2004 Molecular beacon DNA probes and their bioanalytical applications. *Applied Spectroscopy* **58** (9), 269A–280A.

FIORINI, G. S. & CHIU, D. T. 2005 Disposable microfluidic devices: fabrication, function, and application. *BioTechniques* **38** (3), 429–446.

GAD-EL-HAK, M. 1999 The fluid mechanics of microdevices - the freeman scholar lecture. *J. Fluids Eng.* **121**, 5–33.

GESCHKE, O., KLANK, H. & TELLEMANN, P., ed. 2004 *Microsystem Engineering of Lab-on-a-Chip Devices*, 1st edn. Weinheim, Germany: Wiley-VCH Verlag GmbH & Co. KGaA.

HIEMENZ, P. C. 1986 *Principles of colloid and surface chemistry*, 2nd edn. New York, NY: Marcel Dekker, Inc.

HIRT, C. W. & NICHOLS, B. D. 1981 Volume of fluid (VOF) method for the dynamics of free boundaries. *J.Comput.Phys.* **39**, 201–225.

HRNCIR, E. & ROSINA, J. 1997 Surface tension of blood. *Physiological Research* **46** (4), 319–321.

HUCHINSON, B. R. & RAITHBY, G. D. 1986 A multigrid method based on the additive correction strategy. *Numerical Heat Transfer* **9**, 511–537.

ISRAELACHVILI, J. 1991 *Intermolecular & Surface Forces*, 8th edn. London, UK: Academic Press.

JEON, S. I. & ANDRADE, J. D. 1991 Protein surface interactions in the presence of polyethylene oxide .2. effect of protein size. *Journal of Colloid and Interface Science* **142** (1), 159–166.

LEONE, G., VAN SCHIJNDEL, H., VAN GEMEN, B., KRAMER, F. R. & SCHOEN, C. D. 1998 Molecular beacon probes combined with amplification by NASBA enable homogeneous, real-time detection of RNA. *Nucleic Acids Research* **26** (9), 2150–2155.

LI, P. C. H. 2006 *Microfluidic Lab-on-a-Chip for Chemical and Biological Analysis and Discovery*, 1st edn. Boca Raton, FL: Taylor & Francis Group.

MADIGAN, M. T., MARTINKO, J. M. & PARKER, J. 1997 *Biology of Microorganisms*, 8th edn. Upper Saddle River, NJ: Prentice Hall International, Inc.

MARMUR, A. 1994 Thermodynamic aspects of contact angle hysteresis. *Advances in Colloid and Interface Science* **50**, 121–141.

MINTEER, S. D., ed. 2006 *Microfluidic Techniques: Reviews and Protocols*, 1st edn. Totowa, NJ: Humana Press Inc.

MORAN, M. M. & SHARPIRO, H. N. 1998 *Fundamentals of Engineering Thermodynamics*, 3rd edn. West Sussex, England: John Wiley & Sons Ltd.

NGUYEN, N. T. & WERELEY, S. T. 2002 *Fundamentals and Applications of Microfluidics*, 1st edn. Norwood, MA: Artech House, Inc.

PROBSTEIN, R. F. 1994 *Physicochemical Hydrodynamics*, 2nd edn. John Wiley & Sons, Inc.

RAW, M. J. 1996 Robustness of coupled algebraic multigrid for the Navier-Stokes equations. In *34th Aerospace and Sciences Meeting & Exhibit, January 15-18 1996, Reno, NV, AIAA 96-0297*.

RUDMAN, M. 1997 Volume-tracking methods for interfacial flow calculations. *International Journal for Numerical Methods in Fluids* **24** (7), 671–691.

SENTURIA, S. D. 2001 *Microsystem Design*, 1st edn. NY, USA: Springer Science+Business Media, Inc.

STRYER, L. 1995 *Biochemistry*, 4th edn. New York, NY: W. H. Freeman and Company, NY.

WHITE, F. M. 1991 *Viscous Fluid Flow*, 2nd edn. McGraw-Hill, Inc.

WHITE, F. M. 1994 *Fluid Mechanics*, 3rd edn. McGraw-Hill, Inc.

Chapter 3

Real-time nucleic acid sequence-based amplification in nanoliter volumes

Anja Gulliksen[1,2], Lars A. Solli[1,3], Frank Karlsen[1], Henrik Rogne[4], Eivind Hovig[5], Trine Norstrøm[1] & Reidun Sirevåg[2]

[1]NorChip AS, Industriveien 8, 3490 Klokkarstua, Norway
[2]Dept. of Biology, University of Oslo, Kristine Bonnevies hus, 0316 Oslo, Norway
[3]Dept. of Energy and Process Engineering, Norwegian University of Science and Technology, Kolbjørn Hejes vei 1B, 7491 Trondheim, Norway
[4]Dept. of Microsystems, SINTEF, Electronics and Cybernetics, Forskningsveien 1, 0314 Oslo, Norway
[5]Dept. of Tumor Biology, Norwegian Radium Hospital, Montebello, 0310 Oslo, Norway

Real-time nucleic acid sequence-based amplification (NASBA) is an isothermal method specifically designed for amplification of RNA. Fluorescent molecular beacon probes enable real-time monitoring of the amplification process. Successful identification, utilizing the real-time NASBA technology, was performed on a microchip with oligonucleotides at a concentration of 1.0 and 0.1 μM, in 10- and 50-nL reaction chambers, respectively. The microchip was developed in a silicon-glass structure. An instrument providing thermal control and an optical detection system was built for amplification readout. Experimental results demonstrate distinct amplification processes. Miniaturized real-time NASBA in microchips makes high-throughput diagnostics of bacteria, viruses, and cancer markers possible, at reduced cost and without contamination.

3.1 Introduction

Applying microsystem technology to the diversity of analytical problems has become an area of enormous interest, especially in connection with the development of microfluidic chips for clinical and forensic analysis (Verpoorte, 2002). One advantage of miniaturization is submicroliter consumption of reagents and sample. In addition, improved heat- and mass-transfer rates may give faster reaction kinetics. Miniaturization enables integration of multiple analytical steps in the same device, thus reducing the risk of carryover contamination. Hand-held lab-on-a-chip devices for point-of-care diagnostics are being developed.

A commonly used technique in molecular biology, clinical research, and evolutionary studies is enzymatic amplification of nucleic acids. The first thermostable amplification procedure published, polymerase chain reaction (PCR) (Saiki *et al.*, 1985), allowed amplification to a great number of copies of a specific region of a DNA chain in a very short time. Northrup *et al.* initially introduced PCR in silicon microstructures in 1993. Since then, numerous publications have appeared on simplification of PCR in microsystems using different approaches. Most of the reported PCR amplification methods use a combination of silicon and glass chips, with reaction chambers in the microliter range. Only a few reports describe PCR in nanoliter volumes or smaller. Experiments by Nagai *et al.* (2001) have demonstrated successful PCR amplification in reaction chambers for volumes down to 86 pL. Amplifications in reaction volumes of 160 and 280 nL have been reported by Hühmer & Landers (2000), Lagally *et al.* (2000*a*), Lagally *et al.* (2000*b*) and Lagally *et al.* (2001), respectively.

The main benefit of reducing sample volumes in PCR lies in enhanced thermal- and mass-transfer rates, which can significantly reduce the reaction time. Different approaches have been reported in order to obtain efficient heat transfer, such as conventional thermocyclers (Waters *et al.*, 1998), integrated polysilicon thin-film heaters (Northrup *et al.*, 1993), Peltier elements (Khandurina *et al.*, 2000), infrared radiation (Hühmer & Landers, 2000), waterbaths (Curcio & Roeraade, 2003), copper blocks (Kopp *et al.*, 1998), and indium-tin oxide thin-film heaters (Friedman & Meldrum, 1998).

The development of PCR in microsystems has led to the integration of complex procedures relevant for performing onchip PCR. Microchips where several analytical steps were incorporated onto a single device have been reported, including the following: cell lysis, amplification, real-time detection, and electrophoretic separation of PCR products (Nagai *et al.* (2001), Hühmer & Landers (2000), Lagally *et al.* (2001), Yuen *et al.* (2001) and Taylor *et al.* (2003)).

We have applied an alternative amplification method, termed nucleic acid sequence-based amplification (NASBA), to microchips. NASBA, initially intro-

duced by Compton in 1991, is a sensitive, transcription-based amplification system specifically designed for detecting RNA. The technology relies on the simultaneous activity of three enzymes (avian myeloblastosis virus reverse transcriptase, RNase H, T7 RNA polymerase) under isothermal conditions (41°C), producing more than 10^9 copies in 90 min. The amplification method is particularly well suited for analyses of various kinds of RNA: genomic RNA, mRNA, rRNA, viriods, and ssDNA. In some NASBA systems, dsDNA may also be amplified, albeit very inefficiently, and only in the absence of the corresponding RNA target (Deiman *et al.*, 2002). Based on this, the NASBA reaction has an application range including viral diagnostics, gene expression, and cell viability (Leone *et al.*, 1998).

NASBA is isothermal and consequently no thermocycling is needed. This is an advantage since it simplifies both the microchip design and the instrument specifications. In NASBA, the amplification is dependent on three enzymes, each catalyzing a specific reaction. Optimal stoichiometric ratio of the enzymes involved is necessary for the reaction to proceed. Thus, the amplification reaction itself is more complex in the case of NASBA than in the case of PCR, which only utilizes one enzyme. In NASBA, molecular beacon probes (Tyagi & Kramer (1996), Tyagi *et al.* (1998) and Tyagi *et al.* (2000)) hybridize to the target during the amplification, making possible real-time monitoring, which simplifies both the analytical procedure and the features of the microchip.

In this work, we report successful real-time amplification of oligonucleotides using NASBA technology in 10- and 50-nL silicon-glass reaction chambers. To our knowledge, this is the first time NASBA has been demonstrated in such a microsystem format.

3.2 Materials and methods

3.2.1 Microchip fabrication

The microchips were processed by SINTEF. Chambers and channels were etched in the silicon wafers with a $\langle 100 \rangle$ crystal orientation using reactive ion etching. A 700-Å oxide layer was grown, before the silicon wafers were bonded to 525-μm-thick Pyrex glass, forming channels and chambers. The channels have cross sections of 50×50 μm. The dimensions of the 10- and 50-nL reaction chambers were $450 \times 450 \times 50$ and $1000 \times 1000 \times 50$ μm, respectively. Conically shaped holes in the Pyrex wafer were made by powder blasting by Micronit. The diameters of these holes were 430 μm on the top surface and 150 μm on the bottom surface. To prevent adsorption of template and inhibition of the enzymes, the chips were coated with SigmaCote (Sigma Chemical Co., St. Louis, MO), according to the manufacturer's instructions. Figure 3.1 shows photographs of a 10-nL reaction

chamber (Fig. 3.1a), the whole microchip with dimensions of $5000 \times 20\,000$ μm (Fig. 3.1b), and an illustration of the cross-sectional area of the silicon-glass microchip (Fig. 3.1c). The 50-nL microchips had the same layout as the 10-nL microchips, but with larger reaction chambers. Altogether, less than 70 microchips were fabricated for both 10 and 50 nL.
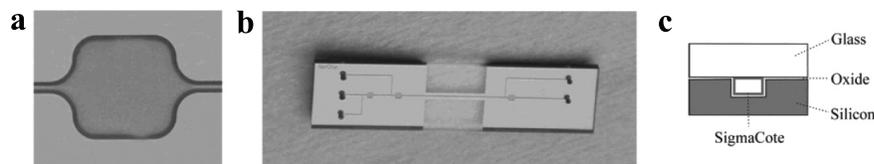
Figure 3.1: a Photograph of a 10-nL reaction chamber, $450 \times 450 \times 50$ μm. **b** The dimensions of the outer microchip are $5000 \times 20\,000$ μm. The two additional reaction chambers and channels were intended for loading of different reagents but were not used in these experiments. **c** Sketch of the cross-sectional area of the microchip.

3.2.2 Optical detection system and heat regulation

An optical system for measuring fluorescence was made for excitation at 494 nm and detection at 525 nm. The instrument consisted of a sample stage and a hinged optical table, located directly above the stage. The stage was mounted on an optical bench and had micrometer screws for x-, y-, and z-alignment of the sample.

Figure 3.2 shows a diagram of the optical geometry of the instrument. A high-intensity blue light-emitting diode (LED) (Marl International Ltd.) excited the fluorophores from above at a 23° angle to the reaction chamber. The excitation light was filtered and focused onto the reaction chamber. Emitted fluorescent light was collected by two lenses (Melles Griot, Santa Clara, CA) perpendicular to the reaction chamber and guided through a prism (Melles Griot), a dichroic beam splitter (Chroma Technology Corp, Brattleboro, VT), a filter (Chroma Technology Corp.), and finally into the photomultiplier tube detector (Hamamatsu). The data collection and preparation of the detected signal was processed on a laptop computer using LabView 5.11 software (National Instruments, Austin, TX). A schematic overview of the experimental setup is shown in Figure 3.3a. Figure 3.3b shows a photograph of the actual detection unit.

The intensity of the fluorescent light (3.5 pW) is extremely low compared to the excitation light (1 mW). Typically a filter transmits $\sim 1/10\,000$ of unwanted light, which is insufficient to separate the fluorescence from the LED light. Consequently, reflection or scattering of the excitation light into the direction of the optical path
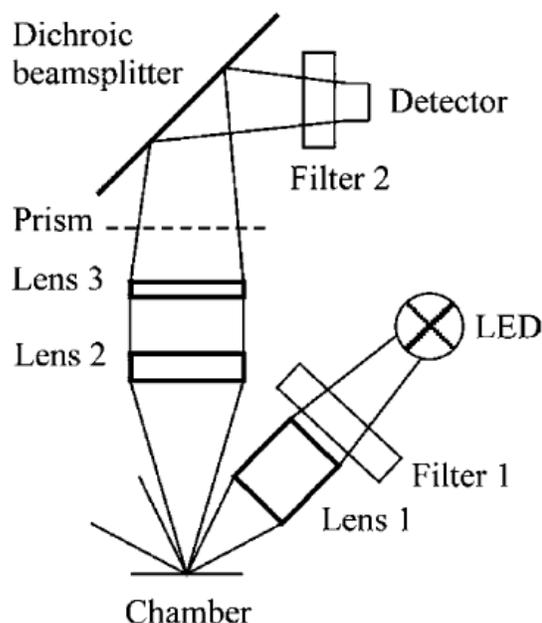
Figure 3.2: Sketch of the optical geometry. Blue light is emitted from the LED as shown in the diagram. Filter 1 is a bandwidth filter (465-500 nm). Lens 1 focuses the light onto the reaction chamber. The lens has a focal length of 10 mm and a diameter of 6 mm. Lens 2 (focal length, 17 mm; diameter, 14 mm) and lens 3 (focal length, 55 mm; diameter, 14 mm) collect and guide the fluorescent light from the fluorophores to a prism and dichroic beam splitter. The latter projects the light onto filter 2 (500-545 nm), which is mounted in front of the detector.

of the detector must be avoided. The 23° angle between the LED and the reaction chamber surface eliminates such reflections. To eliminate scattering, the surface in the reaction chamber was made optically smooth, which means a surface roughness less than 1/10 of the wavelength of the light employed. The roughness in the reaction chambers in the silicon-glass chips was measured with a WYKO white light interferometer (Veeco Instruments Inc., Woodbury, NY) and found to be less than 40 nm and thus within the limits of optical smoothness.

To control the temperature of the chip, an aluminum chip holder was mounted on top of a Peltier element (Marlow Industries Inc., Dallas, TX). A thermocouple was integrated in the aluminum block with a feedback circuit to the Peltier element. The temperature system was controlled externally on a laptop computer with incorporated digital PID controllers (National Instruments) for regulation. The temperature precision of the system was within 41.0 ± 0.1°C. A commercial Fluke temperature calibration apparatus (Fluke, Everett, WA) was used to calibrate the
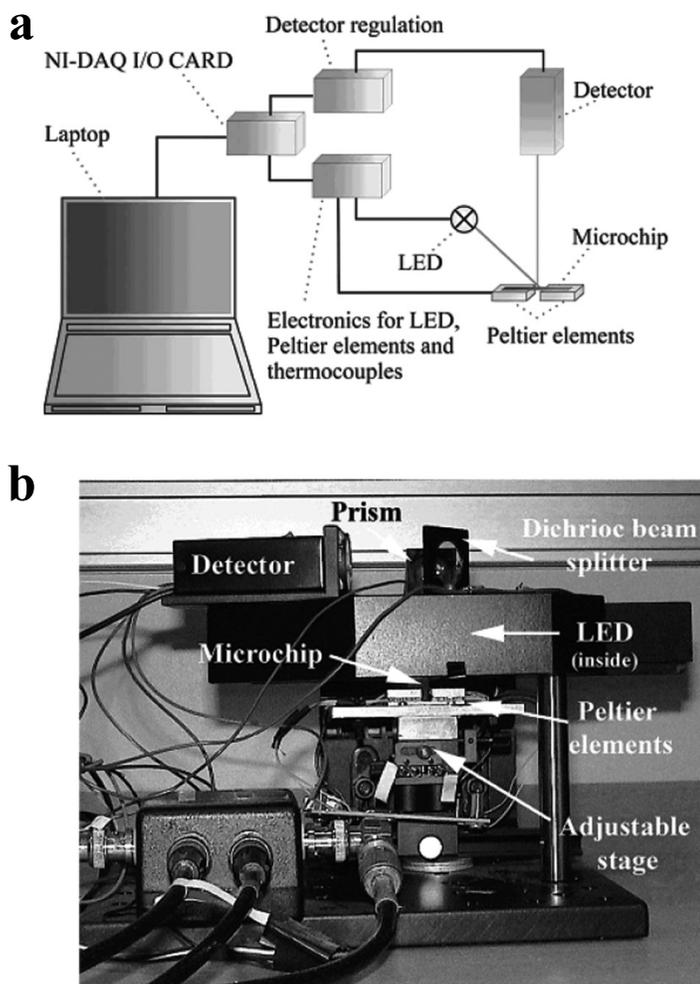
Figure 3.3: a Diagram of the experimental setup. **b** Photograph of the optical module.

system with thermocouples and a platinum resistance sensor. Measurements were performed both on the aluminum block and on top of a dummy chip without glass. The Fluke temperature calibration unit measured absolute temperatures to within $\pm 0.1°$C. The overall temperature accuracy of the system was $\pm 0.3°$C, after calibration.

A limited number of disposable microchips were fabricated. Commercially available glass capillaries (Drummond Scientific Co, Broomall, PA) were used for temperature calibration, sample alignment, and testing of the data collection system. For these purposes, solutions containing active fluorophores in addition to the NASBA reaction mixture were applied to the glass capillaries. The glass

capillaries had a capacity of 5 μL with an inside diameter and outside diameter of 447 and 940 μm, respectively. During measurements, only 2 mm of the capillary was illuminated; this corresponds to a detection volume of 300 nL.

Additionally, conventional 20-μL NASBA reactions were performed in polypropylene tubes. The amplification was performed in a Biotek FL600 reader (MWG Biotech AG). The experiments were carried out in order to compare the experimental results from the microchips and the glass capillaries with conventional methods. The Biotek FL600 reader had a temperature variance of 41 ± 1°C. Both the custom-made instrument with integrated thermal control and optical detection and the Biotek FL600 reader had an excitation wavelength at 494 nm and an emission wavelength at 525 nm.

3.2.3   Sample material

A positive control for human papillomavirus (HPV) 16, from the HPV Proofer kit (NorChip AS, Klokkarstua, Norway) was used as sample material. In addition, an artificial 118-bp single-stranded DNA (ssDNA) 5'-GATTAGACATTTCAGCATA–CGCATAATCGGCCGGCTTCGCCTAGGCATATCCTTTGCATGCTACTATA–TGGGACGATACGACCAAATGCCAGTCAGATAGCACAGTAGCAGCGATT–AA-3' (NorChip AS) was used to test NASBA in nanoliter volumes.

3.2.4   NASBA

The NASBA reaction was performed in microchips and glass capillaries with volumes of 10, 50, and 300 nL. For performance comparison, conventional amplification was carried out in 20-μL polypropylene tubes.

Primers and molecular beacon probes for the HPV 16 were provided with the HPV Proofer kit (NorChip AS). Primers and probes for the 118-bp ssDNA were not included in the original kit. The following sequences were used in the amplification process of the ssDNA: primer 1 (5'-AATTCTAATACGACTCACTATAGGGAG–AAGGGCTGCTACTGTGCTATCTGA-3'), primer 2 (5'-GACATTTCAGCATA–CGCATA-3'), and molecular beacon probe (5'-FAM-GCGGCATCCTTTGCATG–CTACTATA GCCGC-dabsyl-3') (NorChip AS).

The reagents were mixed according to the manufacturer's instructions. It should be pointed out that manual mixing of reagents may lead to some relative shifts in the negative and positive baseline signals presented in the plots due to concentration variations of reagents. Depending on the application and target of interest, the reactants were optimized. For HPV 16, the final concentration of the molecular beacon was 0.42 μM, whereas for the ssDNA the concentration was 0.21 μM. As a negative control, water was added to the reaction mixture instead of target DNA. In addition to the regular kit reagents, yeast tRNA (Sigma Chemical

Co.) was added to the reaction mixture to a final concentration of 4 μg/mL. To reduce the surface adsorption of enzymes and targets, tRNA was used as a dynamic coating. The surfaces of the silicon chips may inhibit the amplification reaction and were treated with surface agents to reduce nonspecific adsorption of the NASBA reagents. As previously described, both the silicon-glass chips and the glass capillaries were coated with SigmaCote to prevent adsorption.

Reagent solution (10 μL) from the kit and 5 μL of sample material (0.1 and 1.0 μM) were mixed and heated to 65°C for 5 min. The mixture was subsequently cooled to 41°C, after which the enzymes were added and the resulting solution was kept at 41°C for 5 min. A Hamilton glass syringe, with a disposable sequencing pipet tip attached to it, was used to apply the sample to a chip. The solution was drawn into the hydrophilic microchip by capillary forces. The inlet holes were subsequently covered with wax to avoid evaporation of the sample. The chip was incubated in the chip holder on top of the Peltier elements at 41°C. Approximately 10 min was needed to inject the reaction mixture into the reaction chambers and to align the microchip. The microchip was only used once due to a high risk of contamination if the microchips were to be used in subsequent experiment.

The same approach that was used for the microchips was utilized to coat, fill, and seal the disposable glass capillaries. The pipets were completely filled with reaction mixture and placed on the aluminum block on top of the Peltier elements underneath the optical detection system. The custom-built instrument detected only a 2-mm cross section of the glass capillary, corresponding to a reaction volume of 300 nL.

3.3   Results and discussion

The main objective of these experiments was to demonstrate the NASBA procedure in microchips with nanoliter reaction volumes. Due to the limited number of silicon-glass microchips, which passed the quality control, it was decided to test only one kind of sample in the 10- and 50-nL reaction chambers. Table 3.1 lists the experiments performed in microchips, glass capillaries, and polypropylene tubes. The results of the nanoliter-scale amplification reactions were compared to conventional NASBA performed in polypropylene tubes (20 μL).

The reactions presented in Figures 3.4–3.7 started after 10 min, due to the time consumed for addition of enzymes and injection of sample into the microchip and alignment in the instrument. Figures 3.4 and 3.5 demonstrate results for real-time NASBA performed in glass capillaries and in the conventional Biotek FL600 reader, using 0.1 μM ssDNA and 1 μM HPV 16 as sample material, respectively. The results using negative controls are presented in each case.

A comparison of the curves shown in Figures 3.4 and 3.5, for 300 and 20 μL,

Table 3.1: Overview of the figures presented and the experiments performed.

Figure	Reaction chamber	Chamber volume	Sample material
4	glass capillary	300 nL	ssDNA
	polypropylene tube	20 μL	ssDNA
5	glass capillary	300 nL	HPV 16
	polypropylene tube	20 μL	HPV 16
6	microchip	50 nL	ssDNA
	polypropylene tube	20 μL	ssDNA
7	microchip	10 nL	HPV 16
	polypropylene tube	20 μL	HPV 16
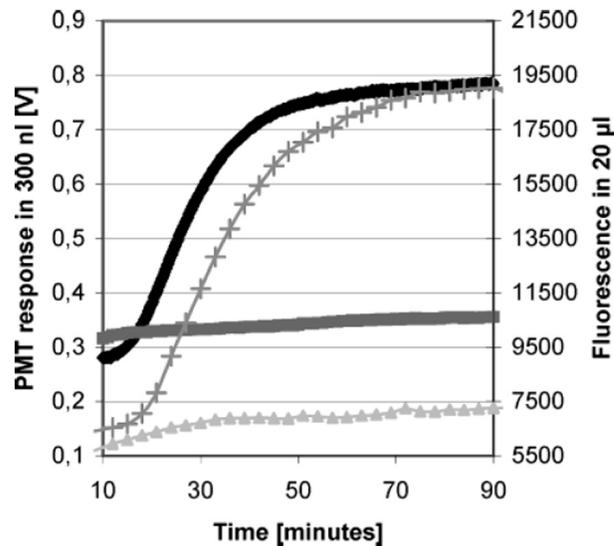
Figure 3.4: Real-time NASBA of ssDNA performed in glass capillaries and in conventional polypropylene tubes: ♦, 0.1 μM ssDNA in 300 nL; ■, negative control in 300 nL; +, 0.1 μM ssDNA in 20 μL; ▲, negative control in 20 μL.

displays a high degree of conformity in performance. The graphs demonstrate the characteristic shape of a real-time amplified reaction, and there is a clear difference between the amplification and the negative control. The exponential phase for detection starts at the same time for both 300- and 20-μL volumes. However, there is a significant difference in the signal level for the HPV 16 compared to that of the ssDNA caused by concentration variations of the molecular beacons. Using ssDNA as target, the signal levels obtained for both glass capillaries measured in

the custom-made instrument and in the conventional reader demonstrate a 3-fold increase from start to end point. The increase of the conventional amplification of HPV 16 is ∼7 times the base signal, whereas in the glass capillaries the increase is 5 times (Figure 3.5). This is expected, as noise will become more significant as the reaction volume decreases and will dominate at low signal levels.
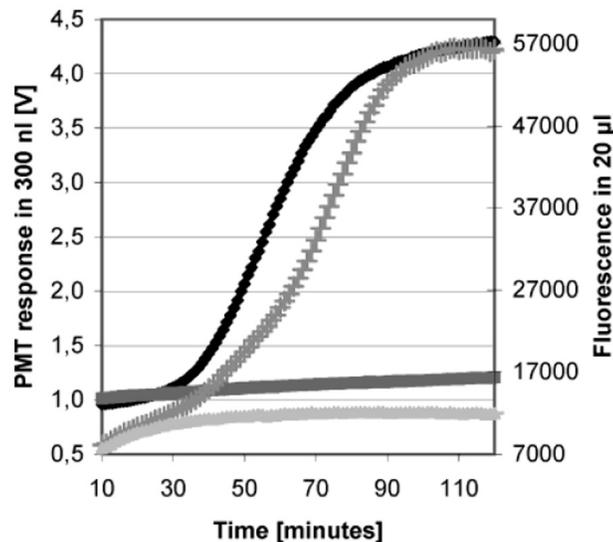
Figure 3.5: Real-time NASBA of HPV 16 oligonucleotides performed in glass capillaries and in conventional polypropylene tubes: ♦, 1.0 μM HPV 16 in 300 nL; ■, negative control in 300 nL; +, 1.0 μM HPV 16 in 20 μL; ▲, negative control in 20 μL.

Figure 3.6 shows results from experiments using ssDNA in silicon-glass microchips with 50-nL reaction chambers, and in 20-μL polypropylene tubes using the conventional reader. The ssDNA concentration was 0.1 μM. For illustration purposes, the negative control was adjusted by a factor of 0.45 in the figure. As shown in Figure 3.4, the conventional amplification signal increases 3 times from the starting level. In 50 nL, the signal increases by a factor of 2. The discrepancy between the negative control and the starting point of the amplified target was anticipated, as it was difficult to repeatedly place the microchip manually in exactly the same position every time. The error introduces a relative shift in the detector readout and does not affect the amplification process itself. The results show a distinct difference between the negative control and the amplification curve. The amplification curve displays the expected shape and time dependency.

Figure 3.7 shows the results of the amplification of HPV 16 performed in a silicon-glass microchip with a 10-nL reaction chamber and in the conventional
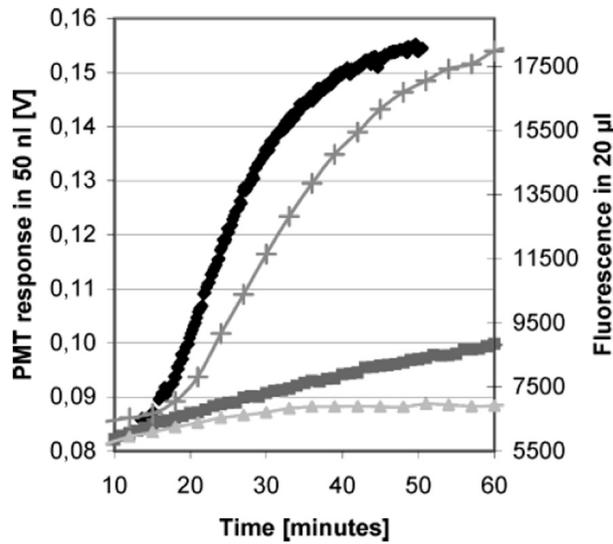
Figure 3.6: Real-time NASBA of ssDNA performed in a 50-nL reaction chamber and in conventional polypropylene tubes: ♦, 0.1 μM ssDNA in 50 nL; ■, negative control in 50 nL; +, 0.1 μM ssDNA in 20 μL; ▲, negative control in 20 μL.

polypropylene tubes. For the 10-nL reaction volume, the signal was amplified by a factor of 2 from 0.055 to 0.100 V. The fluorescence signal in the conventional reaction volume was increased 7 times and is the same as presented in Figure 3.5. The 10-nL amplification curve has a different progress further to the left in the chart compared to the conventional curve. Several factors can result in the observed shape of the curve. Such factors could be due to higher target concentration (Deiman *et al.*, 2002) and concentration variations, because the target of interest was acquired from different samples. In addition, the heat transfer in silicon is significantly faster than in glass or polypropylene and can result in reduced amplification times.

Another challenge related to microchip miniaturization is surface treatment. In microsystems, the surface-to-volume ratio is several orders of magnitude larger than in conventional systems. Preliminary experiments performed with no surface treatment of the silicon-glass structures gave negative results. Therefore, if the surface is not treated to prevent adsorption, the large surface area can disturb and even inhibit the whole process as in this case. Shoffner *et al.* (1996) emphasized the need of surface treatment to be able to perform PCR in silicon-glass structures. Enzymes are complex molecules consisting of hydrophilic, hydrophobic, and charged areas in a vital three-dimensional structure, and the surface properties of the reaction chamber can cause the enzymes to adsorb to the surface. The
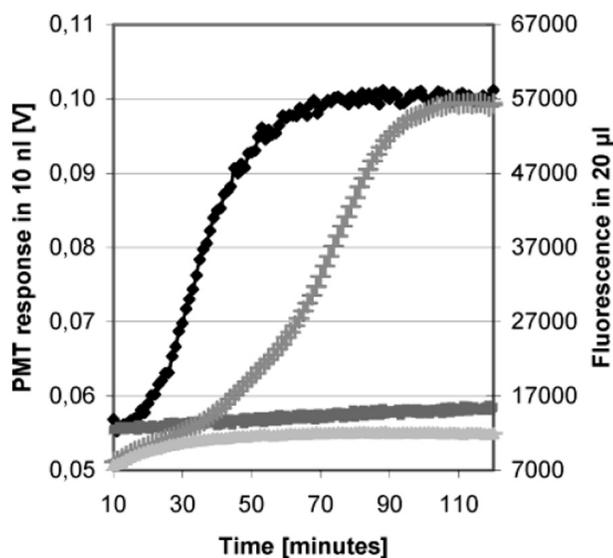
Figure 3.7: Real-time NASBA of HPV 16 oligonucleotides performed in a 10-nL reaction chamber and in conventional polypropylene tubes: ♦, 1.0 μM HPV 16 in 10 nL; ■, negative control in 10 nL; +, 1.0 μM HPV 16 in 20 μL; ▲, negative control in 20 μL.

major subprocesses constituting the overall protein adsorption are changes in the state of hydration, redistribution of charged groups, and rearrangements in the protein structure. It is therefore important to obtain a surface with hydrophilic properties similar to that of the enzyme exterior (Norde & Lyklema, 1992). The surface property in microsystems used for the NASBA reaction, which contains three enzymes, is therefore extremely important. Downscaling the reaction volume also effects the fluid dynamics of the system. The surface tension can be treated chemically to create either hydrophilic or hydrophobic behavior with specific liquids (Ratner, 1995).

3.4   Conclusions

The experimental results have shown it is possible to detect real-time NASBA amplification in 10-nL volumes by utilizing a custom-made microfabricated device and an optical detection system under process control. This is a reduction of the conventional 20-μL reaction volumes by a factor of 2000. Furthermore, real-time NASBA was performed on two different target sequences at the nanoliter level. The performance of the NASBA reaction for the silicon-glass microchip was in agreement with the conventional method. But to obtain amplification

in silicon-glass microchips, addition of small quantities of carrier molecules and surface treatment were required.

Miniaturization makes it possible to integrate processes such as amplification and detection within the same microchip. Integration of an additional function such as sample preparation will result in even shorter analysis time and in addition reduce the possibility for contamination. The results from these experiments will be applied in future work toward an automated μ-TAS system for clinical diagnosis.

Acknowledgements

References

COMPTON, J. 1991 Nucleic-acid sequence-based amplification. *Nature* **350** (6313), 91–92.

CURCIO, M. & ROERAADE, J. 2003 Continuous segmented-flow polymerase chain reaction for high-throughput miniaturized DNA amplification. *Analytical Chemistry* **75** (1), 1–7.

DEIMAN, B., VAN AARLE, P. & SILLEKENS, P. 2002 Characteristics and applications of nucleic acid sequence-based amplification (NASBA). *Molecular Biotechnology* **20** (2), 163–179.

FRIEDMAN, N. A. & MELDRUM, D. R. 1998 Capillary tube resistive thermal cycling. *Analytical Chemistry* **70** (14), 2997–3002.

HÜHMER, A. F. R. & LANDERS, J. P. 2000 Noncontact infrared-mediated thermocycling for effective polymerase chain reaction amplification of dna in nanoliter volumes. *Analytical Chemistry* **72** (21), 5507–5512.

KHANDURINA, J., MCKNIGHT, T. E., JACOBSON, S. C., WATERS, L. C., FOOTE, R. S. & RAMSEY, J. M. 2000 Integrated system for rapid PCR-based DNA analysis in microfluidic devices. *Analytical Chemistry* **72** (13), 2995–3000.

KOPP, M. U., LUECHINGER, M. B. & MANZ, A. 1998 Chemical amplification: Continous flow PCR on a chip. *Science* **280**, 1046–1048.

LAGALLY, E. T., EMRICH, C. A. & MATHIES, R. A. 2001 Fully integrated PCR-capillary electrophoresis microsystem for DNA analysis. *Lab on a Chip* **1** (2), 102–107.

LAGALLY, E. T., MEDINTZ, I. & MATHIES, R. A. 2000*a* Single-molecule DNA amplification DNA amplification and analysis in an integrated microfluidic device. *Analytical Chemistry* **73** (3), 565–570.

LAGALLY, E. T., SIMPSON, P. C. & MATHIES, R. A. 2000*b* Monolithic integrated microfluidic DNA amplification and capillary electrophoresis analysis system. *Sens. Actuators, B* **63** (3), 138–146.

LEONE, G., VAN SCHIJNDEL, H., VAN GEMEN, B., KRAMER, F. R. & SCHOEN, C. D. 1998 Molecular beacon probes combined with amplification by NASBA enable homogeneous, real-time detection of RNA. *Nucleic Acids Research* **26** (9), 2150–2155.

NAGAI, H., MURAKAMI, Y., MORITA, Y., YOKOYAMA, K. & TAMIYA, E. 2001 Development of a microchamber array for picoliter PCR. *Analytical Chemistry* **73** (5), 1043–1047.

NORDE, W. & LYKLEMA, J. 1992 Why proteins prefer interfaces. In *The Vroman Effect* (ed. C. Bamford), pp. 1–20. VSP.

NORTHRUP, M. A., CHING, M. T., WHITE, R. M. & WATSON, R. T. 1993 DNA amplification with a microfabricated reaction chamber. *Transducers '93 the 7th International Conference on Solid-State Sensors and Actuators* pp. 924–927.

RATNER, B. D. 1995 Surface modification of polymers - chemical, biological and surface analytical challenges. *Biosensors & Bioelectronics* **10**, 797–804.

SAIKI, R. K., SCHARF, S., FALOONA, F., MULLIS, K. B., HORN, G. T., ERLICH, H. A. & ARNHEIM, N. 1985 Enzymatic amplification of beta-globin genomic sequences and restriction site analysis for diagnosis of sickle cell anemia. *Science* **230**, 1350–1354.

SHOFFNER, M. A., CHENG, J., HVICHIA, G. E., KRICKA, L. J. & WILDING, P. 1996 Chip PCR .1. surface passivation of microfabricated silicon-glass chips for PCR. *Nucl.Acids Res.* **24** (2), 375–379.

TAYLOR, M. T., NGUYEN, P., CHING, J. & PETERSEN, K. E. 2003 Simulation of microfluidic pumping in a genomic DNA blood-processing cassette. *J. Micromech. Microeng.* **13**, 201–208.

TYAGI, S., BRATU, D. P. & KRAMER, F. R. 1998 Multicolor molecular beacons for allele discrimision. *Nature Biotechnology* **16**, 49–53.

TYAGI, S. & KRAMER, F. R. 1996 Molecular beacons: Probes that fluoresce upon hybridization. *Nature Biotechnology* **14**, 303–308.

TYAGI, S., MARRAS, S. A. E. & KRAMER, F. R. 2000 Wavelength-shifting molecular beacons. *Nature Biotechnology* **18** (11), 1191–1196.

VERPOORTE, E. 2002 Microfluidic chips for clinical and forensic analysis. *Electrophoresis* **23**, 677–712.

WATERS, L. C., JACOBSON, S. C., KROUTCHININA, N., KHANDURINA, J., FOOTE, R. S. & RAMSAY, G. 1998 Multiple sample PCR amplification and electrophoretic analysis on a microchip. *Analytical Chemistry* **70**, 5172–5176.

Yuen, P. K., Kricka, L. J., Fortina, P., Panaro, N. J., Sakazume, T. & Wilding, P. 2001 Microchip module for blood sample preparation and nucleic acid amplification reactions. *Genome Res.* **11**, 405–412.

Chapter 4

Parallel nanoliter detection of cancer markers using polymer microchips

Anja Gulliksen[1,2], Lars A. Solli[1,3], Klaus S. Drese[4], Olaf Sörensen[4], Frank Karlsen[1,5], Henrik Rogne[6], Eivind Hovig[7] & Reidun Sirevåg[2]

[1]NorChip AS, Industriveien 8, 3490 Klokkarstua, Norway
[2]Dept. of Biology, University of Oslo, Kristine Bonnevies hus, 0316 Oslo, Norway
[3]Dept. of Energy and Process Engineering, Norwegian University of Science and Technology, Kolbjørn Hejes vei 1B, 7491 Trondheim, Norway
[4]IMM, Fluidik und Simulation, 55129 Mainz, Germany
[5]Buskerud University College, Kongsgata 51, 3019 Drammen, Norway
[6]Dept. of Microsystems & Nanotechnology, SINTEF ICT, 0314 Oslo, Norway
[7]Dept. of Tumor Biology, Norwegian Radium Hospital, Montebello, 0310 Oslo, Norway

A general multipurpose microchip technology platform for point-of-care diagnostics has been developed. Real-time nucleic acid sequence-based amplification (NASBA) for detection of artificial human papilloma virus (HPV) 16 sequences and SiHa cell line samples was successfully performed in cyclic olefin copolymer (COC) microchips, incorporating supply channels and parallel reaction channels. Samples were distributed into 10 parallel reaction channels, and signals were simultaneously detected in 80 nl volumes. With a custom-made optical detection unit, the system reached a sensitivity limit of 10^{-6} μM for artificial HPV 16 sequences, and 20 cells μl^{-1} for the SiHa cell line. This is comparable to the detection limit of conventional readers, and clinical testing of biological samples in polymer microchips using NASBA is therefore possible.

4.1   Introduction

Several studies have demonstrated that the presence of the human papilloma virus (HPV) is a prerequisite for the development of cervical cancer, the second most common cancer in women (Walboomers *et al.* (1999) and Muñoz *et al.* (2003)). Screening of cervical cancer is mainly done by cytological testing. However, this method has both poor reproducibility and specificity, as well as limited sensitivity (Jenkins, 2001). Therefore, new diagnostic methods have been developed. The present on-line technology identifies high-risk HPV mRNA transcripts employing real-time nucleic acid sequence-based amplification (NASBA) (Compton (1991), Leone *et al.* (1998), Kraus *et al.* (2004) and Cuschieri *et al.* (2004)). Briefly, NASBA is an isothermal (41°C) method specifically designed for amplification of any single-stranded RNA and DNA sequence, by using three different enzymes simultaneously. The use of a specific and sensitive technology, such as NASBA, for detection of highrisk HPV types, makes it possible to meet the increasing demands for diagnostic precision and prognostic information, and to prevent incorrect diagnosis based on subjective decisions.

We present experimental evidence of real-time NASBA detection in cyclic olefin copolymer (COC) microchips, with 80 nl detection volumes. The sample is automatically distributed into 10 parallel reaction channels for simultaneous detection, making it possible to specifically amplify and detect several different targets with high sensitivity on just one sample. The work presented here is part of a project towards a fully automated and disposable diagnostic microsystem with integrated sample preparation and detection modules for virus and bacteria identification. Shorter handling time, combined with reduced reagent and sample consumption, will be benefits of this system compared to conventional methods (Fig. 4.1).

4.2   Materials and methods

4.2.1   Microchip fabrication

Microchips, incorporating supply channels, reaction channels and microfluidic actuation systems, were injection molded in COC polymer (Elias, 1997). A photograph of the microchip is shown in Fig. 4.2a. An actuation system was implemented on the microchip for liquid plug movement. However, the actuation mechanism is not described here, as it was not applied to these experiments. A description of the design and actuation functions of the chips is presented elsewhere (Drese *et al.*, 2003).

The microchips were oxygen plasma activated prior to coating with 5% (w/v)
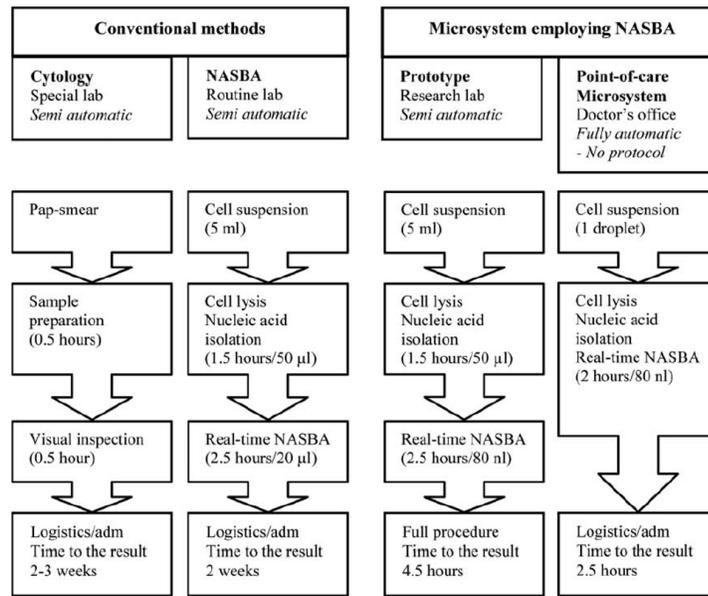
Figure 4.1: Comparison of conventional methods and a point-of-care microsystem for detection of cervical cancer. The false negative results for cytology is 69% for the first time tests. Employing NASBA, the false negative result is reduced to 23%. The time scale is approximate, since the analysis can be performed using different methods and instruments.
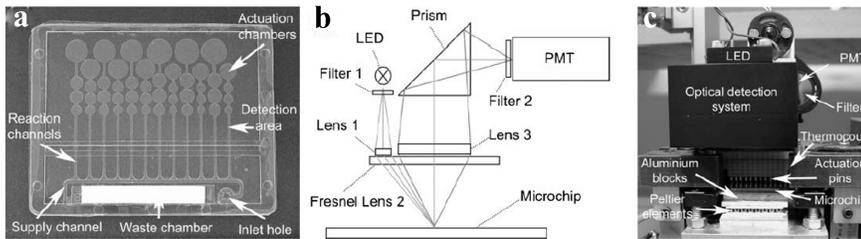
Figure 4.2: **a** A photograph of the COC microchip with dimensions of 50 × 40 mm. **b** Sketch of the optical geometry. **c** Photograph of the major components in the instrument.

polyethylene glycol (PEG) in methanol (Sigma Chemical Co, St. Louis, MO). A cotton linter filter (Schleicher & Schuell BioScience GmbH, Relliehausen, Germany) was placed in the waste chamber, and the chips were sealed by welding a 75 mm COC membrane to the substrate. To block out background fluorescence from the thermal pads in the instrument, gold (25 nm) was sputtered on the back of the chip.

4.2.2 Optical detection system

The optical detection system was redesigned from an earlier prototype (Gulliksen *et al.*, 2004), to increase light intensity and reduce component costs (Fig. 4.2b). Light emitting diodes (LED) (Lumileds, San Jose, CA), with 130 mW centred at 470 nm, excited the fluorophores from above at an angle of 26° to the plane of the chip surface. Hence, the excitation light is reflected away from the light path of the detection unit. Scattered excitation light entering the detection unit was reduced by a bandpass filter (Chroma Technologies Corp, Brattleboro, VT), 465 nm–500 nm, and collimated through a lens (Melles Griot, Santa Clara, CA), Ø12.5 mm/f30 mm. An off-axis fresnel lens, Ø50 mm/f25 mm, focused the collimated light onto the reaction chambers. Fluorophores, excited at 494 nm and emitting at 525 nm, were activated and the light was collected in the center of the fresnel lens, passed through a lens, Ø25 mm/f100 mm, a prism (Melles Griot), a bandwidth filter, 500 nm–545 nm, and an aperture, before being detected by a photomultiplier-tube (PMT) (Hamamatsu, Shizuoka, Japan). A 2×2 mm^2 area of the reaction channel was illuminated by the LED, corresponding to a detection volume of 80 nl ($400 \times 2000 \times 100 \ \mu$m^3).

Sequential measurements of the reaction chambers were performed by automatically moving the chip underneath the optical unit. Each channel was measured for 1 s on each scanning cycle, using a digital lock-in system operating at 1 kHz. A complete chip cycle took 90 s. Data were collected and processed using MATLAB (The MathWorks Inc., Natick, MA). Fig. 4.2c shows a photograph of the instrument set-up.

4.2.3 Instruments

Peltier elements (Marlow Industries Inc., Dallas, TX) with aluminum blocks mounted on top formed the chip holder. A thermal pad was placed on the blocks for thermal contact to the chip. A thermocouple was integrated into the chip holder, with feedback to the Peltier elements. Temperature regulation was controlled externally by the use of MATLAB. The system was calibrated with a commercial temperature calibration instrument (Fluke, Everett, WA) and platinum resistance sensors, both with an accuracy of ± 0.1°C. Temperature calibrations were performed both on the aluminum block, and on top of a dummy microchip, without a membrane. The overall temperature accuracy of the system was within ± 1°C.

The instrument was equipped with a movable chip holder for alignment of the polymer microchip, automatic actuation and optical positioning. The servomotors (Omron Electronics, Kyoto, Japan) were regulated by a physical signaling sublayer (PLS) (Saia-Burgess Electronics AG, Murten, Switzerland), programmed with PG

5 (Saia-Burgess Electronics AG). All communications were run through a serial line (RS232) and controlled by MATLAB.

Results from the two outermost channels on the microchip were excluded in this work, because of a design fault in the instrument.

For comparison, sample solutions were also tested using microplates in a conventional microplate reader, Lambda FL600 (Bio-Tek Instruments, Winooski, VT). The total detection volume of the Lambda FL600 was 20 μl.

4.2.4 Sample material

The SiHa cell line, with 1-2 copies of integrated HPV 16 DNA per cell, was used as a model system (Syrjanen *et al.* (1988), Mincheva *et al.* (1987) and Heiles *et al.* (1988)). The cells were obtained from the American Type Culture Collection (ATCC, Manassas, VA) and maintained in Dulbecco's modified Eagles medium (DMEM), supplemented with 10% fetal bovine serum (FBS), 2 mM L-glutamine and 25 μg ml^{-1} gentamycin. The cells were incubated at 37°C in a 5% CO$_2$ atmosphere, trypsinated, counted in a Bürker chamber, and lysed in lysis buffer (bioMérieux, Boxtel, the Netherlands), before the nucleic acids were isolated and extracted using a NucliSens Extractor (bioMérieux) (Boom *et al.*, 1990).

In addition, artificial HPV 16 sequences, from the PreTect$^®$ HPV-Proofer kit (NorChip AS, Klokkarstua, Norway) were used as targets in the reaction. To define the lower detection limit of the system, dilution series were tested. Serial dilutions ranging from 10^{-10} μM to 10^{-1} μM were tested using the artificial HPV 16 sequence, whereas the SiHa cell line was tested over a range from 2×10^{-2} cells μl^{-1} to 2×10^3 cells μl^{-1}. SiHa cell line samples (250 cells μl^{-1}) have been previously used as positive controls for detection of HPV 16 in biopsies from cervical cones (Kraus *et al.* (2004) and Kraus (2004)) in conventional microplates.

4.2.5 NASBA procedure

All reagents required to perform the NASBA amplification and the HPV detection were supplied as part of the PreTect$^®$ HPV-Proofer kit. The final concentration of the reaction mixture: 40 mM Tris-HCl (pH 8.5), 70 mM KCl, 12 mM MgCl$_2$, 5 mM DTT, 1 mM dNTP, 2 mM ATP, 2 mM CTP, 2 mM UTP, 1.5 mM GTP, 0.5 mM ITP, 0.2 μM of each primer, 0.4 μM molecular beacon probe (FAM/Dabsyl), 375 mM sorbitol, 0.119 g l^{-1} BSA, 15% (v/v) DMSO, 6.4 U AMV RT, 32 U T7 RNA polymerase and 0.08 U RNase H.

The reagent mixture except for the enzymes (26 μl) and sample material (13 μl) were mixed manually and heated on a conventional block heater at 65°C for 2 min. The mixture was subsequently incubated at 41°C for 2 min, after which the enzymes (13 μl) were added. This mixture was then immediately applied to the

microchip and distributed into 10 parallel reaction channels. To ensure that all individual reaction channels were filled, one actuation chamber on each channel was punctured before the addition of the mixture to the microchip. This caused the reaction channels to be filled due to capillary forces. Excess reaction mixture was drawn into the waste chamber and absorbed by the filter, completely separating the fluids in individual reaction channels. Chip movement, process control and measurements were handled by the instrument.

For comparison, the ten-fold serial dilutions of the artificial HPV 16 sequence and of the SiHa cell line were tested, both in the microchip and in the conventional system. Reaction mixtures were prepared in the same way for both systems. The reaction volume for the conventional system was 20 μl.

For negative controls, water for molecular biology (DNase or RNase not detected, Sigma Chemical Co.) was added instead of sample material. All experiments were run for 2.5 h at 41°C.

4.2.6   Calculations

Experimental results were processed with a dedicated NASBA regression calculation program, PreTect Data Analyzer (NorChip AS), based on polynomial regression algorithms. The final fluorescence level was divided with the initial fluorescence level and all reactions with a ratio larger than 1.7 were considered positive. Time-to-positivity (TTP) (Niesters (2001) and deBaar *et al.* (2001)) was chosen as the point of onset for exponential increase. The average slopes were calculated from the data between 10 and 80% increase in initial fluorescence level. The detection limit of the microchips was defined as the lowest concentration tested where all 10 reaction channels were positive.

4.3   Results and discussion

Identification of the HPV 16 sequence and the SiHa cell line utilizing real-time NASBA was successfully performed in polymer microchips with a detection volume of 80 nl. Fig. 4.3 shows the result obtained from one microchip experiment using a SiHa cell line and a HPV 16 sequence. The graphs are clearly positive, and reveal the same sigmoid curvature as when samples were tested using regular 20 μl volumes and conventional readers (Leone *et al.* (1998), Gulliksen *et al.* (2004) and deMello (2001)).

To characterize the amplification reactions, several different parameters were evaluated: the fluorescence ratio, time-to-positivity (TTP), the average slope of the linear part of the curve, the number of positive amplifications, the number of polymer microchips and microplate reactions tested. The values shown in
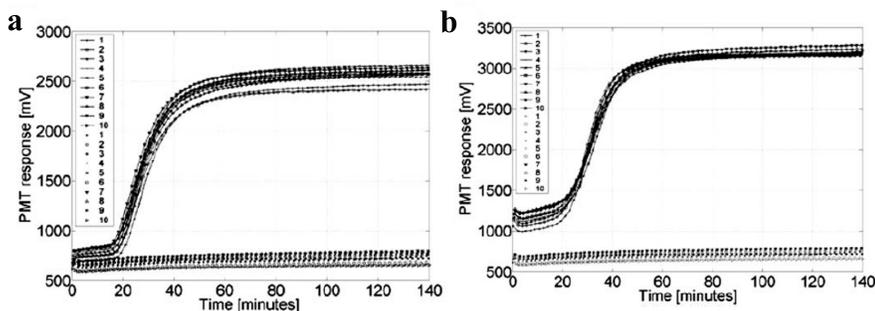
Figure 4.3: A **a** SiHa cell line sample (2000 cells μl^{-1}) and a **b** HPV 16 sequence sample (0.1 μM) tested on a microchip. Solid lines characterize positive amplification reactions while no lines represent negative controls. The key numbers indicate the reaction channels on the microchip from left to right.

Table 4.1 represent the average values and the standard deviations of all the positive samples tested within the different dilution series. In comparison, the standard deviations of: the fluorescent ratio, the TTP and the average slope for an individual microchip ranged from (0.1-0.5), (0.0-14.5) and (1.2-19.6), respectively. For most experiments, the standard deviations, between parallel reaction channels on one microchip, are in the lower part of the range.

A comparison of the NASBA results from the HPV 16 sequence and from the SiHa cell line, shows that all parameters display the same trend for microsystems as for conventional methods, except for the ratio between the final and initial fluorescence levels. This ratio is nearly constant for the microchip experiments, but decreases with sample concentration for the conventional experiments. The fluorescense level is determined by the concentration of molecular beacons in the reaction mixture. Theoretically, if the amplification reaches full reactant consumption, the final fluorescense level should be independent of sample concentration, but reached at different times. The overall lower ratio obtained in the microchips could be explained by the enlarged background noise, caused by autofluorescent COC and light scattering from imperfect polymer surfaces. The auto-fluorescence of the microchips was measured to $\sim$300 mV. Adsorption of reagents to the chamber wall will also contribute to background noise.

The results for the microchips correlate well with the conventional methods (Table 4.1). When concentrations are reduced, TTP increases, and the average slope decreases, because reagents need more time to find and interact with the targets. Small amounts of target give less amplified material at the beginning of the reaction, and hence the TTP increases. However, very high sample concentrations may slow down the reactions, because of enzymatic inhibition.

Table 4.1: NASBA performed on microchips and conventional microplates. The detection volumes were 80 nl and 20 μl, respectively. Serial dilutions of an artificial HPV 16 sequence and a SiHa cell line were tested for both systems. The table shows the average and standard deviations of all values measured in all experiments. A line represents no positive reaction detected.

Concentration	Ratio		TTP/min		Average slope: Microchips /mV min^{-1}; Conv./Fluorescence units min^{-1}		No. of positive reactions/Total no. of reactions	
	80 nl Microchips	20 μl Conv.	80 nl Microchips	20 μl Conv.	80 nl Microchip	20 μl Conv.	80 nl Microchip	20 μl Conv.
HPV 16 sequence /μM								
10^{-1}	2.8 ± 0.3	6.5 ± 0.2	13.9 ± 4.6	14.0 ± 0.8	45.6 ± 10.4	111.2 ± 19.3	40 / 40	6 / 6
10^{-2}	3.1 ± 0.4	6.7 ± 0.3	14.7 ± 4.0	11.8 ± 1.5	42.5 ± 9.5	96.3 ± 28.3	40 / 40	6 / 6
10^{-3}	2.8 ± 0.4	6.5 ± 0.3	9.0 ± 2.1	15.3 ± 1.8	46.0 ± 17.7	113.1 ± 33.6	30 / 30	6 / 6
10^{-4}	2.8 ± 0.3	5.2 ± 1.1	22.2 ± 4.5	23.8 ± 4.7	35.1 ± 17.9	94.4 ± 58.9	30 / 30	6 / 6
10^{-5}	2.6 ± 0.4	4.8 ± 1.2	22.6 ± 7.4	25.1 ± 3.7	29.9 ± 13.7	84.1 ± 38.3	30 / 30	12 / 12
10^{-6}	2.5 ± 0.5	3.8 ± 0.8	25.3 ± 3.6	26.3 ± 5.5	19.6 ± 9.2	42.8 ± 11.4	30 / 30	12 / 12
10^{-7}	2.1 ± 0.3	1.8 ± 0.1	37.1 ± 12.8	33.8 ± 7.4	17.3 ± 11.8	15.7 ± 1.5	33 / 70	2 / 12
10^{-8}	1.9 ± 0.3	—	43.8 ± 7.1	—	9.9 ± 3.6	—	6 / 60	0 / 12
10^{-9}	2.2 ± 0.9	—	81.0 ± 38.2	—	15.0 ± 6.3	—	2 / 60	0 / 12
10^{-10}	—	—	—	—	—	—	0 / 50	0 / 12
SiHa cell line/cells μl^{-1}								
2×10^{3}	2.9 ± 0.3	4.9 ± 0.6	16.9 ± 2.8	29.3 ± 1.3	42.6 ± 6.2	80.1 ± 6.8	40 / 40	6 / 6
2×10^{2}	2.8 ± 0.4	3.8 ± 1.2	18.9 ± 3.4	29.3 ± 4.0	40.6 ± 14.5	52.5 ± 24.8	40 / 40	6 / 6
2×10^{1}	2.9 ± 0.3	3.7 ± 1.2	30.7 ± 9.3	33.3 ± 7.9	37.5 ± 11.1	44.0 ± 16.8	39 / 40	5 / 6
2×10^{0}	2.8 ± 0.5	3.0 ± 0.4	38.0 ± 26.1	39.8 ± 1.1	35.1 ± 15.5	28.0 ± 7.2	60 / 70	2 / 6
2×10^{-1}	2.8 ± 0.5	—	70.1 ± 39.1	—	$39.3 \ 15.0$	—	4 / 50	0 / 6
2×10^{-2}	—	—	—	—	—	—	0 / 30	0 / 6

96

The custom-made optical detection system was found to have a detection limit of 10^{-6} μM for the artificial HPV 16 sequence, and 20 cells μl^{-1} for the SiHa cell line material. These values are the same as for the conventional Lambda FL600 reader (Table 4.1). It was possible to detect even lower concentrations in both systems, but the results were inconsistent, most likely due to stochastic sampling effects. The detection limit of the NASBA reaction is dependent on the target of interest, the quality of the RNA samples, and influenced by the design of the primers and the molecular beacon probe. Negative control experiments were run to check for contamination. Because the microchips were only used once, false positive results are only possible if the premixed reaction mixture is contaminated. False negative results could theoretically only arise from contamination with inhibiting agents during microchip fabrication.

The experimental results, based on experiments from 140 microchips $\times$ 10 individual reaction channels, including negative controls, are summarized in Table 4.1. Several factors influence the experimental results and are reflected in the calculated standard deviations. The results show that when the sample concentration of the input target decreases, the standard deviation increases. This could be caused by nonspecific surface binding of the target or pipetting skills. Particularly, nonspecific surface binding is more pronounced for the microchips than for regular microplates, because of a larger surface-to-volume ratio. For the present microchips, this is of great importance, because only three of the four walls forming the reaction chambers were coated with PEG. Experiments with uncoated microchips show complete inhibition of the reaction (data not shown). The PEG coating was in some cases damaged when the membrane was welded to the microchip, at treatment which may change the surface structure and lead to increased nonspecific binding and scattering of the excitation light. Also, BSA acts as a dynamic coating, reducing nonspecific binding of reagents to the channel walls. Volume variations in the pipetting affects the standard deviations for both microchips and microplates. Thus, reagents for individual microchips were mixed separately for each experiment, while for the conventional reactions only two reaction solution were mixed to perform all the experiments. Hence, the exact time for addition of enzymes and insertion of the microchip into the instrument varied between experiments. Also, stochastic sampling variation at lower molecular concentrations may affect the standard deviation.

The microchips used in these experiments had a large dead volume due to the design of the channel network. However, a reduction of dead volume may easily be obtained with a revised design.

4.4   Conclusions

Detection of cancer markers using real-time NASBA has been successfully demonstrated. To our knowledge, these are the first results showing detection of mRNA using real-time NASBA within such a microsystem. The detection limits are comparable to those obtained for experiments performed in conventional routine-based laboratory systems, demonstrating that the microchip and its detection system has a potential for diagnostic use in a point-of-care setting.

Future microchips could contain more reaction channels, and be combined with multiplexing of several different targets in each of the channels. Simultaneous detection of different targets is possible to identify with multi-parallel reaction channels having integrated different reagents in the channels. The benefits of the present system are reduced reagent consumption, combined with multi-parallel target testing, using only one sample. Hence, less sample material is required, since in many cases the amount of sample material is limited. Finally, an integration of this microchip, with an integrated sample preparation microchip, would constitute a fully automatic, laboratory independent diagnostic system, resulting in an overall time and cost reduction of the whole analysis.

Acknowledgements

References

Boom, R., Sol, C. J. A., Salimans, M. M. M., Jansen, C. L., Wertheimvandillen, P. M. E. & Vandernoordaa, J. 1990 Rapid and simple method for purification of nucleic-acids. *Journal of Clinical Microbiology* **28** (3), 495–503.

Compton, J. 1991 Nucleic-acid sequence-based amplification. *Nature* **350** (6313), 91–92.

Cuschieri, K. S., Whitley, M. J. & Cubie, H. A. 2004 Human papillomavirus type specific DNA and RNA persistence - Implications for cervical disease progression and monitoring. *Journal of Medical Virology* **73** (1), 65–70.

deBaar, M. P., vanDooren, M. W., deRooij, E., Bakker, M., vanGemen, B., Goudsmit, J. & deRonde, A. 2001 Single rapid real-time monitored isothermal RNA amplification assay for quantification of human immunodeficiency virus type 1 isolates from groups M, N, and O. *Journal of Clinical Microbiology* **39** (4), 1378–1384.

deMello, A. J. 2001 DNA amplification: does "small" really mean "efficient"? *Lab on a Chip* **1** (2), 24N–29N.

Drese, K. S., Sörensen, O., Solli, L. A. & Gulliksen, A. 2003 Design and realization of a lab-on-a-chip system for multiple real-time detection of nucleic acid sequence-based amplification (NASBA). In *smallTalk 2003, San Jose, CA, USA*.

Elias, H. G. 1997 *An introduction to polymer science*. NY: VCH, NY.

Gulliksen, A., Solli, L., Karlsen, F., Rogne, H., Hovig, E., Nordstrom, T. & Sirevag, R. 2004 Real-time nucleic acid sequence-based amplification in nanoliter volumes. *Analytical Chemistry* **76** (1), 9–14.

Heiles, H. B. J., Genersch, E., Kessler, C., Neumann, R. & Eggers, H. J. 1988 Insitu hybridization with digoxigenin-labeled DNA of human papillomaviruses (HPV 16/18) in HeLa and SiHa cells. *Biotechniques* **6** (10), 978–981.

Jenkins, D. 2001 Diagnosing human papillomaviruses: recent advances. *Current Opinion in Infectious Diseases* **14** (1), 53–62.

Kraus, I. 2004 personal communication.

Kraus, I., Molden, T., Erno, L. E., Skomedal, H., Karlsen, F. & Hagmar, B. 2004 Human papillomavirus oncogenic expression in the dysplastic portio; an investigation of biopsies from 190 cervical cones. *British Journal of Cancer* **90** (7), 1407–1413.

Leone, G., van Schijndel, H., van Gemen, B., Kramer, F. R. & Schoen, C. D. 1998 Molecular beacon probes combined with amplification by NASBA enable homogeneous, real-time detection of RNA. *Nucleic Acids Research* **26** (9), 2150–2155.

Mincheva, A., Gissmann, L. & Zurhausen, H. 1987 Chromosomal integration sites of human papillomavirus DNA in 3 cervical-cancer cell-lines mapped by insitu hybridization. *Medical Microbiology and Immunology* **176** (5), 245–256.

Muñoz, N., Bosch, F. X., de Sanjosé, S., Herrero, R., Castellsagué, X., Shah, K. V., Snijders, P. J. F. & Meijer, C. J. L. M. 2003 Epidemiologic classification of human papillomavirus types associated with cervial cancer. *The New England Journal of Medicine* **348** (6), 518–527.

Niesters, H. G. M. 2001 Quantitation of viral load using real-time amplification techniques. *Methods* **25** (4), 419–429.

Syrjanen, S., Partanen, P., Mantyjarvi, R. & Syrjanen, K. 1988 Sensitivity of insitu hybridization techniques using biotin-labeled and s-35-labeled human papillomavirus (HPV) DNA probes. *Journal of Virological Methods* **19** (3-4), 225–238.

Walboomers, J. M. M., Jacobs, M. V., Manos, M. M., Bosch, F. X., Kummer, J. A., Shah, K. V., Snijders, P. J. F., Peto, J., Meijer, C. J. L. M. & Muñoz, N. 1999 Human papillomavirus is a necessary cause of invasive cervical cancer worldwide. *Journal of Pathology* **189** (1), 12–19.

Chapter 5

A non-contact pump mechanism for parallel movement of nanoliter sized liquid plugs using flexible diaphragms

Lars A. Solli[1,2], Anja Gulliksen[2,3], Liv Furuberg[4], Olaf Sörensen[5], Frank Karlsen[2,6], Lars R. Sætran[1], Henrik Rogne[4] & Klaus S. Drese[5],
[1]Dept. of Energy and Process Engineering, Norwegian University of Science and Technology, Kolbjørn Hejes vei 1B, 7491 Trondheim, Norway
[2]NorChip AS, Industriveien 8, 3490 Klokkarstua, Norway
[3]Dept. of Molecular Biosciences, University of Oslo, Kristine Bonnevies hus, 0316 Oslo, Norway
[4]Dept. of Microsystems, SINTEF ICT, P.O. Box 124 Blindern, 0314 Oslo, Norway
[5]Institut für Mikrotechnik Mainz GmbH, Carl-Zeiss-Strasse 18-20, 55129 Mainz, Germany
[6]Institute for Microsystems Technology, Vestfold University College, P.O. Box 2243, 3103 Tønsberg, Norway
(Manuscript for journal publication)

A novel non-contact pump mechanism for metering and movement of nanoliter sized liquid plugs in parallel channels has been developed. This work presents one part of the development of a lab-on-a-chip technology platform for point-of-care diagnostics. The cyclic olefin copolymer microchip has twelve parallel reaction channels with four pumps each, which are able to simultaneously move twelve sample plugs four steps in total. The combination of on-chip flexible diaphragms and actuation pins in a surrounding instrument constitute the pumps. We present results on the functioning and precision of the membrane pumps. Effects related to the membrane material, channel geometry, wall pinning, and pump chamber

geometries are examined. The risk of cross contamination is drastically reduced between and within subsequently analyzed chips. However, evaporation of liquid reduces the pump quality and the inaccuracy in the positioning indicates the need for improvements of membrane material.

5.1 Introduction

Medical diagnostics based on microfluidic systems are currently being proposed for a variety of applications (Verpoorte (2002), Weigl *et al.* (2003) and Li (2006)). Microsystem solutions provide low-cost tests with rapid results using disposable microchips. The chips are inserted into automated instruments which can be used by non-qualified personnel. The goal is to create instruments where a sample (e.g. blood or saliva) can be inserted into a chip and the diagnostic results are displayed in a panel shortly after. The sample has to be guided through the microfluidic chip where all necessary reactions must take place, by the means of a micropump (Laser & Santiago, 2004).

An advantageous option for lab-on-a-chip systems is the ability to divide the sample into discrete independently controllable nanoliter sized liquid plugs. Transporting samples in liquid plugs bears some advantages over the usual continuous-flow systems. A microfluidic operation can be reduced to a set of repeated basic operations, i.e., moving one plug over one unit of action area. This method also facilitates utilization of the recirculating flow pattern (Duda & Vrentas, 1971) within the plug to minimize the time of both mixing and heat transfer.

The group of Burns *et al.* reported in 1998 a plug-based integrated device for amplification and separation of DNA, where the movement of the plugs was based on external pneumatic control combined with on-chip vents and hydrophobic patches. Usually, external pneumatic control is handled by a pressure source or a syringe, while on-chip solutions might use ferrofluid as a dynamic plunger (Sörensen *et al.*, 2003). Several other transport methods in microscale segmented gas-liquid flow systems have been investigated, e.g. thermocapillary pumping (Burns *et al.*, 1996), electrowetting (Beni & Tenan, 1981), and thermopneumatic (Handique *et al.*, 2001).

We are in the process of developing a fully automated lab-on-a-chip device with no operating protocols for detecting human papillomavirus (HPV) cervix cancer markers (Gulliksen *et al.* (2004) and Gulliksen *et al.* (2005)). This online technology identifies high-risk HPV mRNA transcripts employing real-time nucleic acid sequence-based amplification (NASBA) (Compton (1991), Leone *et al.* (1998), Kraus *et al.* (2004) and Cuschieri *et al.* (2004)). The microfluidic chip consists of two parts: A sample preparation chip (not reported here), which

concentrates and extracts nucleic acids from a patient sample, and a NASBA chip, which amplifies and detects mRNA. This work documents a solution for the pumping mechanism in the NASBA chip.

In the NASBA chip, the injected sample containing mRNA will be split into several plugs, for simultaneous analysis of different HPV viruses, along with negative, positive (artificial oligos), and human U1A sample control (Sillekens *et al.*, 1987). Each of the plugs will be metered to have a well-defined volume. Subsequently, the plugs are pushed through the chip, in parallel channels. Each sample plug must be halted three times at exact channel positions for mixing with dried reagents and finally also at an optical window for detection of a possible NASBA amplification. Capillary forces are utilized for pulling the sample into the chip and draining the excess sample into the waste chamber. In addition a pump mechanism is needed for metering and positioning the plugs.

The risk of cross contamination between on-chip reaction channels must be avoided, as well as contamination of instrument parts which severely will endanger sequential chip analysis. Thus, a non-contact pump mechanism that exclusively works on one reaction channel each, is preferred. We present a pump mechanism based on on-chip chambers with lids that are initially pressed down by pins actuated by the handling system. When the pins are lifted, the plug is pulled towards the expanded chamber. A similar mechanism has previously been used to inject sample from on-chip reservoirs (Solignac & Gijs, 2003).

This paper presents a lab-on-a-chip system for plug-based real-time NASBA detection in cyclic olefin copolymer (COC) microchips with 95 nl plug volumes. It reports on experiments on the controllability of plug metering and positioning, using the chip membrane as pumps, whereas the previous work12 showed optical detection of artificial HPV 16 sequences and SiHa cell line samples using the NASBA technology in the same microchip.

5.2 Materials and methods

5.2.1 Microchip fabrication

The microchips were fabricated using injection moulding (Elias, 1997) of COC polymer (Grade 8007, Topas Advanced Polymers GmbH, Germany). The mould insert was manufactured with ultra precision milling of nickel. The microchips were oxygen plasma activated prior to coating with 0.5% (w/v) polyethylene glycol (PEG, P2263, Sigma-Aldrich Co.) in methanol.

The chip (see Fig. 5.1a) is a 2 mm thick COC substrate embodying on one side the microstructures and on the other side pockets for thermal control. The sealing foil is a 75 μm thick COC membrane acting as a top cover for the microstructures

(not visible in the figure). The membrane was sealed to the substrate using solvent bonding with cycloolefin. The COC is hydrophobic of nature and the PEG-coated COC is hydrophilic of nature. A cotton linter filter (Schleicher & Schuell BioScience GmbH, Relliehausen, Germany) was placed in the waste chamber to provide a driving force to drain the excess sample.
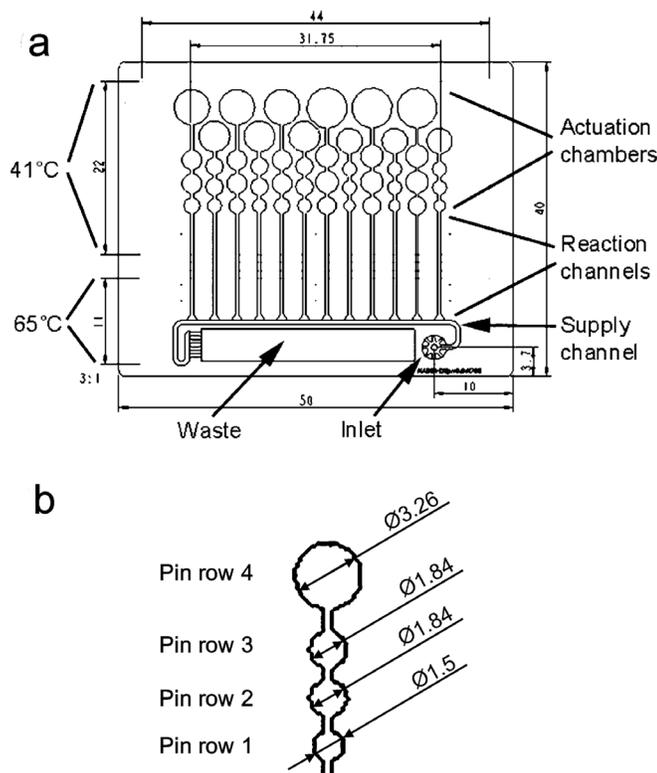
Figure 5.1: Illustrations of the NASBA microchip. All dimensions are in millimetres. **a** The two thermal pockets are displayed as the light grey areas as pointed to by the 41°C and the 65°C text, respectively. The waste chamber has an opening in the end close to the inlet. The delta shaped areas that connect the reaction channels with the supply channel are present to ease the filling procedure due to smoother corners. The inlet is designed to maintain the liquid plug in position above the inlet area, ensuring successful filling. **b** Segment of the actuation chambers of the reaction channel to the very right in Fig. 5.1a. Each channel has four individual diaphragm pump chambers; one for metering and three for movement. In total the chip has 48 chambers in twelve separate channels. The four chambers are located on horizontal lines as represented by the pin row numbers.

104

5.2.2 Diaphragm pumps chamber design

The inlet, located at the lower right hand side of the chip in Fig. 5.1a, is connected to a waste chamber through the supply channel. The supply channel has a cross-section of 550×550 μm^2. The waste chamber has venting to the outside atmosphere. Perpendicular to the supply channel are twelve parallel closed-end reaction channels, with a cross-section of 400×100 (width×depth) μm^2. The reaction channels have four rounded chambers each, called actuation chambers, at their end. These four chambers work as diaphragm pumps, which will transport the liquid in four steps into the reaction channel. In order to test liquid sample transport compared to actuation chamber sizes, four different sets of chambers are designed on one chip (see Fig. 5.1a. From left to right: Channels 1,3,5 and 2,4,6 and 7,9,11 and 8,10,12 are equal). It was found that channels 8, 10 and 12 resulted in the best plug positioning over the three reaction sites, where the mixing and the optical read-out are located. The chamber diameters of the four chambers in these channels were 1.5, 1.84, 1.84 and 3.26 mm (see Fig. 5.1b).

5.2.3 Mechanical actuation

The pump principle is illustrated in Fig. 5.2a. Volume is increased by the release of a deflected diaphragm. The liquid plug enters a new equilibrium position downstream the channel. The actuation mechanism consists of 48 spring-loaded pins (GSS-3 series, Interconnect Devices, Inc., KS, USA) with a rounded tip and a head diameter of 1.96 mm, assembled in two blocks. The upper block in Fig. 5.2b contains the pins for row 2, 3 and 4 (see Fig. 5.1b). The rows are in a staircase formation. The block is mounted to a robotic shaft movable in the longitudinal axis of the pins. The staircase formation of the pin rows and the springs enable the ability to release the pumps in pin row 2 simultaneously, followed by pin row 3 and 4, by elevating the block in three steps. The second block in Fig. 5.2b contains the first pin row and is mounted on a magnetic actuator. This allows faster response time of the pin actuation[1]. Fig. 5.2c illustrates how the pin deflects the membranes of the four actuation chambers. As the illustration shows the pin head is larger than chamber 1, 2 and 3, i.e. the pin will not hit the bottom in these chambers.

5.2.4 Instrument

Fig. 5.2d displays a photograph of the major components in the instrument. The parts that compose the optical system are described in Gulliksen *et al.* (2005). The instrument further comprises two Peltier elements (Marlow Industries Inc., Dallas,

---

[1]This was originally intended to aid the mixing of the dried chemicals into the liquid sample, but this is not reported in this work.
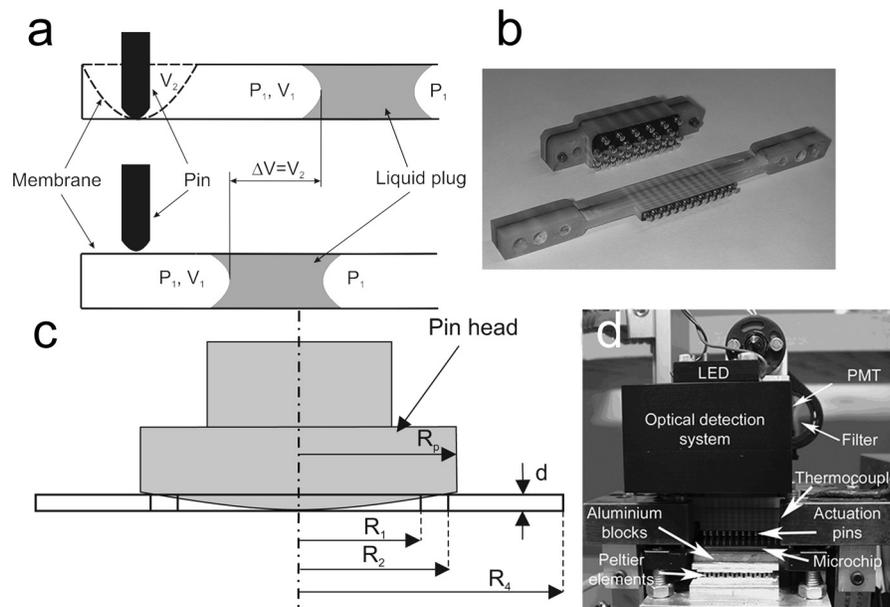
Figure 5.2: a Principle sketch of the pin actuation. Both sketches illustrate a cross-section of a reaction channel with a sample plug in equilibrium and an actuation chamber at the left end. The upper sketch displays a pin which is pushing the membrane down in the actuation chamber, thus creating a displaced volume. The lower sketch presents a situation where the pin has been elevated. When revealing the displaced volume, the pressure in the confined volume at the end of the reaction channel decreases. Thus, the pressure in front and rear of the plug are no longer in equilibrium and the plug will move to the left to again resituate in equilibrium. **b** Photograph of the two blocks that contain the pin rows. **c** Illustration of a pin head in chambers 2, 3 and 4. *d* is the depth of the chambers and R_p, R_1, R_2 and R_4 are the radii of the pin head, chamber 1, chamber 2 (and 3) and chamber 4, respectively. The height of the spherical cap that constitutes the tip of the pin equals the depth of the chambers *d*. **d** Photograph of the major components in the custom-made instrument.

TX) with aluminum blocks mounted on top to form the chip holder. A thermal pad was placed on the blocks for thermal contact to the chip. A thermocouple was integrated into the chip holder, with feedback to the Peltier elements. The system was calibrated with a commercial temperature calibration instrument (Fluke, Everett, WA) and platinum resistance sensors, both with an accuracy of $\pm 0.1°$C. Temperature calibrations were performed both on the aluminum block, and on top of a dummy microchip, without a membrane. The overall temperature accuracy of the system was within $\pm 1°$C.

The instrument was equipped with a chip holder movable in two axes for pin elevation and optical positioning. The servomotors (Omron Electronics,

Kyoto, Japan) were regulated by a physical signaling sublayer (PLS) (Saia-Burgess Electronics AG, Murten, Switzerland), programmed with PG 5 (Saia-Burgess Electronics AG).

All communications were run through a serial line (RS232) and controlled externally by MATLAB (The MathWorks Inc., Natick, MA).

5.3 Experimental procedure

5.3.1 Liquid sample material

The sample material used in the experiments is a NASBA mixture (PreTect® HPV-Proofer kit (NorChip AS, Norway)). See Gulliksen *et al.* (2005) for details about the sample. This solution does not contain any targets, so no amplification will be present in the experiments. The sample proved to have wettable characteristics to both the non-coated lid surface and the PEG-coated microchannel surface. The sample liquid exhibited a contact angle of 56.4° and 25° on the COC and the PEG-coated COC, respectively, when investigated with the sessile drop method. The surface tension in air of the liquid was 35 mN m^{-1}, when investigated with the pendant drop method. All the measurements were conducted in room temperature with the DROP instrument (University of Oslo, Norway).

5.3.2 Metering and isolation of sample plugs

Metering is accomplished by the combination of capillary forces and the first set of pumps. As capillary forces pull the liquid sample through the supply channel, the cross-section difference between the supply channel and the reaction channels ensures that liquid is also pulled into the reaction channels. The capillary pressure across a meniscus in a microchannel with a lid of different wetting behaviour, can be expressed as (Lee *et al.*, 2003):

$$\Delta p = \gamma \cos\left(\theta_{chip}\right)\left(\frac{2d + w}{dw}\right) + \gamma \cos\left(\theta_{lid}\right)\left(\frac{w}{wd}\right). \tag{5.1}$$

Here, w is the width, d is the depth, γ is the surface tension of the liquid and θ_{chip} and θ_{lid} are the contact angles of the chip and the lid, respectively. By inserting θ_{chip}=25°, θ_{lid}=56.4° and γ=35 mN m^{-1}, Eq. 5.1 yields $\Delta p = 669.5$ Pa. The reaction channels have initially an atmospheric pressure of 101325 Pa, thus the volume change is about 0.66%. The upstream closed volume in actuation channel 12 is at this stage calculated to be 1683 nl, hence the sample will enter ∼11 nl into the channel. Subsequently, the first pin row is elevated and the liquid is pulled a

distance into the reaction channel, defined by the first diaphragm pump. Further, the filter drains the excess sample in the supply channel, and the rear meniscus of the sample snaps off liquid at the intersection with the reaction channels, leaving separated sample plugs in the reaction channels. The filling- and draining process of the supply channel is a continuous procedure.

5.3.3 Principle of the NASBA chip

The principle of the whole NASBA procedure is presented step-by-step with timeline in Fig. 5.3a-h. The chip is in the initial state when all the chamber diaphragms are pressed down (a). Sample is introduced and pulled into the chip by capillary forces (b), plugs are metered (c) and excess sample is drained by the filter (d). The twelve sample plugs are moved to the two dried reagent spots (e and f), and finally to the last combined reagent and optical detection site (g), where the NASBA detection starts (h). The NASBA procedure requires heating in two steps. Initially a temperature of 65°C is needed for denaturation of the nucleic acids. Subsequently the temperature is lowered to 41°C for the amplification to take place (see Fig. 5.3). The first two reaction sites are at 65°C. The reaction mixture containing enzymes in the last reaction site must not exceed 42°C. In order to assure a certain safety margin, this part of the chip was only heated up to 39°C, while the other was kept at 65°C (see Fig. 5.3a-f).

5.3.4 Experimental

In order to saturate the humidity inside the chip, a 2 μl part of the sample was pre-injected into the chip and kept in the inlet area for approximately 5 minutes at the initial chip temperature of 65°C/39°C (see Fig. 5.3a). This procedure was implemented to reduce evaporation of sample and minimize its consequences such as sample displacement and volume loss. Next, a sample volume of 25 μl was applied to the inlet hole by a pipette. Capillary forces moved the sample into the chip and the elevation of the first pin row moved a defined sample volume into the twelve parallel reaction channels. The supply channel was subsequently drained by the filter, leaving 12 isolated sample plugs in each reaction channel. No dried analytes were present in the reaction sites during the experiments of this paper. This part will be presented in future work.

Optical monitoring of plug positioning in parallel channels is conducted with a DV-camera (Sony DCR-TRV30E) placed above the instrument. All pictures are taken five seconds after the pin elevation. Data for the plug movement are produced by measuring covered distances on larger paper reprints. The accuracy of the measurements is given from the pixel size on the reprints, which is about 43 μm on the microchip.
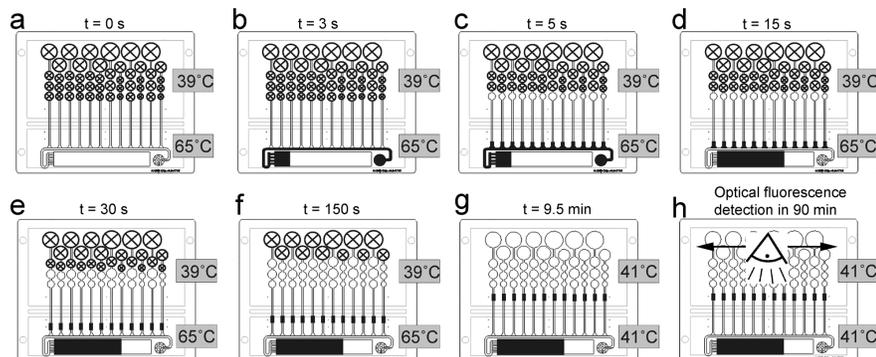
Figure 5.3: Schematic illustrations displaying the NASBA chip procedure step-by-step. A circle with a cross inside indicates that the membrane of the particular actuation chamber is pushed down. The grey boxes denote the temperature of the Peltier elements. The sample liquid is shown in black. Here, the four sets of actuation chambers are considered identical in order to emphasize the topical principle, hence, the equal sample movement. The timeline is included above each figure. **a** The chip in its initial position. All four pins impress the membranes into the actuation chambers. **b** Sample is applied to the inlet and the supply channel is filled due to capillary forces. **c** The first set of pins is elevated and sample is metered into the reaction channels. **d** The supply channel is drained into the waste chamber, leaving separated sample plugs in the reaction channels. **e** The second row of pins is elevated and the sample plugs are moved onto their first reaction site. **f** The third row of pins is elevated and the sample plugs are moved onto the second reaction site. **g** The fourth row of pins is withdrawn and the sample plugs are moved onto the third reaction site. **h** The NASBA amplification and detection start.

5.4   Results and discussion

Metering and movement of plugs, including heating procedure were conducted in 12 different microchips. The pictures in Fig. 5.4 show a typical result from one reaction channel. Parallel metering and movement were performed successfully in all twelve channels on each chip. However, in order to have realizable statistics, only channel 12 in the different chips was investigated.

The metering volume in the experiments produced plugs of sample volumes of 95.6±17.1 nl. Fig. 5.5 displays experimental data of the plug movement. Each middle point of the plug samples is monitored in the three movement steps to the three reaction sites. The positions are measured from the start of the reaction channel. The inset in Fig. 5.5 demonstrates the reproducibility of the actuation method. The error bars represent standard deviation based on the 12 reaction channels. The first reaction site has a mean position with standard deviation of 2.08±0.27 mm, the second 4.21±0.38 mm and the third 9.85±0.44 mm.
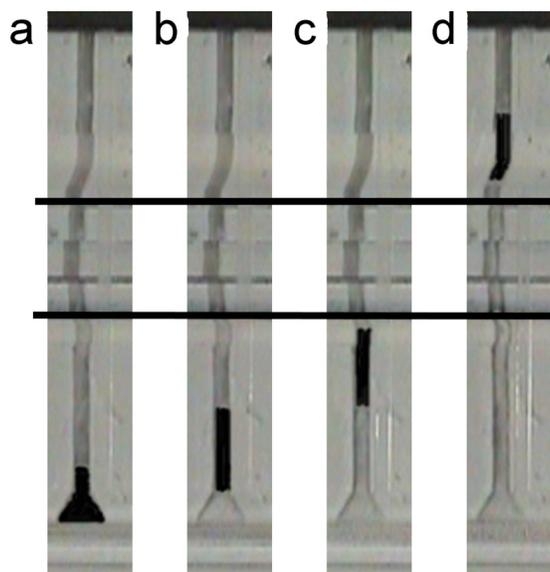
Figure 5.4: Picture series showing a typical result of a plug sample in reaction channel 12 displaced by the diaphragm pumps. The plug is coloured black for visualization purposes. The channels and plugs appear skewed in the images, because only their shadow is visible on the grey cover of the Peltier element. The horizontal lines represent the edges of the temperature zones. **a** Plug in metering position. **b** Plug moved to reaction site 1. **c** Plug moved to reaction site 2. **d** Plug moved to reaction site 3.

The measured effective pump volumes of the chambers are presented in Fig. 5.6. The graph shows pump volumes of actuation chamber 2, 3 and 4 of reaction channel 12. The data are collected by measuring the distance between the upstream meniscus of the plug before and after pin elevation. The second actuation chamber has a mean pump volume with standard deviation of 73.1 ± 11.3 nl, the third 82.9 ± 7.5 nl and the fourth 223.9 ± 11.9 nl. The horizontal lines in Fig. 5.6 represent calculated pump volumes; based on the volume of a spherical cap (height of 70 μm) for chamber 2 and 3 and a truncated cone (with radius of truncated area of 40 μm) for chamber 4. The latter model was chosen because in this case, the main part of the deflected diaphragm exhibits a linear shape, i.e. not curved as the deflection in the chambers comparable in size with the rounded pin head. The approximated values are 93.2 nl for actuation chamber 2 and 3, and 285 nl for actuation chamber 4. The experimental data of chamber 2 and 3 differ in average pump volumes by 13.4%, although the chambers are equal in size. Further, the estimated data diverge from the experimental by 27.5%, 12.4% and 27.3% for pump volumes 2, 3 and 4, respectively. Investigations showed that the observed deviations are caused by two main effects.
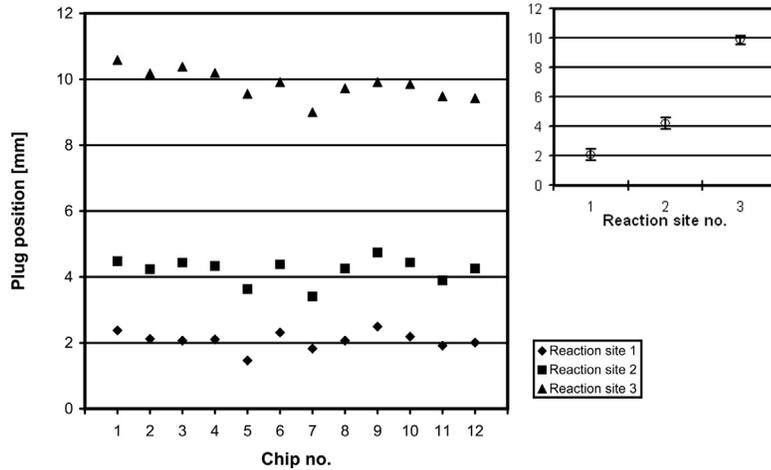
Figure 5.5: Graph showing plug positions of 12 different microchips. All points denote centre points of plugs in reaction channel 12. *Inset*: The open circles represent the average values of the middle position of the plug in the reaction sites. Standard deviations are included in the figure.
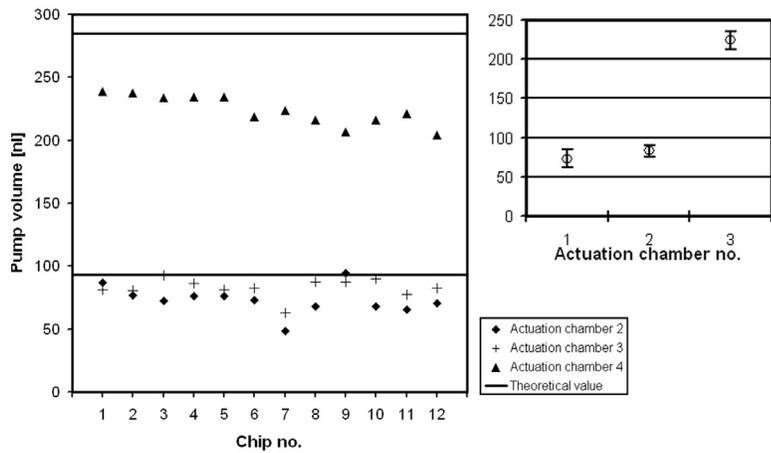
Figure 5.6: Graph showing pump volumes of actuation chamber 2, 3 and 4. The horizontal lines represent estimated pump volumes. *Inset*: The open circles represent the average values of the pump volume. Standard deviations are included in the figure.

The following sections will explain the apparent difference in pump volumes between chamber 2 and 3, the theoretical overestimation of pump volume, together with the noise in the pump volume data.

First, due to the larger width of the entrance of the reaction channel (1.59 mm) compared to its overall width (0.4 mm), the pump volume deviation between actuation chamber 2 and 3 is caused by the difference in capillary pressure of the plug in the metering position (see Fig. 5.4a). The pressure over the front- and the back meniscus of the whole plug Δp_{plug}, is given by:

$$\Delta p_{plug} = \Delta p_{front} - \Delta p_{back}. \tag{5.2}$$

By substituting Eq. 5.1 into Eq. 5.2, yields the following relation

$$\Delta p_{plug} = 2\gamma \cos\left(\theta_{chip}\right)\left(\frac{1}{w_f} - \frac{1}{w_b}\right), \tag{5.3}$$

where w_f and w_b are the widths of the front meniscus and back meniscus of the plug, respectively. By inserting the measured values, Eq. 5.3 yields $\Delta p = 594.4$ Pa. The reaction channels have initially an atmospheric pressure of 101325 Pa, thus the volume change are about 0.59%. The downstream closed volume in actuation channel 12 is at this stage calculated to 1624 nl, and given the assumptions above the effect of actuation chamber 2 is $\sim$10 nl less than chamber 3. This is in reasonable agreement with measured pump volumes in Fig. 5.4, as the corrected pump volumes of chamber 2 and 3 becomes comparable.

Secondly, the estimated pump volume of all chambers is reduced compared to the experimental data due to evaporation of the sample plugs. The experiments show a reduction in the measured total sample volume from the first position to the third position. The plug volumes were 89.3±13 nl, 86±13 nl and 81.9±13 nl when leaving reaction site 1, 2 and 3, respectively. Hence, the sample has lost a volume of 3.3 nl in 2 minutes on 65°C and 4.1 nl in 7 minutes where the temperature was reduced from 65°C to 41°C (see Fig. 5.3e and f), due to evaporation from both ends of the plugs. Further, evaporation increases the partial vapour pressures in the downstream closed side of the channel and thus expands its volume. The experiments reveal that the plugs, when in position of the two first reaction sites for mixing with dried reagents (in 2 minutes (Fig. 5.3e) and 7 minutes (Fig. 5.3f), respectively), are moved downstream before actuation of the following diaphragm pump. The data exhibits a variable behaviour, an expansion of the closed volume of 1.2±3.8 nl and 7.3±9.1 nl, during the elapsed time at the 2nd and the 3rd reaction sites, respectively. The evaporation effect is not quantified any further.

The variations within the experimental data are believed to be caused mainly by hysteresis effects. These are energy barriers which the fluidic interfaces must overcome before its liquid edge can advance further (Adamson & Gast,

1997). The channel surface was investigated using a white light interferometer (WYKO NT-2000, Veeco Instruments Inc., NY, USA). The RMS (root mean square) value of the surface roughness on the PEG coating was measured to be 0.5 μm. The measurements were conducted in a 400×450 μm^2 area inside the reaction channels. The data also show a maximum value of 1.55 μm. Pinning of menisci in microchannels with RMS roughness less than 1 nm has been observed (Jin & Breuer, 2003). Other possible hysteresis attributes are heterogeneous coating, chemical liquid-surface interactions and contamination such as dust in the channels (Adamson & Gast, 1997). These attributes are not investigated further. The effect of hysteresis is believed to have a distinct influence on liquid movement in this case of the gradually increasing volume caused by evaporation, rather than the movement due to the fast expansion of volume caused by the elevated diaphragms. Hence, it is likely to assume that the plugs are not in equilibrium positions when the diaphragm pumps are actuated, causing the pumps to achieve less than estimated.
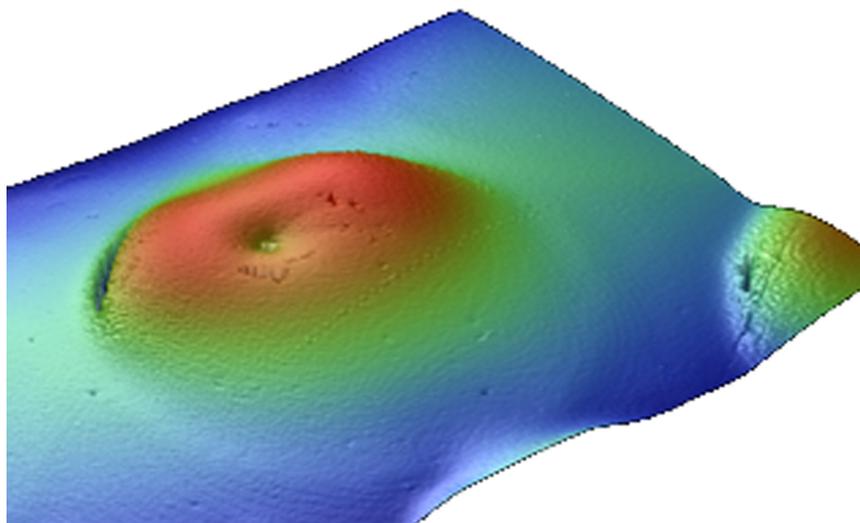
Figure 5.7: Picture showing a typical WYKO visualization of a membrane after pin actuation. Parts of two adjacent chambers are visible to the right and below of the main chamber. The blue colour represents low height values, while red represents high.

A total number of six diaphragms were also investigated in the WYKO, for inspection of effects from the direct impact of the pins and plastic deformations due to deflection. The diaphragms were examined both before and after pin actuation. A gold layer with a thickness of a few nanometres was sputtered onto the membrane in order to realize the measurements. A typical result is shown

in Fig. 5.7. The measurements showed a noteworthy plastic deformation in only one of the inspected diaphragms of approximately 2.5 nl, which is considered an insignificant contribution to the position inaccuracy. All diaphragms, however, showed a convex shape of 10 ± 2 μm before actuation, but exhibited irregular convex shapes of 5 ± 1.5 μm after actuation. This is due to different applied pin pressure and alignment. The unequal deformation may cause approximately 6.3 nl difference in the mid sized pumps, which are considered to be significant contribution to the variance of the pump volumes.

5.5 Conclusion and further work

A novel non-contact pumping mechanism consisting of flexible diaphragms and pins has been developed. The on-chip pumps successfully performed metering and movement of nanoliter sized liquid plugs in parallel channels, demonstrating that the pump mechanism has a potential for use in lab-on-a-chip applications.

The benefits of this system are the reduction of cross contamination risks between the twelve on-chip analysis channels, and also between the instrument parts and sequentially analysed chips. In addition, the pumps mechanism employs low-cost manufacturing, which facilitates disposable chips.

The range of the pumps may be optimized by adjusting the chamber sizes, so desired sample positions can be reached. However, the results proved that the effect of the pumps is reduced due to evaporation of the sample plugs and noise is generated from deformations of the diaphragms. Future microchips could contain valves such as geometrical restrictions in the channels combined with hydrophobic patches to aid position restriction of the plugs, while the membrane material must be changed into a more robust one. Careful design criteria must be pursued in order to decrease the evaporation, as i.e. reduction of on-chip dead volume to increase the efficiency of the vapour saturation.

5.6 Acknowledgements

References

ADAMSON, A. W. & GAST, A. P. 1997 *Physical Chemistry of Surfaces*, 6th edn. New York, NY: John Wiley & Sons, Inc.

BENI, G. & TENAN, M. A. 1981 Dynamics of electrowetting displays. *Journal of Applied Physics* **52** (10), 6011–6015.

BURNS, M. A., JOHNSON, B. N., BRAHMASANDRA, S. N., HANDIQUE, K., WEBSTER, J. R., KRISHNAN, M., SAMMARCO, T. S., MAN, P. M., JONES, D., HELDSINGER, D., MASTRANGELO, C. H. & BURKE, D. T. 1998 An integrated nanoliter DNA analysis device. *Science* **282** (5388), 484–487.

BURNS, M. A., MASTRANGELO, C. H., SAMMARCO, T. S., MAN, F. P., WEBSTER, J. R., JOHNSON, B. N., FOERSTER, B., JONES, D., FIELDS, Y., KAISER, A. R. & BURKE, D. T. 1996 Microfabricated structures for integrated DNA analysis. *Proceedings of the National Academy of Sciences of the United States of America* **93** (11), 5556–5561.

COMPTON, J. 1991 Nucleic-acid sequence-based amplification. *Nature* **350** (6313), 91–92.

CUSCHIERI, K. S., WHITLEY, M. J. & CUBIE, H. A. 2004 Human papillomavirus type specific DNA and RNA persistence - Implications for cervical disease progression and monitoring. *Journal of Medical Virology* **73** (1), 65–70.

DUDA, J. L. & VRENTAS, J. S. 1971 Steady flow in the region of closed streamlines in a cylindrical cavity. *Journal of Fluid Mechanics* **45**, 247–260.

ELIAS, H. G. 1997 *An introduction to polymer science*. NY: VCH, NY.

GULLIKSEN, A., SOLLI, L., KARLSEN, F., ROGNE, H., HOVIG, E., NORDSTROM, T. & SIREVAG, R. 2004 Real-time nucleic acid sequence-based amplification in nanoliter volumes. *Analytical Chemistry* **76** (1), 9–14.

GULLIKSEN, A., SOLLI, L. A., DRESE, K. S., SÖRENSEN, O., KARLSEN, F., ROGNE, H., HOVIG, E. & SIREVÅG, R. 2005 Parallel nanoliter detection of cancer markers using polymer microchips. *Lab on a Chip* **5** (4), 416–420.

HANDIQUE, K., BURKE, D. T., MASTRANGELO, C. H. & BURNS, M. A. 2001 On-chip thermopneumatic pressure for discrete drop pumping. *Analytical Chemistry* **73** (8), 1831–1838.

Jin, S. & Breuer, K. S. 2003 Diffusion-limited evaporation in long microchannels. In *Proceedings of IMECE03, 2003 ASME International Mechanical Engineering Congress & Exposition, November 16-21, 2003, Washington, DC USA*. ASME.

Kraus, I., Molden, T., Erno, L. E., Skomedal, H., Karlsen, F. & Hagmar, B. 2004 Human papillomavirus oncogenic expression in the dysplastic portio; an investigation of biopsies from 190 cervical cones. *British Journal of Cancer* **90** (7), 1407–1413.

Laser, D. J. & Santiago, J. G. 2004 A review of micropumps. *Journal of Micromechanics and Microengineering* **14** (6), R35–R64.

Lee, S. H., Lee, C. S., Kim, B. G. & Kim, Y. K. 2003 Quantitatively controlled nanoliter liquid manipulation using hydrophobic valving and control of surface wettability. *Journal of Micromechanics and Microengineering* **13** (1), 89–97.

Leone, G., van Schijndel, H., van Gemen, B., Kramer, F. R. & Schoen, C. D. 1998 Molecular beacon probes combined with amplification by NASBA enable homogeneous, real-time detection of RNA. *Nucleic Acids Research* **26** (9), 2150–2155.

Li, P. C. H. 2006 *Microfluidic Lab-on-a-Chip for Chemical and Biological Analysis and Discovery*, 1st edn. Boca Raton, FL: Taylor & Francis Group.

Sillekens, P. T. G., Habets, W. J., Beijer, R. P. & Vanvenrooij, W. J. 1987 cDNA cloning of the human U1 snRNA-associated a protein - extensive homology between U1 and U2 snRNP-specific proteins. *Embo Journal* **6** (12), 3841–3848.

Solignac, D. & Gijs, M. A. M. 2003 Pressure pulse injection: a powerful alternative to electrokinetic sample loading in electrophoresis microchips. *Analytical Chemistry* **75** (7), 1652–1657.

Sörensen, O., Drese, K. S. & Hardt, S. 2003 Liquid slug transport, synchronization and mixing driven by ferrofluids. In *Proc. of the μTAS Symposium (μTAS 2001), Squaw Valley, CA, USA, Oct 2003*, pp. 1029–1032.

Verpoorte, E. 2002 Microfluidic chips for clinical and forensic analysis. *Electrophoresis* **23**, 677–712.

Weigl, B. H., Bardell, R. L. & Cabrera, C. R. 2003 Lab-on-a-chip for drug development. *Advanced Drug Delivery Reviews* **55** (3), 349–377.

Chapter 6

Flow visualization and simulation of discrete liquid droplets moving in microchannels

Lars A. Solli[1,2], Michal M. Mielnik[1], Frank Karlsen[2], Lars R. Sætran[1] & Liv Furuberg[3]

[1]Dept. of Energy and Process Engineering, Norwegian University of Science and Technology, Kolbjørn Hejes vei 1B, 7491 Trondheim, Norway
[2]NorChip AS, Industriveien 8, 3490 Klokkarstua, Norway
[3]Dept. of Microsystems, SINTEF ICT, Forskningsveien 1, 0314 Oslo, Norway

We present experiments visualizing the flow pattern inside droplets moving in microchannels. Micro-Particle Image Velocimetry shows a recirculation pattern of liquid flow within the droplets. The experimental results correspond well with the computational fluid dynamic analysis. We characterize the flowfield inside two different sized droplets moving in a straight microchannel for Reynolds numbers as low as 0.008. Depending on the droplet length, we observe different flow profiles predictable by theory. The recirculation flow can be utilized for mixing of reagents within moving droplets. Continuous flow of a liquid through a straight microchannel in the low Reynolds number regime implies parallel streamlines. Thus mixing is caused by molecular diffusion. Splitting the liquid into moving droplets introduces the recirculation streamlines and thus convective mixing. Therefore, a significant reduction of the mixing time can be achieved.

6.1 Introduction

Microfluidic systems are the core components of a wide variety of medical diagnostic instruments (Verpoorte (2002) and Tüdős *et al.* (2001)). Microsystem solutions provide low-cost tests with rapid results using disposable microchips. The chips are inserted into automated instruments which can be used by non-qualified personnel. The goal is to create instruments where a sample droplet (e.g. blood or salvia) can be inserted into a chip and the diagnostic results are displayed in a panel shortly after. The sample droplet then has to be guided through the microfluidic chip where all necessary reactions must take place.

We are in the process of developing a fully automated lab-on-a-chip device with no protocols for detecting human papillomavirus (HPV) cervix cancer markers (Gulliksen *et al.*, 2005). Most of the current available commercial diagnostic devices based on molecular markers require substantial support equipment outside of the microfluidic components themselves. They therefore have to be handled by qualified lab-personnel. Cepheid (USA) has developed a commercial fully automatic analysis system, but our new system will use much smaller detection volumes (saves reagent costs) and detect more targets in parallel (10 HPV markers). Also Xtrana Inc. and Motorola are US companies that have developed prototypes of fully automatic analysis instruments, but no commercial products.

One important function in a fully automatic analysis system is to mix the sample with reagents or enzymes. These can be liquids injected through side channels or solid state powder. Mixing is also crucial in other types of microfluidic systems, such as microreactors and chips for drug discovery.

Due to size, fluidics in microchannels are usually dominated by laminar flows of low Reynolds number (Re) and thus mixing becomes a serious challenge, because only molecular diffusion is predominant on these length scales. The diffusion length, L_d is the characteristic length scale for diffusion of a particle in the fluid in a given time. It increases as the square root of the time:

$$L_d \approx \sqrt{2Dt_d}, \tag{6.1}$$

where t_d is the time and D is the diffusion constant, respectively. This implies that a typical particle will have diffused a length comparable to the system size d after a time t_d:

$$t_d \approx \frac{d^2}{2D}. \tag{6.2}$$

Considering a typical microchannel of the order of 100 μm and 100 nm sized particles with diffusion constant D in the order of 10^{-8} cm^2 s^{-1}, the total mixing

time, t_d becomes equivalent to several minutes. As the above equation suggests, one can dramatically reduce the mixing time by reducing the diffusion length required or increasing the contact area between the two miscible reagents liquids while keeping the volume constant.

For a continuous flow system, where two miscible liquids are merged into one channel, mixing requires long channel distances ($\gg$ 1 cm) which are generally not preferred in a microsystem. In order to enhance the mixing process in such flows, several methods involving the liquid streams to be mixed have been developed and studied. Continuous micro-mixers can be categorized as using either active or passive means. Active micro-mixers use external fields to agitate the flow and creating temporary chaotic fluctuations. The agitating field can be mechanical (Lu *et al.*, 2001), electrokinetic (Oddy *et al.*, 2001), magneto hydrodynamic (Bau *et al.*, 2001) or acustic (Yang *et al.*, 2001). Passive micro-mixers involves means to reduce the diffusion path between fluid streams by splitting and recombining the flow (Schwesinger *et al.*, 1996), with the use of i.e. nozzle effect (Veenstra *et al.*, 1999) or coanda effect (Hong *et al.*, 2001). Several passive chaotic methods are of the most resent contribution. This implies advanced 3D structures such as to demonstrate stirring by chaotic advection (Liu *et al.* (2000) and Stroock *et al.* (2002)).

Droplet-based microfluidics in a diagnostic system introduces a number of advantages. The advantages regards mixing and also the isolation of a precise volume of the sample and reagent. Splitting a large sample droplet into smaller droplets that are mixed with different reagents makes it possible to handle very small volumes in the nanoliter range and practice multiple analyses in parallel (Drese *et al.* (2003) and Gulliksen *et al.* (2005)).

A droplet moving in a microchannel develops a recirculating flow within itself (Duda & Vrentas (1971) and Taylor (1961)). Furthermore, these recirculation streamlines allows convective mixing of solutes in addition to molecular diffusion. Similar to the drawback with continuous micro-mixers, this effect can only be sustained by enduring the flow momentum. However, droplet-based flow can to a greater extent utilize the option of alternating the flow directions. This recirculation effect has been alluded to in the works of Burns *et al.* (1998), Katopodes *et al.* (2000) and Sammarco & Burns (1999). For the purpose of mixing a few groups presents both experimental work (Burns & Ramshaw (2001) and Fowler *et al.* (2002)) and simulations (Bringer *et al.* (2004) and Handique & Burns (2001)). Most recently Lammertink *et al.* (2004) reported on the possibility of mixing, utilizing this effect by counterbalancing hydrodynamic pressure against electroosmotically generated flow in closed channels and Günther *et al.* (2004) reported on using micro-PIV and fluorescence microscopy techniques

to characterize the flow pattern within microscale segmented[1] gas-liquid flow at superficial velocities.

In a fully automated analysis system, even the injection of two different liquids will complicate the analysis for the operator using the lab-on-a-chip system. In our lab-on-a-chip dried reagents will be stored inside the chip. Dried enzymes are particularly advantageous for disposable devices, as it not only simplifies the operation, but provides greater portability, long-term storage and reduces the risk of contamination drastically. The use of dried enzymes has never been explored in such microfluidic systems before. However, Garcia *et al.* (2004) reports on controlled dissolution of dried protein in a micro cavity.

Our aim is to develop droplet based devices with on-chip stored dried enzymes that are capable of carrying out several qualitative bioassays in parallel. This requires mixing of enzymes with the sample droplets. The liquids in our system will be driven by a simple external pump only, and therefore it is important to explore the mixing effect of a moving droplet.

We present experimental micro-Particle Image Velocimetry (micro-PIV) results that visualize the hydrodynamic flow pattern within a liquid plug moving in a microchannel. The experimental results correspond well with our results from computational fluid dynamics (CFD) simulations. A recirculation flow field is measured and we make remarks on the efficiency of the recirculation pattern regarding mixing of reagents within a moving droplet. Also, we measure the transition from a two-cell recirculation pattern to a four-cell recirculation pattern for decreasing droplet aspect ratios.

6.2 Theory

6.2.1 The continuum hypothesis

In general, the fluids of macroscopic perspective can be treated as continuous isotropic matter. The continuum description could however be questioned because of the small length scales present in microfluidic flows. One way of defining deviations from the continuum description is through a precision criterion. An example could be to determine the mass density to a certain relative precision r.

- Example
  Consider N number of molecules of a mass m in a small volume $V = l^3$.
  The mass density can be written $\rho = mN/V$. There are only fluctuations in
  the relative number of molecules ΔN due to random walk which is typically

---

[1]In this work the term droplet-flow is the preferred nomenclature. There are also terms as plug- or slug-flow in the available literature, but there is no unanimous use of terms.

$\Delta N \approx \sqrt{N}$. For $r = 1\%$ the requirement $\Delta N / N < r$ yields $N > 1/r^2 = 10^4$. The given volume V hence needing dimensions $l > 22 L_{mol}$, where L_{mol} is the intermolecular length (bond length). The volume occupied by one molecule L_{mol}^3 is approximated using $L_{mol} = (M_{mol}/\rho N_A)^{1/3}$, where ρ is the density, M_{mol} is the molar mass and N_A is Avogado's number. For water $L_{mol} \approx 0.31$ nm, which implies that $l > 7$ nm.

This is a factor of 10^5 smaller than the geometric dimensions of the microfluidic channels analysed in this paper, which implicates that the continuum assumption is still relevant.

6.2.2   Governing equations for single-phase flow

Adopting the continuum assumption and considering incompressibility, Newtonian flows in microchannels can be modeled by the Navier-Stokes equations. The governing equations of fluid flow are the continuity and momentum equations, which are given respectively, by

$$\nabla \cdot \boldsymbol{V} = 0 \tag{6.3}$$

and

$$\rho \frac{D\boldsymbol{V}}{Dt} = \rho \left(\frac{\partial \boldsymbol{V}}{\partial t} + \left(\boldsymbol{V} \cdot \nabla \right) \boldsymbol{V} \right) = -\nabla p + \mu \nabla^2 \boldsymbol{V} + \rho \boldsymbol{F}, \tag{6.4}$$

where $\boldsymbol{V} = (u, v, w)$ is the velocity vector, ρ is the fluid density, μ is the absolute viscosity of the fluid, p is the applied pressure and $\boldsymbol{F}$ is an external force vector (i.e. gravitational, magnetic). The left side of Equation 6.4 represents inertial forces, while the right hand side represents forces due to applied force, pressure and viscosity.

6.2.3   Micro scale flow

The flow is usually characterized by the ratio of the inertial and viscous forces, the Reynolds number:

$$Re = \frac{\rho U x}{\mu}. \tag{6.5}$$

Equation 6.5 is written in terms of the characteristic size (typically the smallest dimension) of the channel, x and the characteristic flow velocity, U. Microfabricated fluid systems usually involves small sizes and slow velocities, thus flow of these systems are often in the low Reynolds number regime ($Re << 1$).

The flow is restricted to the laminar flow regime, where the inertial effects which causes turbulence and secondary flows, are negligible. Considering this assumption and neglecting the body forces the momentum equation (Eq. 6.4) is reduced to:

$$\rho\frac{\partial \boldsymbol{V}}{\partial t} = -\nabla p + \mu\nabla^2 \boldsymbol{V}. \tag{6.6}$$

## 6.2.4 Discrete droplet-flow

The liquid inside a discrete drop that moves in a microchannel recirculates within itself. This was first described experimentally by Taylor (1961) and analytically by Duda & Vrentas (1971). As the drop moves in the channel, liquid moves from the centre of the drop and adheres to the walls at the front end of the drop. At the back end of the drop, liquid moves from the wall to the centre of the drop. This exchange of liquid at the boundaries and the continuity of liquid within the drop causes closed streamlines within the drop.

Duda & Vrentas (1971) developed an analytical solution to describe the steady, closed streamline velocity field within a cylindrical cavity with a uniformly translating wall at low Reynolds numbers. Their work characterized the liquid drops in a non-dimensional scale, defining the aspect ratio β,

$$\beta = \frac{L}{h} \tag{6.7}$$

where L is the length of the drop and h is the radius of the drop. The group assumed symmetry in the azimuthal direction and calculated the streamline pattern for $y = [0, h]$ for $\beta = 0.5$, 1, 5 and 20. The work concluded that there are four-cell recirculation patterns for $\beta = 0.5$, and a two-cell recirculation pattern for $\beta = 1$, 5 and 20. We preformed CFD analysis for illustrational purposes and a two-cell recirculation pattern is shown in Figure 6.1, while Figure 6.2 shows a four-cell recirculation pattern.

To create a simplified solution to a flow profile for the drop in Figure 6.1, we follow the arguments of Handique & Burns (2001), who assumed a long drop moving in a slit-type (width $\gg$ depth) microchannel, implying a 2D solution. The physical properties of the liquid (viscosity and density) are assumed to be uniform and constant over the whole liquid. The two meniscuses on each side of the droplet are modelled as fixed solid walls. The upper and bottom walls move at a constant speed V_d. The drop is very long compared to the depth of the channel. In the middle section of the droplet, the velocity of the fluid elements (V_{rel}) with respect to the drop translating at a constant velocity (V_d) can be estimated as Poiseuille flow (parallel plate) as
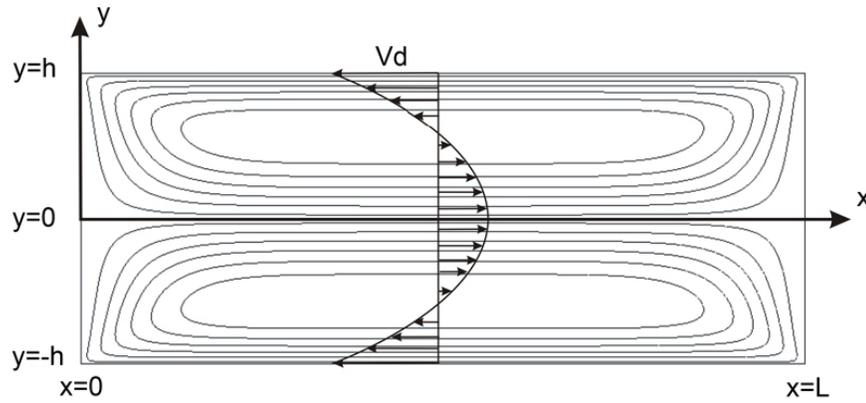
Figure 6.1: Illustration based on a CFD simulation showing a two-cell recirculation pattern in a liquid drop moving at a constant uniform velocity. The frame of reference is moving at the average velocity of the drop (V_d).
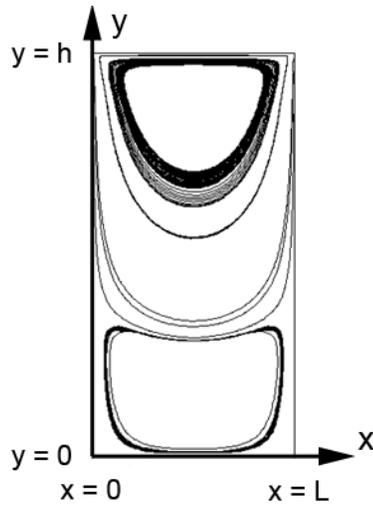
Figure 6.2: Illustration based on a CFD simulation showing a four-cell recirculation pattern for a droplet with $\beta = 0.5$. Note that the illustration is only presenting the upper part of the droplet along the symmetry axis x.

$$V_{rel}(y) = 0.5V_d\left(1 - 3\left(\frac{y}{h}\right)^2\right), \tag{6.8}$$

where V_{rel} is the velocity of a streamline at a distance y from the centreline axis.

6.3 Experimental and simulation

6.3.1 Microfluidic device

The experiments are conducted using a square borosilicate glass channel with a cross-section of 100×100 μm^2 (Wale Apperatus, Inc.). The channel was coated with Sigmacote (Sigma-Aldrich Co.), to prevent the particles from attaching to the glass channel. Figures 6.3a and b shows a picture and a sketch of the experimental set-up and the channel, respectively. The glass channel was glued to a syringe.
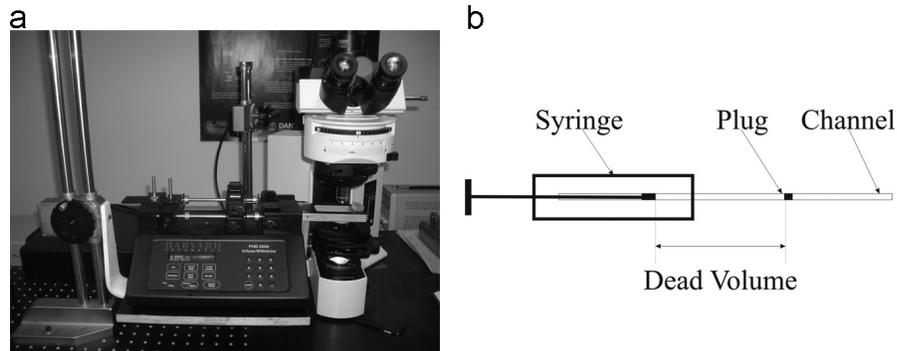
Figure 6.3: a Picture of the set-up. The syringe pump (middle) was placed on a lift (left) controllable in the vertical direction. The microscope (right) was able to focus on the channel by adjusting the lift. The glass channel is beneath the objective of the microscope. **b** Sketch of the syringe. The glass channel was glued to the syringe tip using a thick silicone glue.

6.3.2 Micro-PIV set-up

For flowcontrol, the experiment involved a syringe pump from Harvard Apparatus (PHD 2000 Infuse/Withdraw) with a 10 μl Hamilton Gastight syringe (1701 series, LT) attached to it. Figure 6.3a shows a picture of the set-up. De-ionized water was used as working fluid, seeded with 0.08% (per volume) fluorescent polymer microspheres (Duke Scientific Corp.). The particle diameter was 1 μm with a density of 1005 kg m^{-3} and thus a specific gravity of 1.01. Particles loaded with a fluorescent dye with peak excitation wavelength $\lambda_{ex} = 540$ nm and peak emission wavelength $\lambda_{em} = 620$ nm were chosen for the experiment.

Imaging was performed via an up-right BX51 microscope from Olympus equipped with a 20-fold planachromat objective lens with NA of 0.40 and an appropriate fluorescence filter cube. The flow field was illuminated by a continuous Hg-arc lamp. Images of the flow field were recorded using a Kodak MEGAPLUS ES/1.0 10bit CCD camera. This camera has an active 1008×1018 pixel array

with 9 μm square pixels, and a capability of grabbing images at a framerate of 30 frames per second. The images were transferred to a PC via a RoadRunner framegrabber from BitFlow. A free software for particle image velocimetry called PIV *Sleuth* (Christensen *et al.*, University of Illinois) was used to compute the vector fields from the local displacement of tracer particles between two frames.

6.3.3   Experimental procedure

Droplet velocity and creation

The liquid velocities employed were as low as 0.2 millimeters per second. At these flow rates, interfacial forces dominate by two orders of magnitude over gravity and by five orders of magnitude over viscous ones.

We use air as the pumping medium for the liquid droplet. This may cause non-constant droplet velocity depending on the dead volume. For this case the dead volume is the gas volume between the syringe piston and the water droplet. Figure 6.3b shows a sketch of the experimental set-up. When moving the liquid droplet, one moves the syringe piston in order to travel the gas volume. Air, being a compressible gas, can thus change its volume instead of keeping it constant. In order to transfer the liquid droplet 1 millimeter in the channel, the piston must occupy a volume of 1×10^{-12} m^{-3}. If this volume is very small relative to the total amount of dead volume, the result of a piston movement can be that the gas pressure increases and the droplet resides its initial position. Such a pressure build-up can also cause a lag in the movement of the drop. A severe prerequisite for a gas driven system is therefore to limit the dead volume to a minimum. Partially wetted walls may also contribute to discontinuous drop movement, by unbalancing the pressure drop across the drop due to different surface tension forces at the two meniscuses of the droplet. The dead volume in this system was approximately 2.5×10^{-9} m^{-3}, which did cause a measurable lag in the droplet movement. The precise lag of the droplets is dependent on surface impurities of the glass walls, but the small statistical pinning effects are not considered here. The droplets were created by injecting the liquid into the glass channel by the use of capillary forces.

Micro-PIV procedure

Droplet-flows are transient and require extraordinary processing. Several series of 190 images per series were obtained with a time delay of approximately 34 ms between each frame. The shutter speed of the camera was set to 6.36 ms. Hence, by using a continuous light source this equipment had a limitation concerning the flow rate of the droplets. For the flow rates employed here, the maximum particle size on a captured image due to exposure time was 2.3 μm, which is considered

neglectable for these measurements. Flow fields were obtained by reducing the flow to steady motion by subsequently moving the frame of interest in each image digitally. By this method the droplet was kept in the same position in each image. This is analogous to superposing a bulk velocity $-U_b$ to the interrogated vector field, but is more correct because the latter method does not involve investigations of the overlapping area at the droplet endings.

Vector fields were achieved by locally cross correlating the images with a spot size of 32×32 pixels and 50% overlap resulting in images with 25×15 and 14×15 velocity vectors for the two droplets presented here. Since the cameras field of view contained not only the desired particle intensities within the droplets, but also reflections from the gas-liquid meniscuses and from the glass channel walls, several erroneous velocity vectors had to be removed. These were eliminated manually within the PIV *Sleuth* software.

The measurement depth of the micro-PIV system is investigated by Mielnik *et al.* (2005) and for these experiments all the experimental data is assumed to be depth-averaged over 60 μm of the total channel depth.

6.3.4 Simulations

The simulations were performed using the flow solver CFX 5.7 (ANSYS Inc.). Discrete liquid droplets were recreated by constructing a two-dimensional triangular grid enclosed by walls. The CFD models had approximately 7000 number of cells. The fluidic properties used were, as for water, $\rho = 1000$ kg m^{-3} and $\mu = 10^{-3}$ kg m^{-1}s^{-1} for density and kinematic viscosity, respectively. The simulations are conducted by translating the vertical walls at a velocity V_d, while the left and right walls are stationary in this reference frame.

6.4 Results and discussion

6.4.1 Large droplet - $\beta = 2.6$

Figure 6.4 shows droplet with an aspect ratio of $\beta = 2.6$. The aspect ratio β is calculated using the smallest distance in the concave shape as L. The top image is an inverted fluorescence image representing the first of two images to be cross-correlated. The two below are the corresponding vector field (left) and the contour lines for the streamfunction (right) for the droplet. The fluorescence image did include a reflection in the right meniscus and from the glass channel at the lower wall. This can be seen in the top image in Figure 6.4, where there is a black area at the right meniscus and a white area close to the bottom wall. This lack of information gave spurious velocity vectors in the image left below in Figure 6.4,

and was manually removed in the PIV *Sleuth* software. The velocity vector field and the streamlines of the $\beta = 2.6$ droplet do however prove resemblance with the analytical solution described by Duda & Vrentas (1971), even though their work does not involve a concave shaped droplet.
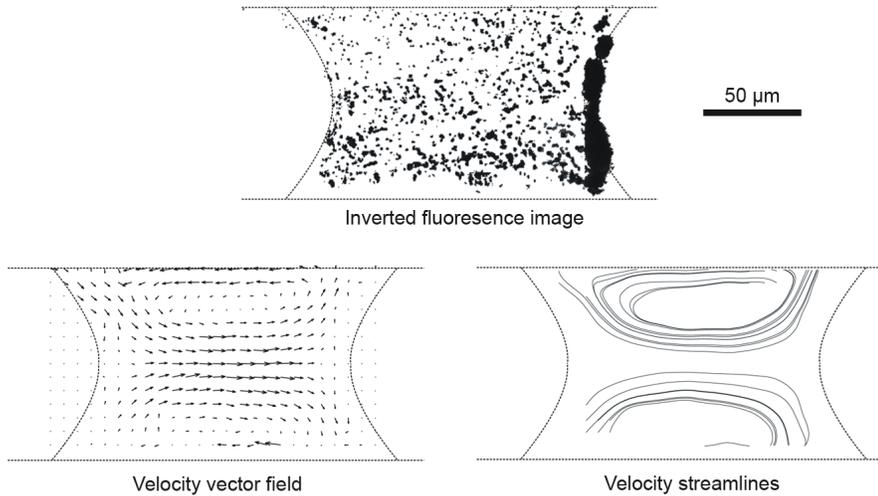
Figure 6.4: Experiment results of droplets with aspect ratio of $\beta = 2.6$. A representative fluorescence image (top) is showing a liquid droplet. The corresponding velocity vector field (bottom left) and streamline contours (bottom right) from micro-PIV measurements of a droplet travelling at a velocity of 0.078 $\mathrm{mm\ s^{-1}}$, equivalent to a Reynolds number of $Re = 0.0078$.

To get a better impression about the flow profile inside the microchannel, simulations were carried out. Figure 6.5 displays simulations of a droplet with aspect ratio of $\beta = 2.6$. The left image shows the velocity vector field and the right image shows the corresponding streamline contours. The results from Figure 6.4 and Figure 6.5 show that despite the lack of information in the experimental data, the patterns in both simulation and experiment show the same qualitative behaviour with a symmetrical two-cell recirculation area. The simulations also show an overall symmetry with respect to the channel centre.

Figure 6.6 depicts the velocity profiles of the vertical symmetry line of the experiment (dashed dot line, open squares), the simulation (solid line) and the parallel plate theory (dashed line). The experimental values are created using an averaged velocity profile from the five vertical velocity profiles in the middle of the droplet. The lowest y value is averaged over two values, due to the data errors cause by refection. The simulations and the experimental results show a resemblance in the middle of the droplet, in contrast to the results close to the

Velocity vector field   Velocity streamlines
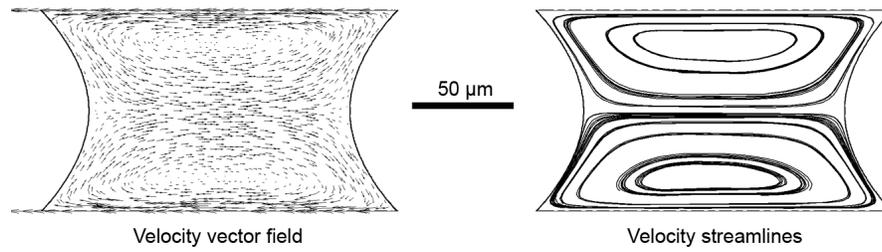
Figure 6.5: Simulations of droplet with aspect ratio of $\beta = 2.6$. The model is created with the same wetting angle and dimensions as the droplet in the experiments. A velocity vector field (left) and the corresponding streamline contours (right).
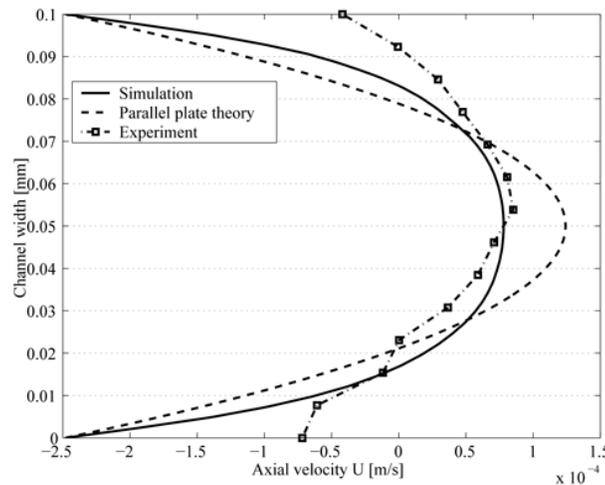
Figure 6.6: Velocity profiles for the vertical symmetry line in a droplet with aspect ratio of $\beta = 2.6$. The solid line is representing the simulations, and the open squares represent the experiments. The parallel plate theory (dashed line) is presented for comparison.

walls. This can be explained by the experimental data close to the walls are hard to recreate due to the rather low resolution of spot size ($14.4 \times 14.4 \ \mu m^2$), compared to the high resolution of the simulation grid (approximately $0.5 \times 0.5 \ \mu m^2$). The results from droplet $\beta = 2.6$ demonstrates a vague similarity to the parallel plate theory. The simplifications made for the parallel plate theory are more correct as the droplets aspect ratio increases. To verify this, a simulation of a droplet with aspect ratio $\beta = 5$ was conducted. Figure 6.7 presents the velocity profile from the simulation and the parallel plate theory of the latter droplet. As expected these velocity profiles show a great match.
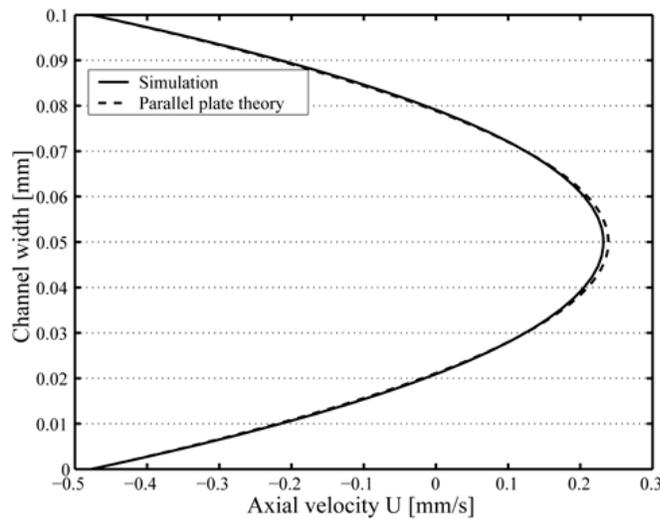
Figure 6.7: Velocity profiles for the vertical symmetry line in a droplet with aspect ratio of $\beta = 5$. The solid line is representing the simulations, and the dashed line represents the parallel plate theory.

6.4.2 Small droplet - $\beta = 1$

Figure 6.8 shows experimental results of a droplet with aspect ratio of $\beta = 1$. The top image is an inverted fluorescence image representing the first of two images to be cross-correlated. The two below are the corresponding vector field (left) and the contour lines for the streamfunction (right) for the droplet. As the two latter images reveals, the amount of particles inside the droplet was not sufficient enough to bestow the experimental data the quantity of information to create a proper flow field. This proved to be impossible under the conditions in this work. The smallest droplets did not include a sufficient number of particles, as some of them most likely were absorbed into the meniscuses of droplet. The velocity vector field and the streamlines of the $\beta = 1$ droplet do however prove resemblance with the analytical solution described by Duda & Vrentas (1971), despite the lack of information in the experimental data.

Figure 6.9 displays CFD simulations of a droplet with aspect ratio of $\beta = 1$. The left image shows the velocity vector field and the right image shows the corresponding streamline contours. The simulations show the expected qualitative behaviour with a symmetrical two-cell recirculation area with respect to the channel centre.

Figure 6.10 depicts the velocity profiles of the vertical symmetry line of the experiment (dashed dot line, open squares), the simulation (solid line) and the
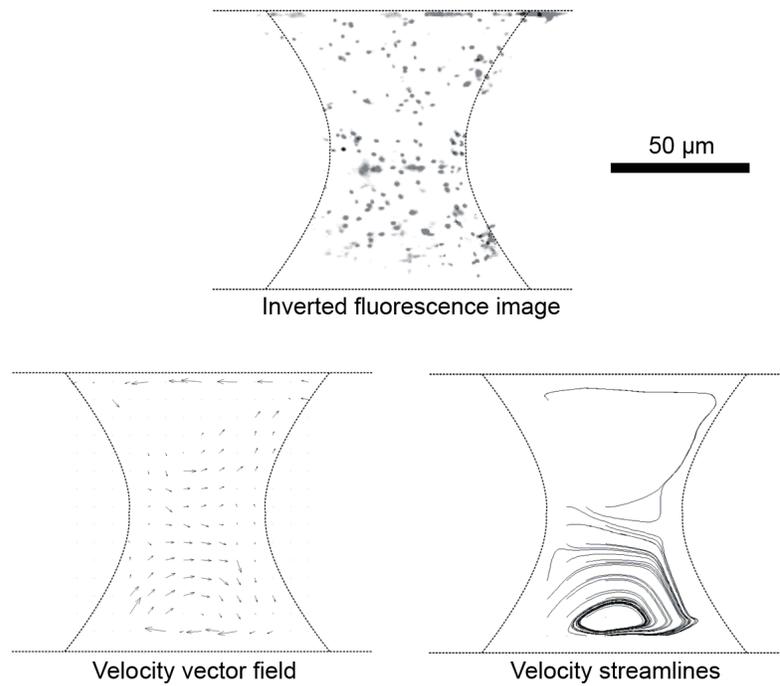
Figure 6.8: Experiment results of droplets with aspect ratio of $\beta = 1$. A representative fluorescence image (top) is showing a liquid droplet. The corresponding velocity vector field (bottom left) and streamline contours (bottom right) from micro-PIV measurements of a droplet travelling at a velocity of 0.2 mm s^{-1}, equivalent to a Reynolds number of $Re = 0.02$.

parallel plate theory (dashed line). The experimental values are created using an averaged velocity profile from the three vertical velocity profiles in the middle of the plug. For viewing purposes, the data forming the profile below the horizontal symmetry line is mirrored above horizontal symmetry line, because the information in the experimental data was not sufficient enough to produce a complete velocity profile. These simulations and the experimental results show a remarkable resemblance in the middle of the droplet, and again weak resemblance in the areas close to the walls, due to the low resolution of the experimental data. These two velocity profiles demonstrate the same trend in the mid area of the droplet, the velocity is decreasing. This shows signs of the prediction of Duda & Vrentas (1971) of a four-cell recirculation zone for droplets with aspect ratio of $\beta < 0.5$, as this droplet demonstrated a velocity profile with a dip in the mid area. It is assumed that this decreasing trend of velocity will at a lower aspect ratio β create a four-cell recirculation pattern as illustrated in Figure 6.2. The parallel plate theory is displayed for comparison and does not show any of the

Velocity vector field   50 µm   Velocity streamlines
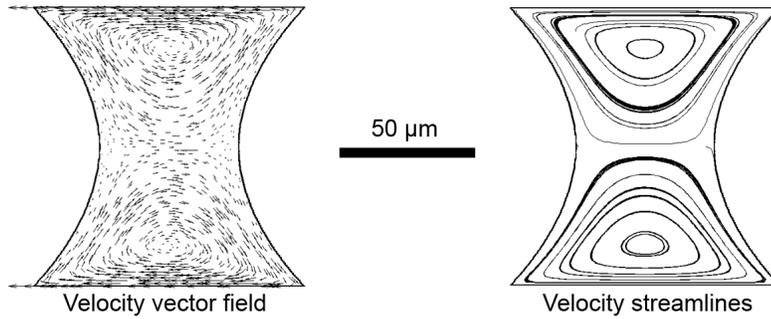
Figure 6.9: Simulations of droplets with aspect ratio of $\beta = 1$. The model is created with the same wetting angle and dimensions as the droplet in the experiments. A velocity vector field (left) and the corresponding streamline contours (right).
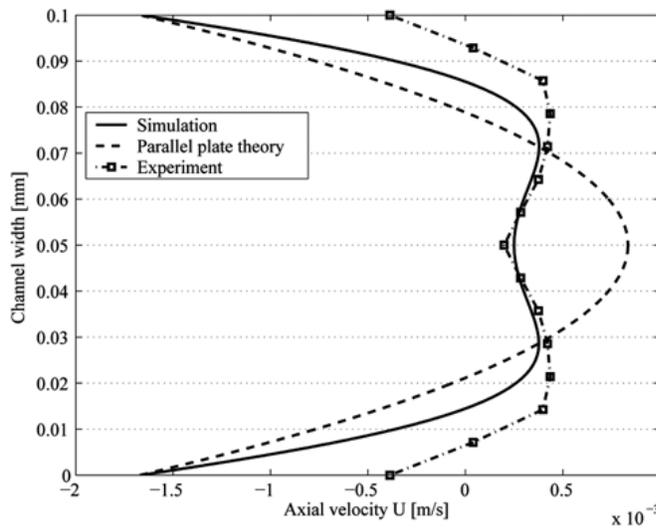

Figure 6.10: Velocity profiles for the vertical symmetry line in a droplet with aspect ratio of $\beta = 1$. The solid line is representing the simulations, and the open squares represent the experiments. The parallel plate theory (dashed line) is presented for comparison.

same trends as the experiment or the simulation due to the simplifications made.

6.4.3   Influence of recirculation pattern on mixing

The recirculation motion and the stagnation points found in the streamline contours for both droplets are consistent with both the analytical solution of Duda & Vrentas (1971) and the predictions of Taylor (1961). Hence, this shows that a

mixing improvement would be expected for droplet flow. As an example one can consider the microchannel used in the experiments. The bottom of the channel is covered with a dried reactant with the purpose of mixing into a sample droplet, which in this case is water. The reactant consists of spherical particles with diameter of 100 nm which have a diffusion constant in room temperature water of $D = 8.58 \times 10^{-12}$ m^2 s^{-1}. By using Eq. 6.2, the time particle spends to diffuse halfway through the channel height (50 μm) is $t_d = 2.4$ minutes. In contrast, by only considering convective mixing, a droplet with the size of $\beta = 1$ which travels with a velocity of 0.2 mm s^{-1}, can transport the same particle to its middle in an estimated time of 0.5 s. The particle utilizes the recirculation zones and travels along the peripheral streamlines inside the droplet. This situation brings a vast improvement of the mixing time. The realistic situation will be a combination of the two mixing techniques. In order to utilize the droplet's recirculation pattern in mixing in the diagnostic system we plan to move the droplet in oscillating motion above the dried reactant with a certain velocity and frequency. These parameters have to be investigated carefully and adjusted to the diffusion constant of the reactant. Future work will investigate this effect.

6.5   Conclusions

Microsystem solutions for medical analysis, diagnostics, microreactors or drug discovery are crucially dependent on reagent mixing. Due to size, fluidics in microchannels are usually dominated by laminar flows of low Reynolds number (Re) and thus mixing becomes a serious challenge, because only molecular diffusion is predominant on these length scales. In order to mix two miscible reagents in a microsystem, this implies a need for a large contact area between the two reagents. Such a continuous flow system requires long channel distances ($\gg$ 1 cm) which is generally not preferred in a microsystem. Droplet-based microfluidics introduce a number of advantages. The advantages regard utilizing the recirculation streamlines inside the droplet to enhance mixing and also the isolation of a precise volume of the two components to be mixed.

We present a method of visualizing the recirculating pattern of liquid within hydrodynamic droplet-based flow in a straight microchannel. The flowfields inside two different sized droplets ($\beta = 1$ and $\beta = 2.6$) were studied by the means of micro-PIV measurements and CFD simulations for Reynolds numbers of 0.02 and 0.0078, respectively. The analysis proved recirculation motion and stagnation points in the streamline contours as predicted by Taylor (1961). The smallest droplet approached the prediction of Duda & Vrentas (1971) of a four-cell recirculation zone for droplets with size of $\beta < 0.5$, as this droplet demonstrated a velocity profile with a dip in the mid area.

These investigations gave rise to a potential improvement in the mixing procedure, despite the low Reynolds number regime of the flow. For a situation concerning droplet-based fluidic devices with on-chip stored dried enzymes, this work proved that by utilizing the internal recirculation streamlines generated by the droplet movement, molecular diffusion can be combined with convective mixing. This results in a significant decrease of the mixing time.

The presented data indicates that droplet-based fluidics and on-chip dried reagents may serve as a feasible solution to a lab-on-a-chip system and should be investigated further.

Acknowledgements

References

Bau, H. H., Zhong, J. & Yi, M. 2001 A minute magneto hydro dynamic (MHD) mixer. *Sens. Actuators, B* **79**, 207–215.

Bringer, M. R., Gerdts, C. J., Song, H., Tice, J. D. & Ismagilov, R. F. 2004 Microfluidic systems for chemical kinetics that rely on chaotic mixing in droplets. *Philos. Trans. R. Soc. London, Ser. A* **362** (1818), 1087–1104.

Burns, J. R. & Ramshaw, C. 2001 The intensification of rapid reactions in multiphase systems using slug flow in capillaries. *Lab on a Chip* **1**, 10–15.

Burns, M. A., Johnson, B. N., Brahmasandra, S. N., Handique, K., Webster, J. R., Krishnan, M., Sammarco, T. S., Man, P. M., Jones, D., Heldsinger, D., Mastrangelo, C. H. & Burke, D. T. 1998 An integrated nanoliter DNA analysis device. *Science* **282** (5388), 484–487.

Drese, K. S., Sörensen, O., Solli, L. A. & Gulliksen, A. 2003 Design and realization of a lab-on-a-chip system for multiple real-time detection of nucleic acid sequence-based amplification (NASBA). In *smallTalk 2003, San Jose, CA, USA*.

Duda, J. L. & Vrentas, J. S. 1971 Steady flow in the region of closed streamlines in a cylindrical cavity. *Journal of Fluid Mechanics* **45**, 247–260.

Fowler, J., Moon, H. & Kim, C.-J. 2002 Enhancement of mixing by droplet-based microfluidics. In *Proc. of the IEEE Micro Electro Mechanical Systems Workshop (Las Vegas, NV, USA, Jan 2002)*, pp. 97–100.

Garcia, E., Kirkham, J. R., Hatch, A. V., Hawkins, K. R. & Yager, P. 2004 Controlled microfluidic reconstitution of functional protein from an anhydrous storage depot. *Lab on a Chip* **4** (1), 78–82.

Gulliksen, A., Solli, L. A., Drese, K. S., Sörensen, O., Karlsen, F., Rogne, H., Hovig, E. & Sirevåg, R. 2005 Parallel nanoliter detection of cancer markers using polymer microchips. *Lab on a Chip* **5** (4), 416–420.

Günther, A., Khan, S. A., Thalmann, M., Trachsel, F. & Jensen, K. F. 2004 Transport and reaction in microscale segmented gas-liquid flow. *Lab on a Chip* **4** (4), 278–286.

Handique, K. & Burns, M. A. 2001 Mathematical modeling of drop mixing in a slit-type microchannel. *Journal of Micromechanics and Microengineering* **11** (5), 548–554.

HONG, C. C., CHOI, J. W. & AHN, C. H. 2001 A novel in-plane passive micromixer using coanda effect. In *Proc. of the µTAS Symposium (µTAS 2001), Monterey, CA, USA, Oct 2001*, pp. 31–33.

KATOPODES, F. V., DAVIS, A. M. J. & STONE, H. A. 2000 Piston flow in a two-dimensional channel. *Physics of Fluids* **12**, 1240–1243.

LAMMERTINK, R. G. H., SCHLAUTMANN, S., BESSELINK, G. A. J. & SCHASFOORT, R. B. M. 2004 Recirculation of nanoliter volumes within microfluidic channels. *Analytical Chemistry* **76** (11), 3018–3022.

LIU, R. H., STREMLER, M. A., SHARP, K. V., OLSEN, M. G., SANTIAGO, J. G., ADRIAN, R. J., AREF, H. & BEEBE, D. J. 2000 Passive mixing in a three-dimensional serpentine microchannel. *J. Microelectromech. Syst.* **9**, 190–197.

LU, L.-H., RYU, K. S. & LIU, C. 2001 A novel microstirrer and arrays for microfluidic mixing. In *Proc. of the µTAS Symposium (µTAS 2001), Monterey, CA, USA, Oct 2001*, pp. 28–30.

MIELNIK, M. M., EKATPURE, R. P., SÆTRAN, L. R. & SCHÖNFELD, F. 2005 Sinusoidal crossflow microfiltration device - experimental and computational flowfield analysis. *Lab on a chip* **5** (8), 897–903.

ODDY, M. H., SANTIAGO, J. G. & MIKKELSEN, J. C. 2001 Electrokinetic stability micromixing. *Anal. Chem.* pp. 5822–5832.

SAMMARCO, T. S. & BURNS, M. A. 1999 Thermocaplliary pumping of discrete drops in microfabricated analysis devices. *AIChE Journal* **45** (2), 350–366.

SCHWESINGER, N., FRANK, T. & WURMUS, H. 1996 A modular microfluid system with an integrated micromixer. *Journal of Micromechanics and Microengineering* **6**, 99–102.

STROOCK, A. D., DERTINGER, S. K. W., AJDARI, A., MEZIĆ, I., STONE, H. A. & WHITESIDES, G. M. 2002 Chaotic mixer for microchannels. *Science* **295**, 647–651.

TAYLOR, G. I. 1961 Deposition of a viscous fluid on the wall of a tube. *Journal of Fluid Mechanics* **10**, 161–165.

TÜDŐS, A. J., BESSELINK, G. A. J. & SCHASFOORT, R. B. M. 2001 Trends in miniaturized total analysis systems for point-of-care testing in clinical chemistry. *Lab on A Chip* **1** (2), 83–95.

Veenstra, T. T., Lammertink, T. S. J., Elwenspoek, M. C. & Van den Berg, A. 1999 Characterisation method for a new diffusion mixer applicable in micro flow injection analysis systems. *Journal of Micromechanics and Microengineering* **9**, 199–202.

Verpoorte, E. 2002 Microfluidic chips for clinical and forensic analysis. *Electrophoresis* **23**, 677–712.

Yang, Z., Matsumoto, S., Goto, H., Matsumoto, M. & Maeda, R. 2001 Ultrasonic micromixer for microfluidic systems. *Sensors and Actuators A-Physical* **93** (3), 266–272.

Chapter 7

Numerical and experimental investigation of hydrodynamically focused sheets

Lars A. Solli[1,2], Lars R. Sætran[1] & Michal M. Mielnik[3]

[1]Dept. of Energy and Process Engineering, Norwegian University of Science and Technology, Kolbjørn Hejes vei 1B, 7491 Trondheim, Norway
[2]NorChip AS, Industriveien 8, 3490 Klokkarstua, Norway
[3]Dept. of Microsystems, SINTEF ICT, Forskningsveien 1, 0314 Oslo, Norway

A numerical study of hydrodynamic focusing in microchannels is presented and compared with experimental results. The emphasis is on the characterization of the focused sheet in terms of its shape and position. The sheet defines the measurement plane when using selective seeding, a novel seeding method for micro-PIV. It is found that the sheet is considerably deformed at high flow velocities and large side stream ratios, making the technique applicable to micro-PIV in the velocity ranges below ~10 mm/s. Using lower angles of the side stream inlet channels, the sheet deformation is substantially reduced, extending the velocity range in which selectively seeded micro-PIV is feasible.

7.1   Introduction

Hydrodynamic focusing is a technique that allows a liquid stream in a channel to be sheathed in a buffer liquid. The method has been widely used in early fluid mechanical studies in the late 19th century, to e.g. observe transition and turbulence (Reynolds, 1883). However, the method also provides a means for transporting particles of interest using the sheathed liquid as a carrier medium.

This approach was first introduced some 50 years later, by Moldavan (1934) and subsequently Crosland-Taylor (1953) as preparatory to electronic counting of red blood cells. It affords the ability to position small quantities of particles with high precision in two dimensions as well as to isolate the particles from channel wall surfaces without the sedimentation effect of gravity. Although work has given birth to several derivations of this approach over the years, the basic principle is still similar, and the most commonly used in flow cytometry (Robinson, 2004) systems today.

In microfluidics, hydrodynamic focusing has been involved and integrated in a great deal of applications such as micro-chip flow cytometers (Miyake *et al.* (1991), Sobek *et al.* (1994)) Coulter particle counter (Larsen *et al.*, 1997), production of polymeric microfibers (Ju *et al.*, 2005), measurement of diffusion coefficients (Munson *et al.*, 2005), generation of monodisperse droplets (Xu & Nakajima, 2004), microreactors (Jahn *et al.*, 2004), flow switching (Lee *et al.*, 2001), mixing in continuous flow systems (Knight *et al.*, 1998) and also mixing in combination with time-interleaved segmentation (Nguyen & Huang, 2005).

Microscale particle image velocimetry (micro-PIV) (Santiago *et al.*, 1998) is a flow measurement technique permitting detailed investigation of microscale flows. The method involves flow seeded with particles as a tool for visualization. Recently, hydrodynamic focusing has been applied in combination with micro-PIV (Mielnik & Sætran, 2006). In this method (Selectively Seeded micro-PIV, SeS-PIV), a hydrodynamically focused stream containing tracer particles defines the measurement plane of the system. Thus, observation of a thin plane within the flow containing the particles is possible, permitting improvement of the depth-wise resolution. Detailed knowledge of the shape and position of the focused sheet is of crucial importance to the SeS-PIV technique, as this sheet defines the measurement plane. Deformations of the sheet may cause incorrect PIV measurements.

This work presents both numerical and experimental investigations of hydrodynamic focusing in a microchannel intersection. The characteristics of the focused sheet are investigated in terms of its shape and position. The results show that the volumetric flow rate ratio of the buffer liquids, the total mean velocity and the angle of the buffer inlet channels influence the shape of the sheet. The computations are validated by comparison to experimental results, showing good agreement. The work presented herein brings forth essential information with respect to the measurement plane in SeS-PIV, by giving a quantitative description of hydrodynamic focusing.

7.2 Background

7.2.1 Principle of SeS-PIV

In a conventional micro-PIV system the commonly applied seeding method is identical to that in macroscopic PIV, namely bulk seeding, with tracer particles evenly distributed throughout the volume of the carrier liquid. In macroscopic PIV, the measurement plane is defined by laser sheet illuminating a plane within the flow. In micro-PIV, laser sheet illumination is not feasible due to the small dimensions of the channels. Instead, the entire volume of flow (and all particles residing inside it) is illuminated. The measurement plane is then mainly defined by the optical characteristics of the imaging system and the particle size. The particles residing outside of the optical measurement plane are also illuminated and generate background noise, corrupting the quality of the particle images. To ensure acceptable signal-to-noise ratio levels (Meinhart *et al.*, 2000), a reduced particle concentration with increasing channel depth is required. To compensate for the insufficient particle image density, average correlation is commonly employed (Wereley *et al.*, 2002). As a consequence, measurement of instantaneous velocity fields on the microscale is a challenging task, and with a few exceptions (Shinohara *et al.*, 2004) the reported velocity data typically represents a temporal average of the flow field.

The basic idea behind selective seeding is to generate a thin layer of seeded liquid sheathed in an otherwise particle-free buffer liquid. The concept is shown schematically in Fig. 7.1, where δ_{PS} is the particle sheet thickness, and δ_Z is the optical measurement depth of the micro-PIV system (Meinhart *et al.*, 2000). When a sufficiently thin particle sheet is generated, so that $\delta_{PS} < \delta_Z$, the particle sheet unambiguously defines the thickness and position of the measurement plane, regardless of the optical set-up. This is analogous to the functionality of a laser sheet in macroscale PIV. The maximum depth-wise resolution of the system is solely limited by the particle diameter, d_p, represented by the case of a monolayered particle sheet ($\delta_{PS} = d_p$) in Fig. 7.1c.

7.2.2 Principle of hydrodynamic focusing

The principle of hydrodynamic focusing is presented in Figure 7.2. At a four-channel intersection, the stream of interest containing the seeded particles, is focused and sheathed downstream by two side streams containing buffer liquids. Q_A, Q_B and Q_C represent the volumetric flow rates of the three merging streams, whereas δ_{tot} represents the sheet thickness. At low flow velocities, δ_{tot} can be approximated from a one-dimensional (1D) approach of mass balance:
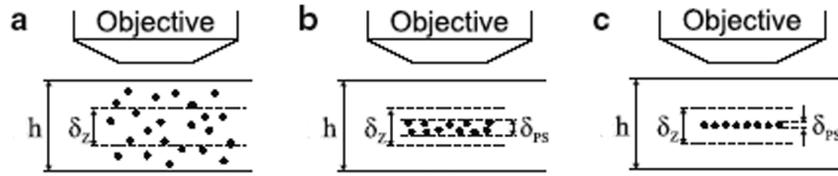
Figure 7.1: Schematic illustration of selective seeding. **a** Bulk seeded flow. **b** $\delta_{PS} < \delta_Z$; the particle sheet defines the measurement plane of the system. **c** Limiting case of a monolayered particle sheet.
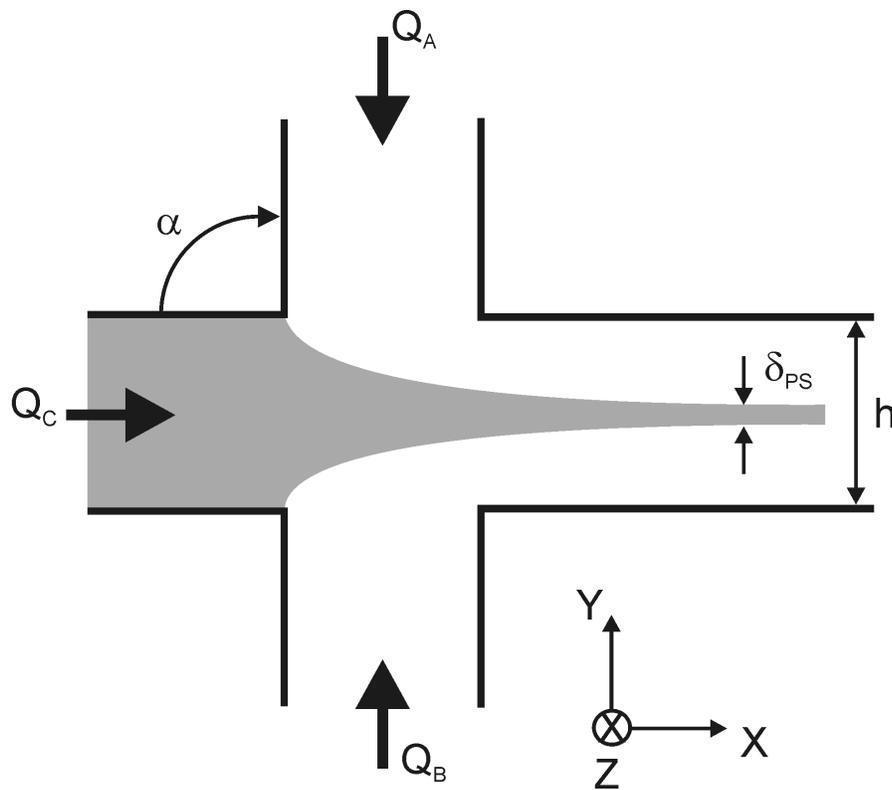
Figure 7.2: Schematic illustration of the hydrodynamic focusing device. The sketch shows the symmetric case, where $Q_A = Q_B$, and the focused sheet resides in the centre of the outlet channel.

140

$$\frac{\delta_{tot}}{h} = \frac{Q_C}{Q_A + Q_B + Q_C} = \frac{Q_C}{Q_{tot}}, \tag{7.1}$$

where h is the height of the channel and Q_{tot} is the total flow rate exiting the intersection. Figure 7.2 displays a symmetrical case, where $Q_A = Q_B$ and the focused sheet resides in the centre of the outlet channel. The position of the sheet in the y-direction can be controlled by altering the ratio of the side stream flow rates, i.e. Q_B/Q_A.

7.3   Methods and experiments

7.3.1   Numerical simulation

The simulations were conducted using the commercial CFX-10 software (version 10.0 ANSYS CFX Inc.). The flow was modelled using the incompressible Navier-Stokes equations, with continuity and momentum given by:

$$\nabla \cdot \boldsymbol{V} = 0 \tag{7.2}$$

and

$$\rho \frac{D\boldsymbol{V}}{Dt} = \rho \left(\frac{\partial \boldsymbol{V}}{\partial t} + \left(\boldsymbol{V} \cdot \nabla \right) \boldsymbol{V} \right) = -\nabla p + \mu \nabla^2 \boldsymbol{V}, \tag{7.3}$$

respectively. Here, p is the pressure, ρ is the density, $\boldsymbol{V} = (u, v, w)$ is the velocity vector and μ is the dynamic viscosity of the fluid. A steady-state flow is assumed for all cases.

Grid generation was accomplished using the CFX-Mesh software. CFX-10 employs an advanced coupled algebraic multigrid method that solves the hydrodynamic equations (for u, v, w and p) as a single system. The solution approach uses fully implicit discretization of a pressure-based finite volume method. The default advection scheme "high resolution" was used for all cases. This is a bounded, second-order upwind scheme based on that of Barth & Jesperson (1989). It ensures high accuracy and good convergence while still producing physical results that are free of spurious spatial overshoots and undershoots in the solution variables.

The schematic structure of the four channel intersection illustrated in Fig. 7.2 constitutes the model used in the simulations. The cross section of the structure is 1040×800 $(h \times w)$ μm^2, as the height and width, respectively. The length of all the inlets is 1.5 times the height of the channel and the length of the outlet is twice the channel height. Preliminary investigations proved that this length was adequate in terms of ensuring fully developed flow. The use of symmetry in the xy-plane at

141

z = 0 (reference to the coordinate system in Fig. 7.2) permitted reduction of the computational domain. Grids consisting of unstructured tetragonal meshes with approximately 265k–460k nodes (1499k–2624k elements), depending on the inlet ratios, were used in the simulations. A preliminary grid convergence study verified that the solution was grid independent. In order to produce accurate results the mesh must consists of 7–8 nodes between the fluid layers. The inlet boundary conditions were specified by the desired mass flow rates, and the outlet boundary condition was fixed at a reference pressure of 0 atm. Both the seeded liquid and the buffer are modelled as two immiscible water-based fluids. The side-to-centre flow rate ratio, $(Q_A + Q_B)/Q_C$ was kept constant at 19:1. The computations were performed on a Pentium 4 PC (3.2 MHz CPU, 2 GB RAM, Windows XP) and a Pentium 4 PC (3.6 MHz CPU, 1 GB RAM, Linux). The post-processing results were visualized by defining the multiphase flow variable "fluid.Volume Fraction" as 0.5.

7.3.2 Experiments

To investigate the characteristics of hydrodynamic focusing experimentally, Confocal Laser Scanning Microscopy (CLSM) was used. CLSM is a microscopy technique capable of delivering images of high depth-wise resolution (Park *et al.*, 2004).

The set-up includes a Carl Zeiss CLSM 510 microscope equipped with a CCD camera (8 bit dynamic range), Plan-Neofluar 20×/0.5l and Plan-Neofluar 10×/0.3 objectives and HeNe 543 nm laser from LASOS lasertechnik as a light source.

Channels for the experiment were manufactured by a micromilling technique in polymethyl methacrylate (PMMA) and thermally bonded with a predrilled cover slip. The cross sections of investigated channels were 1040×800 ($h \times w$) μm^2.

For flow control, the experiment involved a syringe pump from Harvard Apparatus (PHD 2000 Infuse/Withdraw) with separate syringes for the seeded and the buffer liquids. The tube from the syringe containing the buffer liquid was split into parallel tubing connected to the side flow channels. In this manner, the ratio Q_B/Q_A could be easily controlled by varying the flow resistance in inlet channel A, without influencing the overall flow rate of the system. The pump maintained constant side-to-centre flow ratio at 19:1. The flow rate was measured by a rotameter on the tubing connected to channel B.

Deionized water labeled with a fluorescent dye (Alexia Fluor 546 from Molecular Probes) was used as the working fluid in the central inlet (channel C in Fig. 7.2). Pure deionized water was injected into the two side channels (A and B in Fig. 7.2).

142

7.4 Results and discussion

A typical post-processed result of a numerical simulation of the development of an asymmetric hydrodynamically focused sheet is displayed in Fig. 7.3. In this case, the side stream ratio is $Q_B/Q_A = 7$ and the mean velocity is $V = 15$ mm/s, where $V = Q_{tot}/hw$. As Fig. 7.3 reveals, the asymmetric side stream ratio displaces the sheet from the centre of the channel and induces a deflection in the y-direction. The pressure drop in all cases exhibited a linear shape at a distance of $\sim$0.8 mm downstream the four-channel intersection, confirming sufficient length of the outlet channel to achieve fully developed flow.
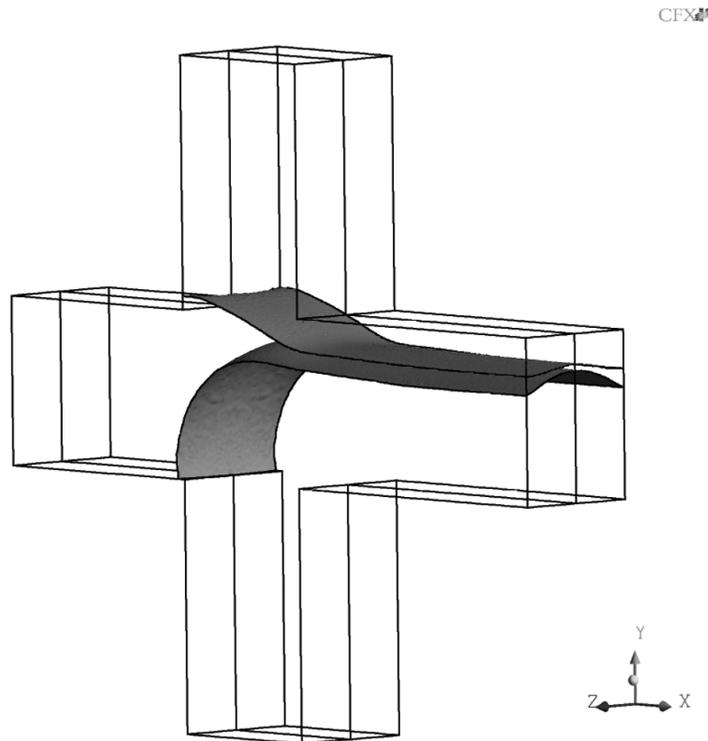
Figure 7.3: Post-processed result of a simulation of a hydrodynamically focused sheet at side stream ratio $Q_B/Q_A = 7$ and a mean downstream velocity of $V = 15$ mm/s.

Hydrodynamic focusing was investigated in the velocity range of $V = 1$–15 mm/s and the side stream ratios from $Q_B/Q_A = 1$ (symmetrical case) to $Q_B/Q_A = 15$.

CFD results of hydrodynamic focusing for $V = 15$ mm/s and various Q_B/Q_A is presented in Figure 7.4. The figure displays focused sheets in a cross section of

the outlet channel, viewed in a plane perpendicular to the x-axis. Corresponding experimental results are shown in Figure 7.5, however with a mean velocity of V = 13.5 mm/s. In the symmetrical case, i.e. Fig. 7.4a and Fig. 7.5a, the generated sheet exhibits a concave shape. For increasing Q_B/Q_A, the sheet moves away from the channel centre and becomes increasingly curved. Despite the minor difference in both the velocity and the side stream ratio in Figs. 7.4 and 7.5, the computational and the experimental data exhibit similar qualitative features of the focused sheet.
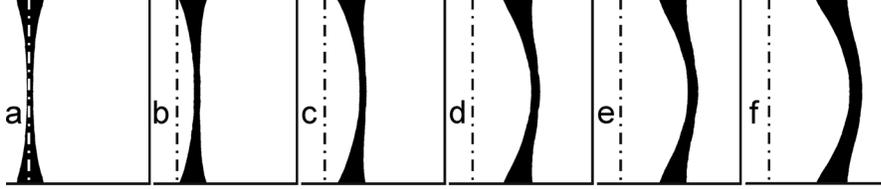
Figure 7.4: CFD results of hydrodynamically focused sheets at mean velocity of V = 15 mm/s, generated with side flow ratio of: **a** Q_B/Q_A = 1, **b** Q_B/Q_A = 1.5, **c** Q_B/Q_A = 2.3, **d** Q_B/Q_A = 5, **e** Q_B/Q_A = 7 and **f** Q_B/Q_A = 15.
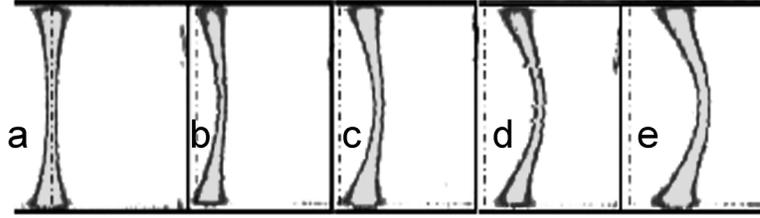

Figure 7.5: Experimental results (CLSM photos in false colours) of hydrodynamic focused sheets at mean downstream velocity of V = 13.5 mm/s, generated with side flow ratio of: **a** Q_B/Q_A = 1, **b** Q_B/Q_A = 1.73, **c** Q_B/Q_A = 2, **d** Q_B/Q_A = 3 and **e** Q_B/Q_A = 7.57.

In order to discuss the sheet characteristics, the sketch in Fig. 7.6 defines the relevant quantities. The figure illustrates a focused sheet in a cross section of the outlet channel at asymmetrical side stream conditions. The shape of the fluid layer exhibits both a bent nature and a thickness variation along the z-axis. The deflection of the layer, d, is quantified as the difference between the middle position of the sheet at the symmetry plane (Y_S) and the middle position at the wall (Y_W), i.e. $d = Y_S - Y_W$. The thickness variation is described by the ratio of the layer's thickness at the symmetry plane (δ_S) and at the wall (δ_W), namely δ_W/δ_S. The
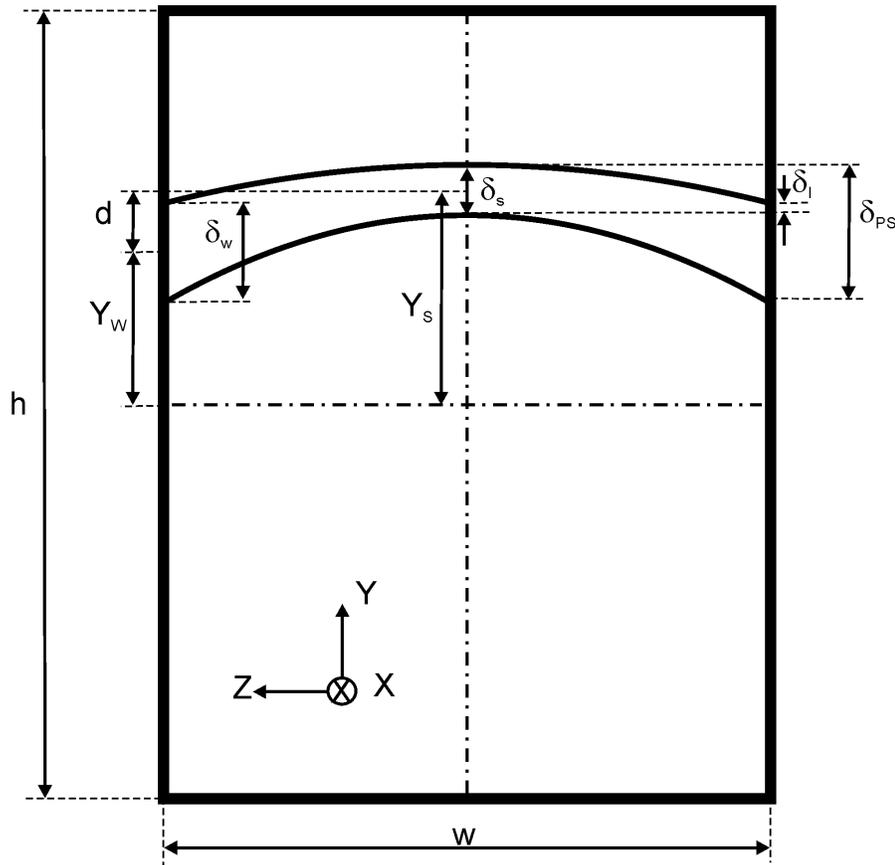
Figure 7.6: Sketch illustrating the cross section of the channel downstream of the four-channel intersection, defining the relevant quantities of the sheet.

difference between the layer's uppermost point at the wall and the lowest point at the symmetry line is quantified as the information depth, δ_I.

The displacement of the sheet from the centre of the channel (Y_S), was found to be highly dependent on the side stream ratio. Data from simulations and experiments are presented in Fig. 7.7. The side stream ratio is plotted against a normalized displacement, Y_S/h, for a wide range of velocities. The solid line is an approximated fit for all values, demonstrating an asymptotic trend towards the value of $Y_S/h = 1$, which represents the top wall of the channel. For a fixed side steam ratio, the CFD data suggest that the sheet displacement is nearly independent of the mean flow velocity. The experimental results have similar implications, although in this case the data exhibits more scatter. This may be due to uncertainties in the rotameter measurements.

Figure 7.8 shows the deflection, d, of focused sheets plotted against the
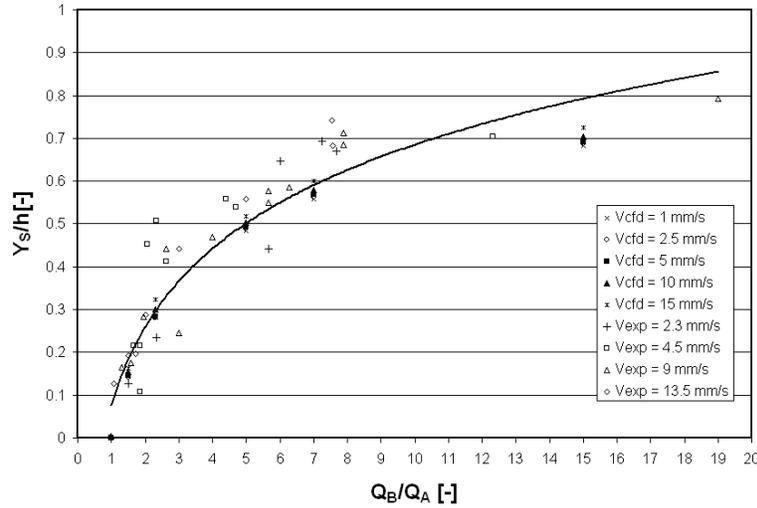
Figure 7.7: The normalized displacement of hydrodynamically focused sheets as a function of side stream ratio, for various values of the mean velocity. Both numerical and experimental data are shown. The solid line is a logarithmical fit for all velocities.

normalized displacement, Y_S/h. As seen previously in Figs. 7.4 and 7.5, the deflection increases with increasing sheet displacement. The graph shows that this growth is approximately linear. Furthermore, significant dependence between the mean velocity and the deflection can be seen, as the deflection becomes larger with increasing velocity. Good agreement between the numerical and experimental data is observed. Here, the experimental values are extracted directly from CLSM images, eliminating the previously mentioned uncertainties in rotameter measurements.

The thickness ratio δ_W/δ_S, is presented in Fig. 7.9. The figure demonstrates that this ratio is nearly independent of Q_B/Q_A at the lowest flow velocities (1–5 mm/s). This implies that the sheet thickness is approximately uniform across the span of the channel. At higher flow velocities, the thickness ratio decreases with increasing Q_B/Q_A. In the near symmetrical case ($Q_B/Q_A \approx 1$), the sheet thickness is significantly higher near channel walls than at channel centre. The shape of the focused sheet becomes increasingly concave (see also Figs. 7.4 and 7.5) as the velocity increases and may eventually break into two separate streams.

Both the deflection and the thickness ratio are important quantities in terms of accomplishment of the SeS-PIV technique. If the deflection value becomes sufficiently large, the information depth, δ_I, can become negative. In this case, parts of the focused sheet may reside outside the optical measurement depth, δ_Z

146
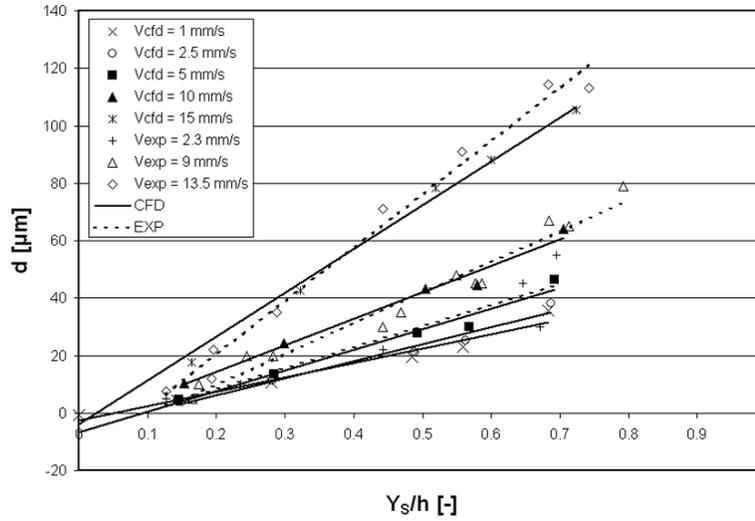
Figure 7.8: The deflection of hydrodynamically focused sheets as a function of normalized displacement, for various values of the mean velocity. Both numerical and exper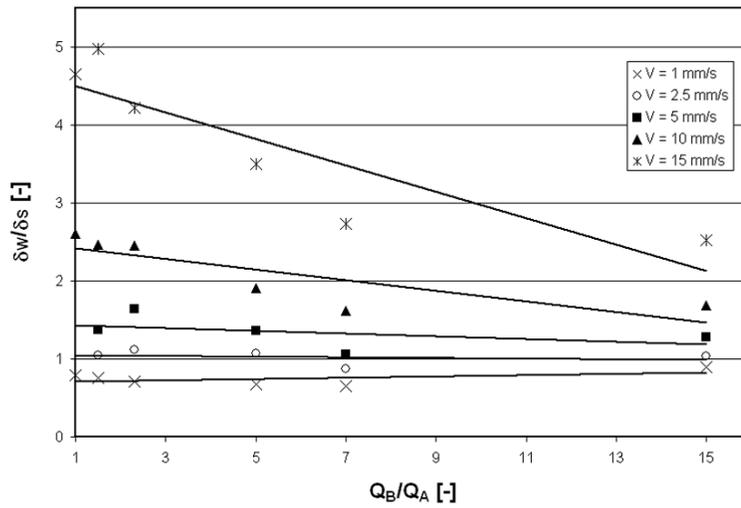imental data are shown. The solid lines and the dotted lines represent linear curve fits for the numerical and the experimental data, respectively.


Figure 7.9: The thickness ratio δ_W/δ_S, plotted against the side stream ratio Q_B/Q_A. The solid lines are linear curve fits for each velocity set. The graph contains numerical data only.

147

(see Fig. 7.1), causing loss of information in the particle image. High thickness ratio results in a non-uniform particle distribution in the PIV image, with high effective seeding concentration near the channel walls. This, in turn, may cause excessive background noise in the near-wall areas, corrupting the measurements.

The discussion above implies that, for high flow velocities and/or large sheet displacement (high Q_B/Q_A), the sheet will attain an undesirable shape. This poses a restriction on the range of application of the SeS-PIV technique, limiting it to velocities below $\sim$10 mm/s. This value depends on the characteristics of the specific micro-PIV set-up, i.e. the optical measurement depth, δ_Z. For very low particle sheet thickness, e.g. the limiting case of a monolayered particle sheet (see Fig. 7.1c), the measurement technique is vulnerable to a sheet deformation in the order of one particle diameter.

The sheet deformation is a direct consequence of the parabolic shape of the laminar velocity profiles of the merging side streams. The side stream flows have velocity components in the y- and z-direction, in contrast to the x- and y-directional components of the centre flow. The momentum imbalance is at its maximum at the centre of the channel, resulting in higher mass displacement in these areas than in the vicinity of the walls, causing the concave shape of the sheet. This effect is also evident in Fig. 7.3, where the lower part of the sheet in the intersection area reveals a spoon-like shape.

In order to further investigate the deflection and the thickness of the focused sheet, the inlet angle, α, of the side stream channels (see Fig. 7.2) was varied in numerical simulations. The shape of the focused sheet for $\alpha = $ 90°, 60°, 45° and 30° is shown in Fig. 7.10. All simulations were preformed at the flow velocity of $V = 15$ mm/s and $Q_B/Q_A = 15$. As can be seen from the figure, the sheet deflection and thickness ratio decrease with lower values of α. For the lowest angle, the sheet has nearly uniform thickness across the channel width and highly reduced deflection. This implies that such channel modification may enable the SeS-PIV technique at velocities exceeding the previously stated limit of $\sim$10 mm/s.
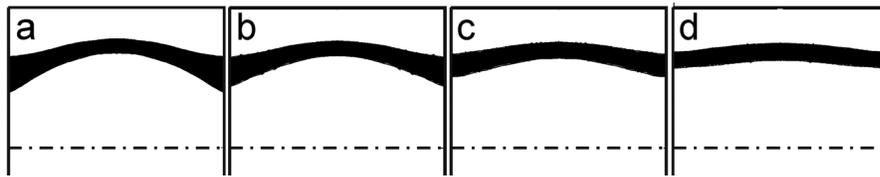
Figure 7.10: CFD results of hydrodynamic focused sheets at mean downstream velocity of $V = 15$ mm/s, generated with side flow ratio of $Q_B/Q_A = 15$. A device with a side flow attack angle of: **a** 90°, **b** 60°, **c** 45° and **d** 30°.

7.5 Conclusions

A numerical study of hydrodynamic focusing in micro channels is presented and compared with experimental results. In principle, hydrodynamic focusing involves a central stream (containing e.g. chemical or biological species of interest) which is squeezed into a thin layer within the flow. Recently, this technique has been applied to improve microscale particle image velocimetry (micro-PIV). The novel method relies on selective seeding of tracer particles in the central stream, to define the measurement plane of the system. The characteristics of the focused sheet were investigated with emphasis on the SeS-PIV technique.

For the channel size investigated here, it was found that for high flow velocities and high side stream ratios, the sheet deformation becomes too large to permit SeS-PIV measurements. However, for velocities below ∼10 mm/s, hydrodynamic focusing may be successfully applied in micro-PIV.

Substantial improvement of sheet characteristics can be achieved by lowering the angle of the buffer stream inlet channels. This increases the velocity range where SeS-PIV measurements are feasible.

Acknowledgements

References

BARTH, T. J. & JESPERSON, D. C. 1989 The design and application of upwind schemes on unstructured meshes. In *27th Aerospace and Science Meeting & Exhibit (Reno, 9-12 Jan. 1989) AIAA 89-0366*.

CROSLAND-TAYLOR, P. J. 1953 A device for counting small particles suspended in a fluid through a tube. *Nature* **17**, 37–38.

JAHN, A., VREELAND, W. N., GAITAN, M. & LOCASCIO, L. E. 2004 Controlled vesicle self-assembly in microfluidic channels with hydrodynamic focusing. *J.Am.Chem.Soc.* **126** (9), 2674–2675.

JU, J. I., OH, H. J., KIM, S. R. & LEE, S. H. 2005 CFD-based modeling of the hydrodynamic production process of polymeric microfibers and an experimental evaluation. *J.Micromech.Microeng.* **15**, 601–607.

KNIGHT, J. B., VISHWANATH, A., BRODY, J. P. & AUSTIN, R. H. 1998 Hydrodynamic focusing on a silicon chip: Mixing nanoliters in microseconds. *Physical Review Letters* **80** (17), 3863–3866.

LARSEN, U. D., BLANKENSTEIN, G. & BRANEBJERG, J. 1997 Microchip coulter particle counter. In *The International Conference on Solid-State Sensors and Actuators, TRANSDUCERS '97, (Chicago, 1997)*, , vol. 2, pp. 1319–1322.

LEE, G. B., HWEI, B. H. & HUANG, G. R. 2001 Micromachined pre-focused $M \times N$ flow switches for continuous multi-sample injection. *Journal of Micromechanics and Microengineering* **11** (6), 654–661.

MEINHART, C. D., WERELEY, S. T. & GRAY, M. H. B. 2000 Volume illumination for two-dimensional particle image velocimetry. *Meas. Sci. Technol.* **11** (6), 809–814.

MIELNIK, M. M. & SÆTRAN, L. R. 2006 Selective seeding for micro-PIV. *Experiments in Fluids* **41** (2), 155–159.

MIYAKE, R., OHKI, H., YAMAZAKI, I. & YABE, R. 1991 A development of micro sheath flow chambers. In *Proc. of the IEEE Micro Electro Mechanical Systems Workshop (Nara, Japan, Jan. 1991)*, pp. 295–264.

MOLDAVAN, A. 1934 Photo-electric technique for the counting of microscopical cells. *Science* **80**, 188–189.

MUNSON, M. S., HAWKINS, K. R., HASENBANK, M. S. & YAGER, P. 2005 Diffusion based analysis in a sheath flow microchannel: the sheath flow T-sensor. *Lab Chip* **5**, 856–862.

NGUYEN, N. T. & HUANG, X. Y. 2005 Mixing in microchannels based on hydrodynamic focusing and time-interleaved segmentation: modelling and experiment. *Lab on a Chip* **5** (11), 1320–1326.

PARK, J. S., CHOI, C. K. & KIHM, K. D. 2004 Optically sliced micro-PIV using confocal laser scanning microscopy (CLSM). *Experiments in Fluids* **37** (1), 105–119.

REYNOLDS, O. 1883 An experimental investigation of the circumstances which determine whether the motion of water shall be direct or sinous and the law of resistance in parallel channels. *Phil.Trans.R.Soc.* **174**, 935–982.

ROBINSON, J. P. 2004 Flow cytometry. In *Encyclopedia of Biomaterials and Biomedical Engineering* (ed. G. Wnek & G. Bowlin), pp. 630–640. New York: Marcel Dekker.

SANTIAGO, J. G., WERELEY, S. T., MEINHART, C. D., BEEBE, D. J. & ADRIAN, R. J. 1998 A particle image velocimetry system for microfluidics. *Experiments in Fluids* **25** (4), 316–319.

SHINOHARA, K., SUGII, Y., AOTA, A., HIBARA, A., TOKESHI, M., KITAMORI, T. & OKAMOTO, K. 2004 High-speed micro-PIV measurements of transient flow in microfluidic devices. *Meas. Sci. Technol.* **15** (10), 1965–1970.

SOBEK, D., SENTURIA, S. D. & GRAY, M. L. 1994 Microfabricated fused silica flow chambers for flow cytometry. In *Solid-State Sensor and Actuator Workshop (Hilton Head, South Carolina, June 13-16, 1994)*, pp. 260–263.

WERELEY, S. T., GUI, L. & MEINHART, C. D. 2002 Advanced algorithms for microscale particle image velocimetry. *AIAA journal* **40**, 1047–1055.

XU, Q. & NAKAJIMA, M. 2004 The generation of highly monodisperse droplets through the breakup of hydrodynamically focused microthread in a microfluidic device. *Applied Physics Letters* **85** (17), 3726–3728.

152

Outlook

The work from Papers I - III in this thesis partly formed the foundation for a EU STREP (Specific Targeted Research Projects) proposal. The project is called "Automatic Detection of Disease Related Molecular Cell Activity - MicroActive" (FP6-2004-IST-NMP-2). The objectives of the project are first to develop an integrated system based on microtechnology and biotechnology for automated diagnosis of a wide range of diseases. Secondly, to validate the accuracy of the system using cytological samples from women at risk of developing cervical cancer (the second most common female cancer) as a test case. The results from the new, automated system will be compared with traditional macroscopic hospital lab tests and available HPV DNA tests. Third, preparation of the system for industrial production. Considering the work in this thesis, it means that a new prototype of the NASBA chip will be developed and integrated with a sample preparation chip. The latter will concentrate and extract nucleic acids from a patient sample. Merged, these chips will form a disposable chip that can be used in a fully automated instrument.

This project started in December 2005, has a three year duration and consists of the participants: SINTEF (coordinator), NorChip, Institut für Mikrotechnik Mainz GmbH (D), IMTEK University of Freiburg (D), BioFluidix GmbH (D) and the Coombe Lying-in Hospital (IE). The total cost of the project is €2.78 mill.

The work from the same papers also form the basis for some of the work in a larger EU project, namely an EU IP (Integrated Project), called "Smart Integrated Biodiagnostic Systems for Healthcare - SmartHEALTH" (FP6-2004-IST-NMP-2-016817). The goal here is also to provide an open platform integrated architecture for new biodiagnostic systems, albeit this system will also include seamless links to an ambient eHealth environment, including health cards, patient records and on-line services. The system is also based on several other detection methods than NASBA, and the relevant areas of clinical application in cancer diagnostics are breast, cervical and colorectal cancer.

The project started in December 2005, has 32 participants and a 4 year duration. The coordinator is the University of Newcastle upon Tyne (UK) and

the total cost of the project is €24 mill.

The work with the hydrodynamically focused sheets in Ch. 7 are also continuing. The experiments and simulations are currently being extended to be submitted as a full journal paper by P. Domagalski, L. A. Solli, L. R. Sætran and M. M. Mielnik.

List of references

ADAMSON, A. W. & GAST, A. P. 1997 *Physical Chemistry of Surfaces*, 6th edn. New York, NY: John Wiley & Sons, Inc.

AHN, C., CHOI, J.-W., BEAUCAGE, G., NEVIN, J. H., LEE, J.-B., PUNTAMBEKAR, A. & LEE, J. Y. 2004 Disposable smart lab on a chip for point-of-care clinical diagnostics. *Proceedings of the IEEE* **92** (1), 154–173.

BARTH, T. J. & JESPERSON, D. C. 1989 The design and application of upwind schemes on unstructured meshes. In *27th Aerospace and Science Meeting & Exhibit (Reno, 9-12 Jan. 1989) AIAA 89-0366*.

BAU, H. H., ZHONG, J. & YI, M. 2001 A minute magneto hydro dynamic (MHD) mixer. *Sens. Actuators, B* **79**, 207–215.

BECKER, H. & LOCASCIO, L. E. 2002 Polymer microfluidic devices. *Talanta* **56** (2), 267–287.

BENI, G. & TENAN, M. A. 1981 Dynamics of electrowetting displays. *Journal of Applied Physics* **52** (10), 6011–6015.

VAN DEN BERG, A. & BERGVALD, P. 2006 Labs-on-a-chip: origin, highlights and future perspectives. On the occation of the 10th μTAS conference. *Lab on a Chip* **6** (10), 1266–1273.

BJÅLIE, J. G., HAUG, E., SAND, O., SJAASTAD, Ø. V. & TOVERUD, K. 2003 *Menneskekroppen*, 5th edn. Oslo, Norway: Gyldendal Akademisk.

BOOM, R., SOL, C. J. A., SALIMANS, M. M. M., JANSEN, C. L., WERTHEIMVANDILLEN, P. M. E. & VANDERNOORDAA, J. 1990 Rapid and simple method for purification of nucleic-acids. *Journal of Clinical Microbiology* **28** (3), 495–503.

BRACKBILL, J. U., KOTHE, D. B. & ZEMACH, C. 1992 A continuum method for modeling surface-tension. *Journal of Computational Physics* **100** (2), 335–354.

BRINGER, M. R., GERDTS, C. J., SONG, H., TICE, J. D. & ISMAGILOV, R. F. 2004 Microfluidic systems for chemical kinetics that rely on chaotic mixing in droplets. *Philos. Trans. R. Soc. London, Ser. A* **362** (1818), 1087–1104.

BRODY, J. P., YAGER, P., GOLDSTEIN, R. E. & AUSTIN, R. H. 1996 Biotechnology at low Reynolds numbers. *Biophysical Journal* **71** (6), 3430–3441.

BURNS, J. R. & RAMSHAW, C. 2001 The intensification of rapid reactions in multiphase systems using slug flow in capillaries. *Lab on a Chip* **1**, 10–15.

BURNS, M. A., JOHNSON, B. N., BRAHMASANDRA, S. N., HANDIQUE, K., WEBSTER, J. R., KRISHNAN, M., SAMMARCO, T. S., MAN, P. M., JONES, D., HELDSINGER, D., MASTRANGELO, C. H. & BURKE, D. T. 1998 An integrated nanoliter DNA analysis device. *Science* **282** (5388), 484–487.

BURNS, M. A., MASTRANGELO, C. H., SAMMARCO, T. S., MAN, F. P., WEBSTER, J. R., JOHNSON, B. N., FOERSTER, B., JONES, D., FIELDS, Y., KAISER, A. R. & BURKE, D. T. 1996 Microfabricated structures for integrated DNA analysis. *Proceedings of the National Academy of Sciences of the United States of America* **93** (11), 5556–5561.

CLAYTON, J. 2005 Go with the microflow. *Nature Methods* **2** (8), 621–627.

COMPTON, J. 1991 Nucleic-acid sequence-based amplification. *Nature* **350** (6313), 91–92.

COOK, N. 2003 The use of nasba for the detection of microbial pathogens in food and environmental samples. *Journal of Microbiological Methods* **53** (2), 165–174.

CROSLAND-TAYLOR, P. J. 1953 A device for counting small particles suspended in a fluid through a tube. *Nature* **17**, 37–38.

CURCIO, M. & ROERAADE, J. 2003 Continuous segmented-flow polymerase chain reaction for high-throughput miniaturized DNA amplification. *Analytical Chemistry* **75** (1), 1–7.

CUSCHIERI, K. S., WHITLEY, M. J. & CUBIE, H. A. 2004 Human papillomavirus type specific DNA and RNA persistence - Implications for cervical disease progression and monitoring. *Journal of Medical Virology* **73** (1), 65–70.

156

DEBAAR, M. P., VANDOOREN, M. W., DEROOIJ, E., BAKKER, M., VANGEMEN, B., GOUDSMIT, J. & DERONDE, A. 2001 Single rapid real-time monitored isothermal RNA amplification assay for quantification of human immunodeficiency virus type 1 isolates from groups M, N, and O. *Journal of Clinical Microbiology* **39** (4), 1378–1384.

DEIMAN, B., VAN AARLE, P. & SILLEKENS, P. 2002 Characteristics and applications of nucleic acid sequence-based amplification (NASBA). *Molecular Biotechnology* **20** (2), 163–179.

DEMELLO, A. J. 2001 DNA amplification: does "small" really mean "efficient"? *Lab on a Chip* **1** (2), 24N–29N.

DITTRICH, P. & MANZ, A. 2006 Lab-on-a-chip: microfluidics in drug discovery. *Nature Reviews Drug Discovery* **5** (3), 210–218.

DRAKE, T. & TAN, W. 2004 Molecular beacon DNA probes and their bioanalytical applications. *Applied Spectroscopy* **58** (9), 269A–280A.

DRESE, K. S., SÖRENSEN, O., SOLLI, L. A. & GULLIKSEN, A. 2003 Design and realization of a lab-on-a-chip system for multiple real-time detection of nucleic acid sequence-based amplification (NASBA). In *smallTalk 2003, San Jose, CA, USA*.

DUDA, J. L. & VRENTAS, J. S. 1971 Steady flow in the region of closed streamlines in a cylindrical cavity. *Journal of Fluid Mechanics* **45**, 247–260.

ELIAS, H. G. 1997 *An introduction to polymer science*. NY: VCH, NY.

FIORINI, G. S. & CHIU, D. T. 2005 Disposable microfluidic devices: fabrication, function, and application. *BioTechniques* **38** (3), 429–446.

FOWLER, J., MOON, H. & KIM, C.-J. 2002 Enhancement of mixing by droplet-based microfluidics. In *Proc. of the IEEE Micro Electro Mechanical Systems Workshop (Las Vegas, NV, USA, Jan 2002)*, pp. 97–100.

FRIEDMAN, N. A. & MELDRUM, D. R. 1998 Capillary tube resistive thermal cycling. *Analytical Chemistry* **70** (14), 2997–3002.

GAD-EL-HAK, M. 1999 The fluid mechanics of microdevices - the freeman scholar lecture. *J. Fluids Eng.* **121**, 5–33.

GARCIA, E., KIRKHAM, J. R., HATCH, A. V., HAWKINS, K. R. & YAGER, P. 2004 Controlled microfluidic reconstitution of functional protein from an anhydrous storage depot. *Lab on a Chip* **4** (1), 78–82.

GESCHKE, O., KLANK, H. & TELLEMANN, P., ed. 2004 *Microsystem Engineering of Lab-on-a-Chip Devices*, 1st edn. Weinheim, Germany: Wiley-VCH Verlag GmbH & Co. KGaA.

GULLIKSEN, A., SOLLI, L., KARLSEN, F., ROGNE, H., HOVIG, E., NORDSTROM, T. & SIREVAG, R. 2004 Real-time nucleic acid sequence-based amplification in nanoliter volumes. *Analytical Chemistry* **76** (1), 9–14.

GULLIKSEN, A., SOLLI, L. A., DRESE, K. S., SÖRENSEN, O., KARLSEN, F., ROGNE, H., HOVIG, E. & SIREVÅG, R. 2005 Parallel nanoliter detection of cancer markers using polymer microchips. *Lab on a Chip* **5** (4), 416–420.

GÜNTHER, A., KHAN, S. A., THALMANN, M., TRACHSEL, F. & JENSEN, K. F. 2004 Transport and reaction in microscale segmented gas-liquid flow. *Lab on a Chip* **4** (4), 278–286.

HANDIQUE, K., BURKE, D. T., MASTRANGELO, C. H. & BURNS, M. A. 2001 On-chip thermopneumatic pressure for discrete drop pumping. *Analytical Chemistry* **73** (8), 1831–1838.

HANDIQUE, K. & BURNS, M. A. 2001 Mathematical modeling of drop mixing in a slit-type microchannel. *Journal of Micromechanics and Microengineering* **11** (5), 548–554.

HANSEN, C., SKORDALAKES, E., BERGER, J. & QUAKE, S. 2002 A robust and scalable microfluidic metering method that allows protein crystal growth by free interface diffusion. *Proceedings of the National Academy of Sciences of the United States of America* **99** (26), 16531–16536.

HEILES, H. B. J., GENERSCH, E., KESSLER, C., NEUMANN, R. & EGGERS, H. J. 1988 Insitu hybridization with digoxigenin-labeled DNA of human papillomaviruses (HPV 16/18) in HeLa and SiHa cells. *Biotechniques* **6** (10), 978–981.

HIEMENZ, P. C. 1986 *Principles of colloid and surface chemistry*, 2nd edn. New York, NY: Marcel Dekker, Inc.

HIRT, C. W. & NICHOLS, B. D. 1981 Volume of fluid (VOF) method for the dynamics of free boundaries. *J.Comput.Phys.* **39**, 201–225.

HONG, C. C., CHOI, J. W. & AHN, C. H. 2001 A novel in-plane passive micromixer using coanda effect. In *Proc. of the µTAS Symposium (µTAS 2001), Monterey, CA, USA, Oct 2001*, pp. 31–33.

HONG, J. & QUAKE, S. 2003 Integrated nanoliter systems. *Nature Biotechnology* **21** (10), 1179–1183.

HRNCIR, E. & ROSINA, J. 1997 Surface tension of blood. *Physiological Research* **46** (4), 319–321.

HUCHINSON, B. R. & RAITHBY, G. D. 1986 A multigrid method based on the additive correction strategy. *Numerical Heat Transfer* **9**, 511–537.

HÜHMER, A. F. R. & LANDERS, J. P. 2000 Noncontact infrared-mediated thermocycling for effective polymerase chain reaction amplification of dna in nanoliter volumes. *Analytical Chemistry* **72** (21), 5507–5512.

ISRAELACHVILI, J. 1991 *Intermolecular & Surface Forces*, 8th edn. London, UK: Academic Press.

JAHN, A., VREELAND, W. N., GAITAN, M. & LOCASCIO, L. E. 2004 Controlled vesicle self-assembly in microfluidic channels with hydrodynamic focusing. *J.Am.Chem.Soc.* **126** (9), 2674–2675.

JENKINS, D. 2001 Diagnosing human papillomaviruses: recent advances. *Current Opinion in Infectious Diseases* **14** (1), 53–62.

JEON, N. L., BASKARAN, H., DERTINGER, S. K. W., WHITESIDES, G. M., VAN DE WATER, L. & TONER, M. 2002 Neutrophil chemotaxis in linear and complex gradients of interleukin-8 formed in a microfabricated device. *Nature Biotechnology* **20** (8), 826–830.

JEON, S. I. & ANDRADE, J. D. 1991 Protein surface interactions in the presence of polyethylene oxide .2. effect of protein size. *Journal of Colloid and Interface Science* **142** (1), 159–166.

JIN, S. & BREUER, K. S. 2003 Diffusion-limited evaporation in long microchannels. In *Proceedings of IMECE03, 2003 ASME International Mechanical Engineering Congress & Exposition, November 16-21, 2003, Washington, DC USA*. ASME.

JU, J. I., OH, H. J., KIM, S. R. & LEE, S. H. 2005 CFD-based modeling of the hydrodynamic production process of polymeric microfibers and an experimental evaluation. *J.Micromech.Microeng.* **15**, 601–607.

KATOPODES, F. V., DAVIS, A. M. J. & STONE, H. A. 2000 Piston flow in a two-dimensional channel. *Physics of Fluids* **12**, 1240–1243.

KHANDURINA, J., MCKNIGHT, T. E., JACOBSON, S. C., WATERS, L. C., FOOTE, R. S. & RAMSEY, J. M. 2000 Integrated system for rapid PCR-based DNA analysis in microfluidic devices. *Analytical Chemistry* **72** (13), 2995–3000.

KNIGHT, J. B., VISHWANATH, A., BRODY, J. P. & AUSTIN, R. H. 1998 Hydrodynamic focusing on a silicon chip: Mixing nanoliters in microseconds. *Physical Review Letters* **80** (17), 3863–3866.

KOLIOPOULOS, G., ARBYN, M., MARTIN-HIRSCH, P., KYRGIOU, M., PRENDIVILLE, W. & PARASKEVAIDIS, E. 2007 Diagnostic accuracy of human papillomavirus testing in primary cervical screening: A systematic review and meta-analysis of non-randomized studies. *Gynecologic Oncology* **104** (1), 232–246.

KOPP, M. U., LUECHINGER, M. B. & MANZ, A. 1998 Chemical amplification: Continous flow PCR on a chip. *Science* **280**, 1046–1048.

KRAUS, I. 2004 personal communication.

KRAUS, I., MOLDEN, T., ERNO, L. E., SKOMEDAL, H., KARLSEN, F. & HAGMAR, B. 2004 Human papillomavirus oncogenic expression in the dysplastic portio; an investigation of biopsies from 190 cervical cones. *British Journal of Cancer* **90** (7), 1407–1413.

LAGALLY, E. T., EMRICH, C. A. & MATHIES, R. A. 2001 Fully integrated PCR-capillary electrophoresis microsystem for DNA analysis. *Lab on a Chip* **1** (2), 102–107.

LAGALLY, E. T., MEDINTZ, I. & MATHIES, R. A. 2000*a* Single-molecule DNA amplification DNA amplification and analysis in an integrated microfluidic device. *Analytical Chemistry* **73** (3), 565–570.

LAGALLY, E. T., SIMPSON, P. C. & MATHIES, R. A. 2000*b* Monolithic integrated microfluidic DNA amplification and capillary electrophoresis analysis system. *Sens. Actuators, B* **63** (3), 138–146.

LAMMERTINK, R. G. H., SCHLAUTMANN, S., BESSELINK, G. A. J. & SCHASFOORT, R. B. M. 2004 Recirculation of nanoliter volumes within microfluidic channels. *Analytical Chemistry* **76** (11), 3018–3022.

LARSEN, U. D., BLANKENSTEIN, G. & BRANEBJERG, J. 1997 Microchip coulter particle counter. In *The International Conference on Solid-State Sensors and Actuators, TRANSDUCERS '97, (Chicago, 1997)*, , vol. 2, pp. 1319–1322.

LASER, D. J. & SANTIAGO, J. G. 2004 A review of micropumps. *Journal of Micromechanics and Microengineering* **14** (6), R35–R64.

LEE, G. B., HWEI, B. H. & HUANG, G. R. 2001 Micromachined pre-focused $M \times N$ flow switches for continuous multi-sample injection. *Journal of Micromechanics and Microengineering* **11** (6), 654–661.

LEE, S. H., LEE, C. S., KIM, B. G. & KIM, Y. K. 2003 Quantitatively controlled nanoliter liquid manipulation using hydrophobic valving and control of surface wettability. *Journal of Micromechanics and Microengineering* **13** (1), 89–97.

LEONE, G., VAN SCHIJNDEL, H., VAN GEMEN, B., KRAMER, F. R. & SCHOEN, C. D. 1998 Molecular beacon probes combined with amplification by NASBA enable homogeneous, real-time detection of RNA. *Nucleic Acids Research* **26** (9), 2150–2155.

LI, P. C. H. 2006 *Microfluidic Lab-on-a-Chip for Chemical and Biological Analysis and Discovery*, 1st edn. Boca Raton, FL: Taylor & Francis Group.

LIU, R. H., STREMLER, M. A., SHARP, K. V., OLSEN, M. G., SANTIAGO, J. G., ADRIAN, R. J., AREF, H. & BEEBE, D. J. 2000 Passive mixing in a three-dimensional serpentine microchannel. *J. Microelectromech. Syst.* **9**, 190–197.

LU, L.-H., RYU, K. S. & LIU, C. 2001 A novel microstirrer and arrays for microfluidic mixing. In *Proc. of the μTAS Symposium (μTAS 2001), Monterey, CA, USA, Oct 2001*, pp. 28–30.

MADIGAN, M. T., MARTINKO, J. M. & PARKER, J. 1997 *Biology of Microorganisms*, 8th edn. Upper Saddle River, NJ: Prentice Hall International, Inc.

MANZ, A., GRABER, N. & WIDMER, H. 1990 Miniaturized total chemical-analysis systems - a novel concept for chemical sensing. *Sensors and Actuators B-Chemical* **1** (1-6), 244–248.

MARMUR, A. 1994 Thermodynamic aspects of contact angle hysteresis. *Advances in Colloid and Interface Science* **50**, 121–141.

MEINHART, C. D., WERELEY, S. T. & GRAY, M. H. B. 2000 Volume illumination for two-dimensional particle image velocimetry. *Meas. Sci. Technol.* **11** (6), 809–814.

Mielnik, M. M. 2005 Micro-PIV and its application to some BioMEMS related microfluidic flows. PhD thesis, Norwegian University of Science and Technology (NTNU), Trondheim, Norway.

Mielnik, M. M., Ekatpure, R. P., Sætran, L. R. & Schönfeld, F. 2005 Sinusoidal crossflow microfiltration device - experimental and computational flowfield analysis. *Lab on a chip* **5** (8), 897–903.

Mielnik, M. M. & Sætran, L. R. 2006 Selective seeding for micro-PIV. *Experiments in Fluids* **41** (2), 155–159.

Mincheva, A., Gissmann, L. & Zurhausen, H. 1987 Chromosomal integration sites of human papillomavirus DNA in 3 cervical-cancer cell-lines mapped by insitu hybridization. *Medical Microbiology and Immunology* **176** (5), 245–256.

Minteer, S. D., ed. 2006 *Microfluidic Techniques: Reviews and Protocols*, 1st edn. Totowa, NJ: Humana Press Inc.

Miyake, R., Ohki, H., Yamazaki, I. & Yabe, R. 1991 A development of micro sheath flow chambers. In *Proc. of the IEEE Micro Electro Mechanical Systems Workshop (Nara, Japan, Jan. 1991)*, pp. 295–264.

Moldavan, A. 1934 Photo-electric technique for the counting of microscopical cells. *Science* **80**, 188–189.

Moran, M. M. & Sharpiro, H. N. 1998 *Fundamentals of Engineering Thermodynamics*, 3rd edn. West Sussex, England: John Wiley & Sons Ltd.

Muñoz, N., Bosch, F. X., de Sanjosé, S., Herrero, R., Castellsagué, X., Shah, K. V., Snijders, P. J. F. & Meijer, C. J. L. M. 2003 Epidemiologic classification of human papillomavirus types associated with cervial cancer. *The New England Journal of Medicine* **348** (6), 518–527.

Munson, M. S., Hawkins, K. R., Hasenbank, M. S. & Yager, P. 2005 Diffusion based analysis in a sheath flow microchannel: the sheath flow T-sensor. *Lab Chip* **5**, 856–862.

Nagai, H., Murakami, Y., Morita, Y., Yokoyama, K. & Tamiya, E. 2001 Development of a microchamber array for picoliter PCR. *Analytical Chemistry* **73** (5), 1043–1047.

Nguyen, N. & Wu, Z. 2005 Micromixers - a review. *JOURNAL OF MICROMECHANICS AND MICROENGINEERING* **15** (2), R1–R16.

NGUYEN, N. T. & HUANG, X. Y. 2005 Mixing in microchannels based on hydrodynamic focusing and time-interleaved segmentation: modelling and experiment. *Lab on a Chip* **5** (11), 1320–1326.

NGUYEN, N. T. & WERELEY, S. T. 2002 *Fundamentals and Applications of Microfluidics*, 1st edn. Norwood, MA: Artech House, Inc.

NIESTERS, H. G. M. 2001 Quantitation of viral load using real-time amplification techniques. *Methods* **25** (4), 419–429.

NIJHUIS, E. R., REESINK-PETERS, N., WISMAN, G. B., NIJMAN, H. W., VAN ZANDEN, J., VOLDERS, H., HOLLEMA, H., SUURMEIJER, A. J., SCHUURING, E. & VAN DER ZEE, A. G. 2006 An overview of innovative techniques to improve cervical cancer screening. *Cell Oncol.* **28** (5–6), 233–246.

NORDE, W. & LYKLEMA, J. 1992 Why proteins prefer interfaces. In *The Vroman Effect* (ed. C. Bamford), pp. 1–20. VSP.

NORTHRUP, M. A., CHING, M. T., WHITE, R. M. & WATSON, R. T. 1993 DNA amplification with a microfabricated reaction chamber. *Transducers '93 the 7th International Conference on Solid-State Sensors and Actuators* pp. 924–927.

ODDY, M. H., SANTIAGO, J. G. & MIKKELSEN, J. C. 2001 Electrokinetic stability micromixing. *Anal. Chem.* pp. 5822–5832.

PARK, J. S., CHOI, C. K. & KIHM, K. D. 2004 Optically sliced micro-PIV using confocal laser scanning microscopy (CLSM). *Experiments in Fluids* **37** (1), 105–119.

POLLACK, L., TATE, M. W., FINNEFROCK, A. C., KALIDAS, C., TROTTER, S., DARNTON, N. C., LURIO, L., AUSTIN, R. H., BATT, C. A., GRUNER, S. M. & MOCHRIE, S. G. J. 2001 Time resolved collapse of a folding protein observed with small angle x-ray scattering. *Physical Review Letters* **86** (21), 4962–4965.

PROBSTEIN, R. F. 1994 *Physicochemical Hydrodynamics*, 2nd edn. John Wiley & Sons, Inc.

PURCELL, E. M. 1977 Life at low Reynolds number. *American Journal of Physics* **45** (1), 3–11.

RATNER, B. D. 1995 Surface modification of polymers - chemical, biological and surface analytical challenges. *Biosensors & Bioelectronics* **10**, 797–804.

163

RAW, M. J. 1996 Robustness of coupled algebraic multigrid for the Navier-Stokes equations. In *34th Aerospace and Sciences Meeting & Exhibit, January 15-18 1996, Reno, NV, AIAA 96-0297*.

REYNOLDS, O. 1883 An experimental investigation of the circumstances which determine whether the motion of water shall be direct or sinous and the law of resistance in parallel channels. *Phil.Trans.R.Soc.* **174**, 935–982.

ROBINSON, J. P. 2004 Flow cytometry. In *Encyclopedia of Biomaterials and Biomedical Engineering* (ed. G. Wnek & G. Bowlin), pp. 630–640. New York: Marcel Dekker.

RUDMAN, M. 1997 Volume-tracking methods for interfacial flow calculations. *International Journal for Numerical Methods in Fluids* **24** (7), 671–691.

SAIKI, R. K., SCHARF, S., FALOONA, F., MULLIS, K. B., HORN, G. T., ERLICH, H. A. & ARNHEIM, N. 1985 Enzymatic amplification of beta-globin genomic sequences and restriction site analysis for diagnosis of sickle cell anemia. *Science* **230**, 1350–1354.

SALITERMAN, S. S. 2006 *Fundamentals of BioMEMS and Medical Microdevices*. Bellingham, WA: Wiley - Interscience.

SAMMARCO, T. S. & BURNS, M. A. 1999 Thermocaplliary pumping of discrete drops in microfabricated analysis devices. *AIChE Journal* **45** (2), 350–366.

SANTIAGO, J. G., WERELEY, S. T., MEINHART, C. D., BEEBE, D. J. & ADRIAN, R. J. 1998 A particle image velocimetry system for microfluidics. *Experiments in Fluids* **25** (4), 316–319.

SCHWESINGER, N., FRANK, T. & WURMUS, H. 1996 A modular microfluid system with an integrated micromixer. *Journal of Micromechanics and Microengineering* **6**, 99–102.

SENTURIA, S. D. 2001 *Microsystem Design*, 1st edn. NY, USA: Springer Science+Business Media, Inc.

SHINOHARA, K., SUGII, Y., AOTA, A., HIBARA, A., TOKESHI, M., KITAMORI, T. & OKAMOTO, K. 2004 High-speed micro-PIV measurements of transient flow in microfluidic devices. *Meas. Sci. Technol.* **15** (10), 1965–1970.

SHOFFNER, M. A., CHENG, J., HVICHIA, G. E., KRICKA, L. J. & WILDING, P. 1996 Chip PCR .1. surface passivation of microfabricated silicon-glass chips for PCR. *Nucl.Acids Res.* **24** (2), 375–379.

164

SILLEKENS, P. T. G., HABETS, W. J., BEIJER, R. P. & VANVENROOIJ, W. J. 1987 cDNA cloning of the human U1 snRNA-associated a protein - extensive homology between U1 and U2 snRNP-specific proteins. *Embo Journal* **6** (12), 3841–3848.

SOBEK, D., SENTURIA, S. D. & GRAY, M. L. 1994 Microfabricated fused silica flow chambers for flow cytometry. In *Solid-State Sensor and Actuator Workshop (Hilton Head, South Carolina, June 13-16, 1994)*, pp. 260–263.

SOLIGNAC, D. & GIJS, M. A. M. 2003 Pressure pulse injection: a powerful alternative to electrokinetic sample loading in electrophoresis microchips. *Analytical Chemistry* **75** (7), 1652–1657.

SOLLI, L. A., GULLIKSEN, A., FURUBERG, L., SÖRENSEN, O., KARLSEN, F., SÆTRAN, L. R., ROGNE, H. & DRESE, K. S. 2007 A non-contact pump mechanism for parallel movement of nanoliter sized liquid plugs using flexible diaphragms. Manuscript for submission.

SOLLI, L. A., MIELNIK, M. M., KARLSEN, F., SÆTRAN, L. R. & FURUBERG, L. 2005 Flow visualization and simulation of discrete liquid droplets moving in microchannels. In *MekIT'05 - Thrid National Conference on Computational Mechanics (Trondheim, 11-12 May, 2005)*, pp. 281–296.

SOLLI, L. A., SÆTRAN, L. R. & MIELNIK, M. M. 2006 Numerical and experimental investigation of hydrodynamically focused sheets. In *Second International Conference on Transport Phenomena in Micro and Nanodevices (Barga, Italy, 11-15 June, 2006)*.

SÖRENSEN, O., DRESE, K. S. & HARDT, S. 2003 Liquid slug transport, synchronization and mixing driven by ferrofluids. In *Proc. of the μTAS Symposium (μTAS 2001), Squaw Valley, CA, USA, Oct 2003*, pp. 1029–1032.

STROOCK, A. D., DERTINGER, S. K. W., AJDARI, A., MEZIĆ, I., STONE, H. A. & WHITESIDES, G. M. 2002 Chaotic mixer for microchannels. *Science* **295**, 647–651.

STRYER, L. 1995 *Biochemistry*, 4th edn. New York, NY: W. H. Freeman and Company, NY.

SYRJANEN, S., PARTANEN, P., MANTYJARVI, R. & SYRJANEN, K. 1988 Sensitivity of insitu hybridization techniques using biotin-labeled and s-35-labeled human papillomavirus (HPV) DNA probes. *Journal of Virological Methods* **19** (3-4), 225–238.

Taylor, G. I. 1961 Deposition of a viscous fluid on the wall of a tube. *Journal of Fluid Mechanics* **10**, 161–165.

Taylor, M. T., Nguyen, P., Ching, J. & Petersen, K. E. 2003 Simulation of microfluidic pumping in a genomic DNA blood-processing cassette. *J. Micromech. Microeng.* **13**, 201–208.

Terry, S. C. 1975 PhD thesis, Stanford University, Stanford, CA.

Tüdős, A. J., Besselink, G. A. J. & Schasfoort, R. B. M. 2001 Trends in miniaturized total analysis systems for point-of-care testing in clinical chemistry. *Lab on A Chip* **1** (2), 83–95.

Tyagi, S., Bratu, D. P. & Kramer, F. R. 1998 Multicolor molecular beacons for allele discrimination. *Nature Biotechnology* **16**, 49–53.

Tyagi, S. & Kramer, F. R. 1996 Molecular beacons: Probes that fluoresce upon hybridization. *Nature Biotechnology* **14**, 303–308.

Tyagi, S., Marras, S. A. E. & Kramer, F. R. 2000 Wavelength-shifting molecular beacons. *Nature Biotechnology* **18** (11), 1191–1196.

Veenstra, T. T., Lammertink, T. S. J., Elwenspoek, M. C. & Van den Berg, A. 1999 Characterisation method for a new diffusion mixer applicable in micro flow injection analysis systems. *Journal of Micromechanics and Microengineering* **9**, 199–202.

Verpoorte, E. 2002 Microfluidic chips for clinical and forensic analysis. *Electrophoresis* **23**, 677–712.

Walboomers, J. M. M., Jacobs, M. V., Manos, M. M., Bosch, F. X., Kummer, J. A., Shah, K. V., Snijders, P. J. F., Peto, J., Meijer, C. J. L. M. & Muñoz, N. 1999 Human papillomavirus is a necessary cause of invasive cervical cancer worldwide. *Journal of Pathology* **189** (1), 12–19.

Waters, L. C., Jacobson, S. C., Kroutchinina, N., Khandurina, J., Foote, R. S. & Ramsay, G. 1998 Multiple sample PCR amplification and electrophoretic analysis on a microchip. *Analytical Chemistry* **70**, 5172–5176.

Weigl, B. H., Bardell, R. L. & Cabrera, C. R. 2003 Lab-on-a-chip for drug development. *Advanced Drug Delivery Reviews* **55** (3), 349–377.

Wereley, S. T., Gui, L. & Meinhart, C. D. 2002 Advanced algorithms for microscale particle image velocimetry. *AIAA journal* **40**, 1047–1055.

166

WHITE, F. M. 1991 *Viscous Fluid Flow*, 2nd edn. McGraw-Hill, Inc.

WHITE, F. M. 1994 *Fluid Mechanics*, 3rd edn. McGraw-Hill, Inc.

XU, Q. & NAKAJIMA, M. 2004 The generation of highly monodisperse droplets through the breakup of hydrodynamically focused microthread in a microfluidic device. *Applied Physics Letters* **85** (17), 3726–3728.

YANG, Z., MATSUMOTO, S., GOTO, H., MATSUMOTO, M. & MAEDA, R. 2001 Ultrasonic micromixer for microfluidic systems. *Sensors and Actuators A-Physical* **93** (3), 266–272.

YUEN, P. K., KRICKA, L. J., FORTINA, P., PANARO, N. J., SAKAZUME, T. & WILDING, P. 2001 Microchip module for blood sample preparation and nucleic acid amplification reactions. *Genome Res.* **11**, 405–412.

ZHANG, C. S., XU, J. L., MA, W. L. & ZHENG, W. L. 2006 PCR microfluidic devices for DNA amplification. *Biotechnology Advances* **24** (3), 243–284.